Multi-Modality Fibre-Optic Imaging for Minimally Invasive Applications

India Lewis Thompson

A dissertation submitted in partial fulfilment

of the requirements for the degree of

Doctor of Philosophy

of

University College London.

First Supervisor: **Dr Richard Colchester**

Secondary Supervisor: **Dr Adrien Desjardins**

Department of Medical Physics

University College London (UCL)

February 12, 2025

I, India Lewis Thompson, confirm that the work presented in this thesis is my own. Where information has been derived from other sources, I confirm that this has been indicated in the work.

Abstract

All-optical ultrasound (OpUS) is an imaging paradigm which uses light to both generate and receive ultrasound and has progressed from benchtop to *in vivo* studies in recent years, demonstrating promise for minimally invasive surgical applications. This technique has advantages in terms of ease of miniaturisation through the use of optical fibres, high sensitivity, broad ultrasound bandwidth and immunity to electromagnetic interference. Additionally, the use of optics allows for easy modification to allow a lateral viewing configuration, which enables the operator to have a view of the specific vessel wall, such as coronary arteries. Another promising feature of OpUS is the potential to integrate other optical modalities, such as photoacoustic imaging or laser ablation via additional optical fibres or wavelength-selective coatings.

Recently there has been interest in using miniaturised hybrid probes for guiding minimally invasive procedures. One promising hybrid imaging methodology is the combination of ultrasound imaging and fluorescence sensing. With ultrasound imaging, an image is formed by the combination of the received reflections of ultrasound waves, thereby providing structural contrast. With fluorescence sensing, excitation light is delivered to the imaging target where it is selectively absorbed by molecules, known as fluorophores, which emit light via fluorescence, thereby providing molecular contrast. These two complementary modalities have been realised previously for imaging of the gastrointestinal tract and for assessment of cancer progression.

This thesis focuses on the integration of complementary optical modalities into a miniaturised lateral Optical Ultrasound (OpUS) probe. Ultrasound transmitters

were fabricated using a novel composite coating to assess the feasibility of creating a wavelength-selective coating with the appropriate transmission windows for complementary fluorescence sensing. These transmitters were capable of generating ultrasound pressures in excess of 1 MPa with corresponding -6 dB bandwidths > 20 MHz. After modification to generate a lateral field-of-view, these transmitters were integrated into a clinically-compatible catheter and housing. A novel rapid acquisition imaging methodology was demonstrated, enabling imaging resolutions as low as 45 µm and 120 µm in the axial and lateral extent respectively whilst achieving subsecond acquisition periods. To demonstrate the potential of the device for clinical imaging, an *ex vivo* swine oesophagus was imaged using the working channel of a mock endoscope for device delivery. Further, fluorescence sensing was incorporated to present a fibre-optic dual-modality side-viewing device for rapid pullback imaging.

This work demonstrates the promise of all-optical hybrid imaging probes to provide rapid diagnostics and guidance alongside conventional endoscopy.

Impact Statement

The research interest in medical imaging techniques and technologies has been growing exponentially in recent decades, driven by the increasing demand for more accurate, non-invasive diagnostic tools. Innovations such as optical ultrasound, fluorescence imaging and multi-modal systems are enhancing early detection and real-time monitoring, providing clinicians with detailed structural and molecular insights. These advancements are particularly transformative for minimally invasive procedures, offering higher resolution and precision. As imaging technologies continue to evolve, the development of compact and multi-functional devices is poised to revolutionise diagnostics and personalised healthcare.

This thesis presents advancements in multi-modality fibre-optic imaging for minimally invasive medical applications, focusing on the integration of optical ultrasound and fluorescence sensing into a single miniaturised device. The development of a novel, clinically compatible probe with dual-modality capabilities offers a significant leap forward in the field of medical imaging, particularly for guiding minimally invasive procedures like endoscopy.

Currently, most ultrasound transducers use piezoelectric elements to generate ultrasound from high voltage pulses. However, these elements have proved challenging to miniaturise without sacrificing key factors such as adequate reception sensitivity and wideband transmission. All-optical ultrasound is an emerging bioimaging technique that is suitable for miniaturisation to below 1 mm diameter in conjunction with high sensitivity, broad bandwidth, and immunity to electromagnetic interference. Further, the use of optics allows for elegant integration of complementary modalities like photoacoustic imaging, optical coherence tomography,

or optical fluorescence sensing.

The integration of ultrasound and fluorescence sensing in a single side-viewing fibre-optic probe improves diagnostic accuracy by providing both structural and molecular information about the vessel wall. This allows for enhanced detection of pathological changes, such as the early stages of oesophageal cancer, with high resolution and speed, reducing the need for multiple invasive procedures. The probe's potential application in identifying metaplastic transformations in Barrett's Oesophagus and oesophageal adenocarcinoma highlights its importance in addressing clinical challenges, where early diagnosis is key to improving patient outcomes.

Beyond oesophageal imaging, the probe's design has versatile applications in a range of minimally invasive procedures, offering enhanced imaging that can better assist clinicians. This work also lays the foundation for future innovations, such as integrating laser ablation, further advancing diagnostics and therapeutic techniques. Overall, this research supports ongoing efforts to make medical procedures safer, more efficient, and accessible, with significant potential to improve healthcare delivery and patient outcomes worldwide.

Acknowledgements

First and foremost I am extremely grateful to my supervisors, Prof. Adrien Desjardins and Dr. Richard Colchester for their invaluable advice, continuous support, and patience during my PhD study. Their immense knowledge and plentiful experience have encouraged me in both my academic research and daily life. I would also like to thank Dr. Edward Zhang, Dr. Sunish Mathews, Dr Erwin Alles, and Dr. Sacha Noimark for their technical support during my study. I would like to thank all the members in the Interventional Devices Group. It is their kind help and support that have made my study at UCL a wonderful time. Finally, I would like to express my gratitude to my family and friends. Without their tremendous understanding and encouragement in the past few years, it would be impossible for me to complete my study.

Contents

List of Figures

List of Tables

Glossary

R Mirror reflectivity (%).

Z_a Characteristic acoustic impedance (Ry).

k_B Boltzmann constant ($1.38x10^{-23}$J.K$^-$1).

A Area (m^2).

C_p Specific heat capacity at constant pressure(J.kg^{-1}K^{-1}).

C_v Specific heat capacity at constant volume (J.kg^{-1}K^{-1}).

C Concentration (mol/L).

E Energy (J).

F_n Noise factor (ratio).

G Incident optical energy (W.m^2).

I Light Intensity (Lumen.m^{-2}).

L_p Decibels (dB).

P_r Peak rarefactional pressure (Pa).

T Temperature ($^\circ K$).

Γ Gruneisen parameter (m^3.J^{-1}).

Φ Quantum yield (ratio).

α_{th} Thermal diffusivity ($m^2.s^{-1}$).

β Thermal expansion coefficient (K^{-1}).

ε Molar extinction coefficient ($L.mol^{-1}.m^{-1}$).

η_{PA} Photoacoustic conversion efficiency (%).

η_f Resonant efficiency (% at dB).

η_{th} Thermalisation efficiency (%).

κ Isothermal compressibility (Pa^{-1}).

λ Wavelength (nm).

μ_a Optical absorption coefficient (m^{-1}).

ρ Density of material ($kg.m^2$).

τ_l Laser pulse width (s).

τ_s Stress relaxation time (s).

τ_{th} Thermal relaxation time (s).

θ_{acc} Acceptance angle (°).

c_s Speed of sound ($m.s^{-1}$).

f_c Centre frequency (Hz).

f Frequency (Hz).

h Planck's constant ($6.63x10^{-34}$ Js).

p Pressure (Pa).

x Distance (mm).

Acronyms

AiO All-in-One.

APDs Avalanche Photodiodes.

AuNP Gold Nanoparticles.

BE Barretts Oesophagus.

CB Carbon Black.

CCDs Charge-Coupled Devices.

CMOS Complementary Metal Oxide Semiconductor Sensors.

CNFs Carbon Nanofibres.

CNT Carbon Nanotubes.

CSNPs Candle Soot Nanoparticles.

CT Computed Tomography.

CV Crystal Violet.

DD Direct Deposit.

EBUS Endobronchial Ultrasound.

ESIPT Excited State Intramolecular Proton Transfer.

EUS Endoscopic Ultrasound.

FLIM Fluorescence Lifetime Imaging.

FlS Fluorescence Sensing.

FP Fabry-Pérot.

FRET Fluorescence Resonance Energy Transfer.

FWHM Full-Width Half-Maximum.

GFP Green Fluorescent Protein.

GI Gastrointestinal.

HGD High-Grade Dysplasia.

ICG Indocyanine Green.

ICT Intramolecular Charge Transfer.

LED Light Emitting Diode.

LGD Low-Grade Dysplasia.

MRI Magnetic Resonance Imaging.

NA Numerical Aperture.

NBI Narrow-Band Imaging.

NEP Noise Equivalent Pressure.

NIR Near Infra-Red.

NPs Nanoparticles.

OCT Optical Coherence Tomography.

OpUS Optical Ultrasound.

PA Photoacoustic.

PAI Photoacoustic Imaging.

PDMS Polydimethylsiloxane.

PET Positron Emission Tomography.

PET Photoinduced Electron Transfer.

PMTs Photomultiplier Tubes.

PSF Point Spread Function.

PVDF Polyvinylidene Fluoride.

QD Quantum Dots.

rGO Reduced Graphene Oxide.

ROI Region of Interest.

SNR Signal-to-Noise Ratio.

SPR Surface Plasmon Resonance.

TGC Time Gain Compensation.

UCL University College London.

US Ultrasound.

UV Ultraviolet.

YFP Yellow Fluorescent Protein.

Chapter 1

Introduction

Many medical interventions would benefit significantly from enhanced sensing and imaging capabilities, as the limitations of using a single modality often restrict the comprehensiveness and accuracy of diagnostics and treatments [12]. For instance, traditional imaging techniques like Magnetic Resonance Imaging (MRI) or X-ray, while effective in certain contexts, may lack the sensitivity or specificity needed to detect subtle abnormalities or to provide detailed insights into complex physiological processes. By integrating multiple imaging modalities, such as combining Optical Coherence Tomography (OCT) with fluorescence imaging or Ultrasound (US) with Photoacoustic (PA) imaging, clinicians can gain a more complete picture of the tissue structure and function [12]. This multi-modal approach allows for better differentiation of tissue types, improved detection of pathological changes, and more precise guidance during interventions, ultimately leading to better patient outcomes. Positron Emission Tomography (PET) combined with Computed Tomography (CT) scans, for instance, are widely used in oncology to detect and localise tumours [13]. Here, PET provides metabolic information, while CT offers detailed anatomical structure. Similarly, OCT and fluorescence imaging are used in tandem in ophthalmology, combining both a view of the structural details of the retina and changes in molecular specificity of the tissue [14]. The synergy of different modalities harnesses the strengths of each, offsetting their individual weaknesses, and is particularly valuable in complex or minimally invasive procedures where real-time, high-resolution imaging is essential.

1.1 Motivation

Oesophageal cancer is responsible for more than 8000 deaths per year in the UK, and has a survival rate of just 12% [15]. However, it is estimated that 59% of these cases are preventable [16]. This anomaly is likely related to an early diagnosis rate of just 5.8%; the lowest Stage I diagnosis rate of any cancer in the UK [15].

Barretts Oesophagus (BE) is a precancerous condition in which the squamous lining the oesophagus begin to grow abnormally. Patients with BE are up to 125 times more likely to develop oesophageal adenocarcinoma than the general population, depending on the grading of the dysplasia [17] (Fig. 1.1).

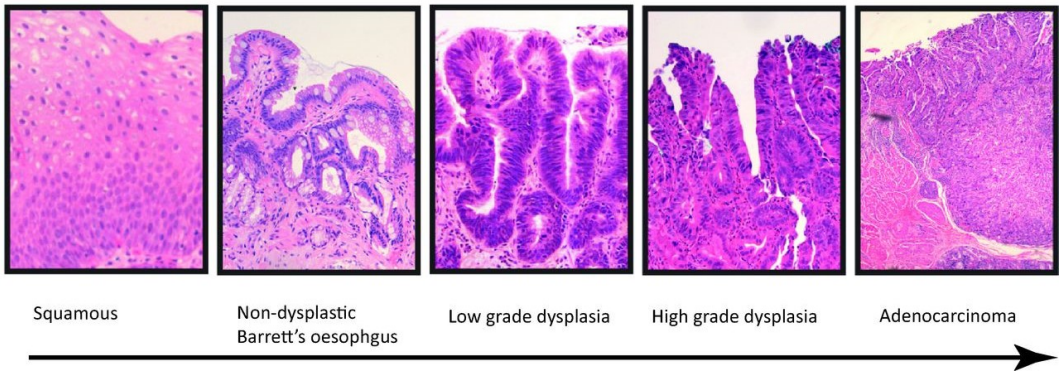

Figure 1.1: A histological description of the development of oesophageal adenocarcinoma in patients with BE. The initial lining of the oesophagus comprises squamous cells. These are then replaced by non-dysplastic columnar cells. Further molecular and genetic aberrations result in low- and high-grade dysplasia. The latter is the immediate precursor of, and often coexists with, adenocarcinoma. Taken from [1].

Currently, the gold-standard diagnostic method for BE is histology of an endoscopic biopsy [18]. The biopsied epithelium is then categorised according to the Vienna Criteria as non-dysplastic, Low-Grade Dysplasia (LGD) or High-Grade Dysplasia (HGD) [19]. However, there is significant inter- and intra-observer variability in the diagnoses of these conditions [20]. Additionally, the inherent sampling error of a biopsy gives an estimated false negative rate of 50% of all BE cases [21].

Initial diagnostic methods include the Cytosponge [22, 23] and white-light endoscopy [24]. However, histology of the cells collected by the Cytosponge only indicates the presence of 'brown cells', so this must be followed up with endoscopies to determine the location and size of the abnormal region. White-light en-

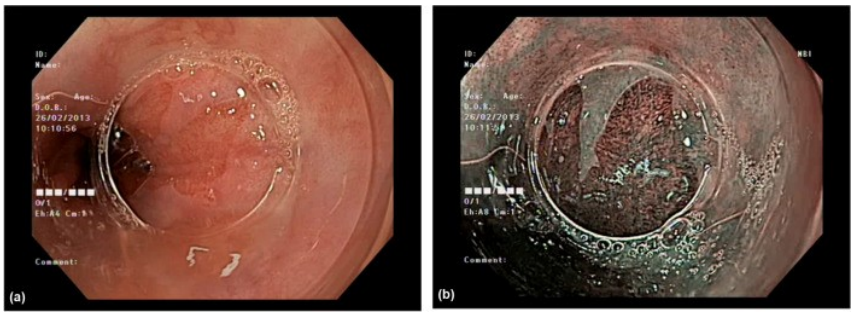

Figure 1.2: BE with HDG imaged with white-light endoscopy, supported by a) narrow band imaging, b) confocal laser endomicroscopy. Taken from [2].

doscopy, whilst highly accurate for topographic identification, cannot identify the tissue depth of the dysplasia, which is particularly important as it extends to the adventitia, where it may progress to adenocarcinoma. This must be supported by various techniques for mucosal enhancement (Fig. 1.2), including both Fluorescence Sensing (FlS) and US imaging [25]. Further, this is likely to require an oesophageal biopsy to be taken for confirmation.

As such, a medical tool is required for integration into the current endoscopic surveillance system to ascertain not only the presence of dysplasia, but the depth and density simultaneously, thereby limiting the amount of procedures required for the patient. This tool could be utilised alongside biopsies for target guidance, or indeed instead of a traditional biopsy, so as to limit the potential for a false negative.

1.2 Clinical Requirements

The first consideration is the compatibility with currently used technology, including surgical instruments such as catheters and endoscopes. This would ease the medical translation of these devices, both physically through the hardware used, and in terms of simplicity for the clinician. To this end, miniaturisation of the probe is of particular interest. Research of current endoscopic devices indicated a maximum tool channel diameter of 1 mm (Table 1.1 (1a)). Additionally, the acquisition time should be minimal to improve patient comfort. A white-light endoscopy of the upper Gastrointestinal (GI) tract takes *ca.* $5-15$ minutes depending on the required detail [31]. Assuming the clinician requires multiple imaging angles, the scan time must be short enough to accommodate multiple scans within the available

	Physical Attribute	Parameter	Advantage
	General Probe Characteristics		
1a	Device diameter	≤ 1 mm	Fits within current surgical workflow, e.g. in the working channel of an endoscope
1b	Acquisition time	< 1 minute	Fast imaging to minimise time for scans and improve patient comfort
1c	Low cost	£100s	Suitable cost for single-use device
	Ultrasound Parameters		
2a	Peak pressure	> 1 MPa	Suitable pressure for required penetration depth
2b	Bandwidth	> 20 MHz	Broadband emission of ultrasound for improved image resolution
2c	Resolution	< 100 µm	Suitable detail for imaging of vascularisation in tissue [26]
2d	Penetration depth	> 10 mm	Imaging of full oesophageal wall [27]
	Fluorescence Parameters		
3a	Signal to Noise Ratio	$\geq 20:1$	To distinguish autofluorescence from background noise sufficient for clinically useful images [28]
3b	Excitation/emission wavelengths (Porphyrins)	$400-410/600-700$ nm	Targeting porphyrins which can accumulate in dysplastic tissue [29]
3c	Excitation/emission wavelengths (Collagen)	$320-380/400-450$ nm	Targeting collagen III which can become upregulated in dysplastic tissue [30]

Table 1.1: Desired properties of an optimal imaging probe.

timeframe. As such, a target of ≤ 1 minute was decided (Table 1.1 (1b)). Due to the invasive nature of these scans, it can be assumed that these devices would be required to be single use. Therefore, minimising costs for the disposable components of the imaging system is essential (Table 1.1 (1c)). While the imaging console represents a significant cost, the device itself is relatively inexpensive to manufacture. Ideally, imaging results should be provided directly to the clinician in a relevant way that does not interfere with surgical workflow, and the probe should be robust and designed for ease of use in a clinical setting.

In order to image the full thickness of the oesophageal wall, the US should be capable of an imaging depth of *ca.* 10 mm [27] (Table 1.1 (2d)). This depth is necessary to adequately visualise the oesophageal wall and surrounding structures, such as the aorta and lymph nodes. This can be used to dictate the required US pressure. Fundamental acoustics and the speed of sound c_s states that the acoustic intensity I is defined by the peak pressure p of the US and the density of the medium ρ as:

$$I = \frac{P^2}{2\rho c} \tag{1.1}$$

Assuming an average oesophageal tissue attenuation μ_a of $0.5-0.75$ dB.MHz^{-}1.cm^{-}1, the pressure p required to reach this penetration depth d can be calculated using Beer-Lamberts law [32] as:

$$P_0 = P(d)e^{\mu_a d} \tag{1.2}$$

Here, the minimum required initial pressure for sufficient pressure at an imaging depth of 10 mm using a high-frequency source was calculated to be 0.9 MPa. As such, a target of ≥ 1 MPa was decided for the generated pressure (Table 1.1 (2a)).

The required resolution is dictated by that of comparable imaging methodologies. Conventional Endoscopic Ultrasound (EUS) achieves resolutions in the axial and lateral extent of $100-300$ and $200-500$ µm respectively depending on the acoustic profile of the US [33]. This is often used in conjunction with other modalities for enhanced visualisation. PA and OCT, for example, demonstrate much smaller resolutions, with PA imaging showing a range of $50-200$ µm in both extents and OCT showing a lateral resolution of $20-40$ µm and an axial resolution of $5-10$ µm. However, these modalities both demonstrate a poor penetration (< 3 mm). As such, a target resolution of < 100 µm in the axial and lateral extent was determined by the characteristics of BE (Table 1.1 (2c)). Here, the axial resolution is determined by the need to differentiate mucosal and submucosal layers,

while the lateral resolution is determined by the vascularisation detail within the tissue. These resolutions necessitate a broad bandwidth, so a target of 20 MHz was set (Table 1.1 (2b)).

The optimal probe for GI US imaging would combine the wide field-of-view and vessel wall visualisation of a lateral probe with integrated modalities such as FlS to indicate the presence of biomarkers such as porphyrins or upregulated collagen (Table 1.1 (3b,c)). The target Signal-to-Noise Ratio (SNR) of the fluorescent targets was determined by the current standard of fluorescent imaging systems [28] as $20:1$ (Table 1.1 (3a)).

An ideal solution would be a lateral single-fibre OpUS probe using a wavelength-selective composite coating to target autofluorescent biomarkers for integration of additional modalities without the need for additional fibres. Future work could include the additional modality of laser ablation; either wavelength-selective or by using an additional fibre. Ablation has already been successfully demonstrated for treatment of LGD within the mucosal layer [34]. This tool would be able to identify, locate, and remove dysplastic regions of the oesophagus in a single outpatient procedure.

These requirements provide a guiding framework for probe development. As this is a proof-of-concept investigation, these should be seen as target goals. It is expected that they may not be fully met in the initial iteration, but the objective is to make continuous progress toward achieving them.

1.3 Thesis Outline

The work contained in this thesis is aimed at creating a multi-modal lateral-viewing OpUS imaging device for fast pullback imaging as a building block towards clinical translation. The aim was to create a device which fulfils the requirements laid out in Section 1.2. While OpUS imaging probes have been demonstrated in clinically relevant formats, multi-modal optical probes remain limited in the literature. Moreover, few OpUS probes in existing studies offer a clinically relevant perspective, such as viewing the vessel wall, and the imaging times are relatively large [35].

Chapter 2 discusses the literature in more detail, looking at a range of topics in both OpUS imaging and fluorescence imaging. Firstly, a review of current imaging techniques for gastrointestinal imaging was conducted to identify a niche area that would benefit from this tool. Subsequently, both the theoretical background and experimental examples of OpUS imaging was discussed, including OpUS reception and an in-depth investigation into the range of composite coatings exhibited in the literature. Finally, the theory of fluorescence spectroscopy was outlined, along with an examination of the currently available techniques.

The aim of the work described in this thesis was to create a device which fulfils the requirements laid out in Table 1.1. This was broken down into three separate elements:

- Wavelength-selective coatings for multi-modal imaging. This was addressed in Chapter 3. Here, the fabrication of a novel OpUS transmitter using a NIR-absorbing dye-Polydimethylsiloxane (PDMS) composite coated fibre is described (published in MRS Advances [5]). This consisted of investigations into different fabrication methods, as well as testing the behaviour and photostability of the dye in various concentrations. Previously demonstrated composites were also fabricated for comparative testing. The transmitters were characterised and demonstrated peak pressure $\geq$ 1 MPa with corresponding bandwidths $\geq$ 30 MHz which suggested they could be suitable for imaging. In particular, the wavelength-selective behaviour was investigated to establish the potential for transmission windows to use in complementary modalities. Subsequently, OpUS pulse-echo imaging was demonstrated using a dye-PDMS coated transmitter in conjunction with an optical receiver (published in IEEE [35]). With this device, images of a tungsten wire phantom and *ex vivo* swine aorta were demonstrated, with an investigation into the impact of imaging parameters on the quality of the image. The full depth of the aorta sample was resolved and the images demonstrated the visualisation of physiological features.

- Rapid B-mode imaging with a lateral-viewing probe. This was addressed pri-

marily in Chapter 4. Here, a modified transmitter design is presented which allowed for imaging perpendicular to the fibre axis. This was demonstrated in conjunction with a novel rapid acquisition process which can achieve high-resolution images in subsecond acquisition times (published in Biomedical Optics Express [36]). Imaging resolutions as low as 45 μm and 120 μm in the axial and lateral extent respectively were reported in images acquired at speeds of 100 mm/s, with a corresponding SNR of 42 dB. This device has direct application in invasive imaging where its highly miniaturised dimensions would allow it to be used where conventional IVUS probes cannot reach. This device was housed within a clinically compatible housing, and represents a significant step towards developing clinical devices.

- Integration of a complementary fluorescence modality. This is addressed in Chapter 5. Here, a novel probe design is presented which allows for both US imaging and fluorescence sensing simultaneously. The device presented a lateral field-of-view for both modalities. Rapid multi-modal imaging was demonstrated which could offer improved guidance and diagnosis to clinicians. This work is awaiting publication at the time of thesis submission.

Finally, Chapter 6 contains a discussion of the work presented and the outlook for future work.

Chapter 2

Literature Review

This chapter is a review for the current literature pertaining to the work carried out in this thesis. Initially, the current imaging techniques in GI are investigated to ascertain the required characteristics for the developed probe. Subsequently, OpUS generation is discussed, including the theoretical approach to the design of composite coatings. The array of current transmitters are discussed, followed by an evaluation of OpUS receivers, and their combination into both lateral imaging probes and multi-modal probes that have been demonstrated previously. Finally, the methods of fluorescence imaging are discussed, including both endogenous and exogenous fluorophores used in medical imaging.

2.1 Current Imaging Techniques in Gastrointestinal Imaging

Imaging technologies play a crucial role in the diagnosis and management of oesophageal cancer and BE. Endoscopic US is highly valued for its ability to provide detailed images of the oesophageal wall and surrounding structures, allowing for accurate staging of oesophageal cancer and assessment of lymph node involvement [37]. High-resolution endoscopy, combined with advanced imaging techniques such as chromoendoscopy and Narrow-Band Imaging (NBI), enhances the detection of dysplastic changes and early cancerous lesions in BE [38]. PET-CT is utilised for staging and assessing the extent of metastatic spread in oesophageal cancer, whilst OCT offers high-resolution, cross-sectional imaging that aids in evaluating

the depth of invasion and detecting early mucosal abnormalities in BE [39]. These imaging modalities, each with their specific advantages, collectively contribute to a comprehensive approach to the diagnosis, treatment planning, and follow-up of oesophageal malignancies.

2.1.1 Optical Coherence Tomography

OCT has emerged as a valuable tool in gastrointestinal imaging, particularly for BE. OCT provides high-resolution, cross-sectional images of the oesophageal mucosa and submucosa, enabling detailed assessment of dysplastic changes and early neoplastic lesions [39, 40]. One of the major advantages of OCT is its ability to offer real-time, high-resolution imaging with excellent tissue differentiation, which aids in accurate biopsy targeting and treatment planning [41]. For example, OCT can effectively distinguish between dysplastic and non-dysplastic tissues, improving the precision of surveillance strategies and reducing the risk of overlooking early cancerous changes [42]. However, OCT also has limitations; its depth penetration is relatively shallow ($\leq$ 3 mm) compared with other imaging modalities such as endoscopic US, which can restrict its ability to evaluate deeper structures and lymph nodes [43]. Additionally, the high-resolution images obtained with OCT can generate a significant amount of data, potentially complicating interpretation and increasing the need for specialised training [44]. Despite these drawbacks, OCT remains a valuable supplement to traditional endoscopy and biopsy, enhancing the overall diagnostic and surveillance capabilities for BE and general GI imaging.

2.1.2 Positron Emission Tomography-Computed Tomography

PET-CT is increasingly utilised in the imaging and management of oesophageal diseases, including BE and oesophageal cancer. PET-CT combines the metabolic imaging capabilities of PET with the anatomical detail of CT, providing comprehensive insights into disease staging, treatment response, and detection of metastasis [45]. In the context of BE, PET-CT is less commonly used for initial diagnosis but plays a significant role in evaluating progression to oesophageal cancer and assessing the extent of disease spread once malignancy is suspected [46]. The major

advantage of PET-CT lies in its ability to detect hypermetabolic activity associated with cancerous lesions, which can be critical for identifying areas of concern that might not be evident through endoscopy or OCT alone.

However, there are limitations to the use of PET-CT in BE. One primary concern is the relatively high cost and radiation exposure associated with PET-CT scans, which may limit its use to cases where the benefit outweighs these risks [47]. Additionally, while PET-CT is excellent for staging and assessing metastatic spread, it is less effective in detecting early dysplastic changes within BE, which typically require higher-resolution imaging techniques such as endoscopy or OCT for accurate evaluation [48].

2.1.3 High-Resolution Endoscopy

High-resolution endoscopy has revolutionized the imaging and management of BE by providing detailed, close-up views of the oesophageal mucosa. This advanced endoscopic technique enhances the visualisation of subtle mucosal changes, allowing for early detection of dysplasia and carcinoma in BE [49]. High-resolution endoscopy employs ultra-thin scopes and high-definition imaging to capture fine details of the oesophageal lining, which is crucial for accurately staging BE and identifying areas that warrant biopsy [50]. This capability is particularly valuable in surveillance programs, where the early identification of dysplastic or cancerous lesions can significantly impact patient outcomes and treatment strategies.

Despite its advantages, high-resolution endoscopy has certain limitations. One key drawback is that whilst it provides excellent mucosal detail, it does not offer depth penetration beyond the mucosal layer, which can be a limitation when assessing deeper invasion or submucosal disease [51]. Furthermore, the technique demands high operator skill and experience to interpret the detailed images and accurately determine the optimal target for biopsies, which can introduce variability in diagnostic accuracy [49]. Additionally, high-resolution endoscopy is often used in conjunction with other imaging modalities to provide a comprehensive assessment, as it does not replace the need for techniques like OCT or PET-CT for deeper structural evaluation or disease staging.

2.1.4 Narrow-band Imaging

NBI has significantly advanced the field of GI imaging, particularly for the surveillance and management of BE. NBI enhances the visibility of mucosal and vascular patterns by using specific wavelengths of light, which penetrate the tissue to a shallow depth and highlight surface structures [52]. This technique improves the detection of early dysplastic and cancerous lesions by providing greater contrast between normal and abnormal tissues, enabling more accurate identification and characterisation of mucosal abnormalities [53]. For instance, NBI can reveal subtle changes in the mucosal surface and microvascular patterns that might be missed with standard white-light endoscopy, thereby aiding in the early diagnosis of dysplasia and early-stage carcinoma in BE.

However, NBI also has limitations. Its effectiveness can be constrained by the expertise required to interpret the enhanced images accurately, as well as by the technique's dependency on the quality of the endoscope and light source [52]. Additionally, while NBI excels at identifying surface abnormalities and vascular patterns, it does not provide information about the depth of tissue invasion or the presence of submucosal disease, necessitating supplementary imaging methods for a comprehensive assessment [53].

2.1.5 Chromoendoscopy

Chromoendoscopy is a valuable technique in gastrointestinal imaging, particularly useful for the detailed examination of BE. This method involves the application of special dyes or stains during endoscopy to enhance the visualisation of mucosal patterns and surface abnormalities [54]. Chromoendoscopy improves the detection of dysplastic and cancerous lesions by providing contrast between normal and abnormal tissue areas, thereby revealing subtle changes in the mucosal architecture that might be missed with standard endoscopy [38]. For instance, chromoendoscopy with methylene blue or indigo carmine can highlight areas of abnormal cell proliferation and delineate the boundaries of dysplastic lesions more clearly, facilitating targeted biopsy and accurate diagnosis.

However, chromoendoscopy has certain limitations. The technique requires

additional preparation time and the use of staining agents, which can increase the complexity and duration of the procedure [54]. Additionally, while chromoendoscopy is effective for visualising surface abnormalities, it does not provide depth information about tissue invasion or submucosal involvement, which may necessitate complementary imaging techniques for a comprehensive assessment [38]. Despite these challenges, chromoendoscopy remains a valuable tool in the surveillance and management of BE, offering enhanced mucosal detail that improves diagnostic accuracy and treatment planning, particularly when demonstrated in combination with a structural imaging modality such as OCT or US.

2.1.6 Fluorescence Imaging

Fluorescence imaging has become an increasingly significant tool in the evaluation of BE, utilising both endogenous and exogenous fluorescence to enhance the detection of abnormal tissue. Endogenous fluorescence imaging leverages the natural fluorescence properties of tissues, such as the autofluorescence of collagen and other extracellular matrix components, to differentiate between normal and pathological tissues [55]. This technique can highlight areas of dysplasia or early cancer by revealing differences in the tissue's fluorescence characteristics, thereby aiding in the identification of abnormal mucosal regions during endoscopic examination.

By contrast, exogenous fluorescence imaging involves the use of fluorescent dyes or contrast agents that are specifically designed to bind to pathological tissues or cellular targets. For example, dyes like 5-aminolevulinic acid (5-ALA) are absorbed by dysplastic or cancerous cells and emit fluorescence when exposed to specific light wavelengths, providing clear delineation of abnormal areas from healthy tissues [56]. This approach enhances the visibility of lesions that might otherwise be difficult to detect with conventional endoscopy, thus improving the accuracy of diagnosis and the precision of biopsy targeting.

However, fluorescence imaging has its limitations. Endogenous fluorescence techniques may suffer from variability in tissue autofluorescence and the potential for interference from surrounding normal tissue, which can complicate interpretation [55]. Exogenous fluorescence imaging, whilst effective, depends on the selec-

tive uptake and retention of fluorescent agents, which may not always be uniformly distributed or may lead to false positives in cases of non-specific binding [57]. Despite these challenges, fluorescence imaging remains a powerful accompaniment to traditional endoscopic methods, offering enhanced visualisation that improves the early detection and management of BE.

2.1.7 Endoscopic Ultrasound

EUS has become an essential imaging modality in the evaluation of BE and oesophageal cancer, providing detailed insights into the submucosal and deeper layers of the oesophageal wall. EUS combines endoscopy with high-frequency US, allowing for precise visualisation of the oesophageal wall layers, lymph nodes, and adjacent structures [58]. This technique is particularly valuable for staging oesophageal cancer, as it enables assessment of tumour depth, local invasion, and the involvement of regional lymph nodes. By providing a detailed cross-sectional view, EUS helps in differentiating between T1a (mucosal) and T1b (submucosal) cancer stages, which is crucial for treatment planning and determining surgical eligibility [59].

However, EUS has limitations in the context of BE. Whilst it excels at evaluating the depth of tumour invasion and local lymph node involvement, it does not provide information on superficial mucosal abnormalities or dysplasia, which are essential for the surveillance and early detection of BE. Additionally, the quality of the results can be influenced by factors such as patient anatomy and the presence of gas or other artefacts [60]. Despite these challenges, EUS remains a valuable tool in the comprehensive management of oesophageal conditions, offering critical information that complements other imaging modalities and enhances overall diagnostic and therapeutic strategies.

Typically, the US systems widely applied in medical diagnostics and considered current state of the art for US imaging use piezoelectric transducers, including in EUS applications. However, miniaturising piezoelectric probes to a sufficient diameter for EUS while maintaining adequate imaging resolution and depth poses significant challenges [61]. The imaging resolution of any US system is influenced by factors such as bandwidth, element size, and array aperture, whereas the

imaging depth is determined by acoustic pressure, directionality, and attenuation. While reducing the size of the piezoelectric element generally results in broader bandwidths, enhancing axial resolution, it also decreases the active area, leading to weaker acoustic pressure and reduced penetration depth. Moreover, miniaturised elements often operate at higher frequencies to maintain efficient performance, but these higher frequencies experience greater attenuation in tissue, further limiting imaging depth [62].

All US systems exhibit an inverse relationship between depth and lateral resolution. Miniaturising the active area of the transducer typically results in a wider US beam, increasing beam divergence with depth and degrading lateral resolution [63]. Additionally, the smaller active area reduces the precision of beam focusing, which diminishes lateral resolution. Miniaturisation also inherently limits the size and number of active elements in array transducers, restricting the application of advanced beamforming techniques such as dynamic focusing and apodisation. This reduction in active area further lowers acoustic pressure and weakens the SNR, making it harder to achieve sharp lateral resolution.

In comparison, optically-generated US shows great potential by simultaneously demonstrating extreme miniaturisation and high-resolution images. Notably, OpUS systems can also be neatly incorporated into multi-modal systems with other optical modalities due to the optical hardware requirements.

2.2 Optical Ultrasound Theory

The generation of US through the interaction of light with matter, commonly known as the PA effect, occur via a mechanism known as the thermoacoustic effect [64, 65]. This process is based on the heating effect of the light and the consequent expansion of the light-absorbing material [64, 66] and is non-destructive while demonstrating a high transduction efficiency [67]. OpUS relies on the absorption of incident light and the use of the PA effect to convert absorbed light to an acoustic wave. To obtain this effect, the light intensity must vary, either periodically as modulated light, or as a single flash (pulsed light). The PA effect is then quantified by measuring the

pressure changes in the formed acoustic wave.

2.2.1 Pressure Generation

OpUS imaging requires sufficient pressure creation. A simple set of relationships have been derived to describe the instantaneous pressure generated from an incident optical pulse.

Two important timescales exist in laser heating of a characteristic dimension: the thermal relaxation time τ_{th} and the stress relaxation time τ_s [68, 69]. Here, the characteristic dimension d_c is defined as the lesser of either the dimension of the medium or the decay constant of the optical energy deposition [70]. The thermal relaxation time is calculated by Eq. 2.1 [68], where α_{th} is the thermal diffusivity (m^2/s).

$$\tau_{th} = \frac{d_c^2}{\alpha_{th}} \tag{2.1}$$

The excitation is said to be in thermal confinement if the laser pulsewidth τ_l is shorter than τ_{th}, meaning that the heat conduction is negligible during the laser pulse. The stress relaxation time τ_s is calculated by Eq. 2.2 [69], where c_s is the speed of sound.

$$\tau_s = \frac{d_c}{c_s} \tag{2.2}$$

Similarly to the thermal confinement, the excitation is said to be in stress confinement if the laser pulsewidth τ_l is shorter than τ_s, thereby meaning that the stress propagation is negligible during the laser pulse.

The change in volume dV of a material can be found in terms of pressure p and temperature T.

$$dV = dp(\frac{\delta V}{\delta p})_T + dT(\frac{\delta V}{\delta T})_p \tag{2.3}$$

The fractional volume expansion dV/V upon laser excitation can be expressed in terms of the isothermal compressibility κ and the thermal expansion coefficient

β.

$$\frac{dV}{V} = -\kappa p + \beta T \tag{2.4}$$

Here, the isothermal compressibility can be calculated as:

$$\kappa = \frac{C_p}{\rho c_s^2 C_v} \tag{2.5}$$

where ρ is the mass density and C_p and C_v are the specific heat capacities at constant pressure and volume respectively [71]. Assuming that the incident laser pulse falls within the thermal (Eq. 2.1) and stress (Eq. 2.2) confinements, the fractional volume expansion can be considered negligible and so the local pressure rise immediately after the laser pulse can be derived from Eq. 2.4.

$$p_0 = \frac{\beta dT}{\kappa} \tag{2.6}$$

Using Beer-Lambert's law [32], the optical absorption coefficient μ_a of a given material can be calculated.

$$I = I_0 e^{-\mu_a d} \tag{2.7}$$

Given this known material quality, the temperature change dT in terms of incident optical energy G can be calculated [72].

$$dT = \frac{\eta_{th} \mu_a G}{\rho C_v} \tag{2.8}$$

Here, the thermalisation efficiency η_{th} is defined by [73] as the percentage of absorbed incident optical energy that is converted to heat in the medium. Optical energy that is not converted to heat, thereby not contributing to the thermal expansion and subsequent acoustic emission, is diverted to light emission. [73] defined this by studying the thermalisation of several common PA contrast agents, finding that the absorbers with little to no fluorescence emission such as Carbon Nanotubes (CNT) have thermalisation efficiencies of near 100%, whilst fluorescent emitters such as

Fluorescein display much lower efficiencies. Substituting Eq. 2.8 into Eq. 2.6, the local pressure rise can be calculated as:

$$dp = \frac{\beta}{\kappa \rho C_v} \eta_{th} \mu_a G \tag{2.9}$$

The Grüneisen parameter Γ [74], defined as:

$$\Gamma = \frac{\beta {c_s}^2}{C_p} = \frac{\beta}{\kappa \rho C_v} \tag{2.10}$$

can then be substituted into Eq. 2.9 to give:

$$dp = \Gamma \eta_{th} \mu_a G \tag{2.11}$$

Simply stated, this means that the generated pressure p is proportional to the material's optical absorption coefficient μ_a and its Grüneisen parameter Γ.

$$p \propto \mu_a \Gamma \tag{2.12}$$

As such, the required properties for a developed composite coating to generate the maximum US pressure p from incident energy G demand a maximised optical absorption coefficient μ_a, Grüneisen parameter Γ, and a large thermalisation efficiency η_{th}.

However, each factors has various limitations and ramifications to be considered. Maximising the optical absorption μ_a, for example, will increase the heating of the material, thus potentially creating thermal damage (Eq. 2.8). Alternatively, to optimise the Grüneisen parameter, the speed of sound through the material should be maximised, while minimising the specific heat capacity (Eq. 2.10). However, increasing the speed of sound will increase the acoustic impedance of the material:

$$Z \propto \rho c_s \tag{2.13}$$

In order to achieve good acoustic coupling to the surrounding medium, the acoustic impedance should be matched [3, 75, 76]. The acoustic impedance should

also create minimal reflection with the substrate, in order to have minimal impact on the temporal profile of the resulting pressure pulse.

2.2.2 Temporal Profiles

The temporal profile of the generated US pulse is typically dictated by the emitting surface geometry. This behaviour dictates the generated acoustic bandwidth, which subsequently dictates the attainable imaging resolution. The general PA equation for the acoustic pressure p at location $\vec{r}$, time t and temperature T [77] states:

$$(\nabla^2 - \frac{1}{c_s^2}\frac{\delta^2}{\delta t^2})p(\vec{r},t) = -\frac{\beta}{\kappa c_s^2}\frac{\delta^2 T(\vec{r},t)}{\delta t^2} \tag{2.14}$$

Assuming infinite space, where no boundary exists, Green's function for an impulse diverging spherical wave [78] is given by:

$$G(\vec{r},t:\vec{r}',t') = \frac{\delta(t-t'-\frac{|\vec{r}-\vec{r}'|}{c_s})}{4\pi|\vec{r}-\vec{r}'|} \tag{2.15}$$

Simply stated, this represents the response of a point absorber to heating. This can then be applied to Eq. 2.14. By assuming thermal confinement, and substituting Eq. 2.10, Eq. 2.14 can be rewritten in terms of pressure response as:

$$p(\vec{r},t) = \frac{1}{4\pi c_s^2}\frac{\delta}{\delta t}\left[\frac{1}{c_s t}\int d\vec{r}' p_0(\vec{r}')\delta\left(t-\frac{|\vec{r}-\vec{r}'|}{c_s}\right)\right] \tag{2.16}$$

When an excitation pulse heats up a thin slab, the resulting pressure distribution can be expressed using Eq. 2.16 as:

$$p(z,t) = \frac{1}{2}p_0(z-c_s t) + \frac{1}{2}p_0(z+c_s t) \tag{2.17}$$

The initial pressure is built up within the slab and then propagated outward in both positive and negative directions in the z plane, represented by the first and second terms respectively of Eq. 2.17. This equates to a temporal profile shown in Fig. 2.1. Experimentally, this appears as a monopolar waveform, in which the pressure peak is proportional to the energy of the incident pulse.

Similarly, when a spherical surface is heated with an excitation pulse, an initial

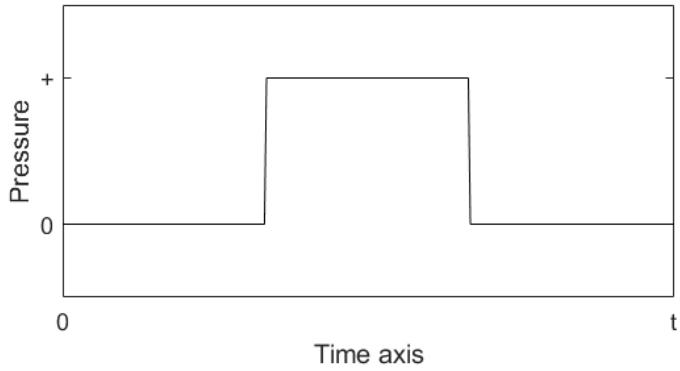

Figure 2.1: Propagating pressure from a planar slab on impulse heating.

pressure p_0 is generated inside the sphere. However, the propagation here involves spherical waves instead of the plane waves shown by the heating of the slab. As such, when the resulting pressure distribution is expressed using Eq. 2.16, it comprises of three terms:

$$p(r,t) = \frac{r+c_s t}{2r} p_0(r+c_s t) + \frac{r-c_s t}{2r} p_0(-r+c_s t) + \frac{r-c_s t}{2r} p_0(r-c_s t) \qquad (2.18)$$

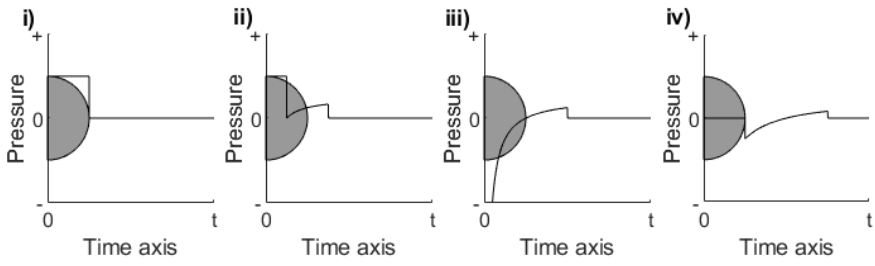

Figure 2.2: Propagating wave from a spherical source on heating showing i) initial pressure application, ii) a converging spherical wave, iii) a diverging spherical wave, and finally iv) the other converging wave.

Simply stated, the initial pressure (Fig. 2.2i)) generated within the spherical surface is divided into two equal parts, each initiating a spherical wave. One travels inwards as a converging spherical compression wave, represented by the first term on the right-hand side of Eq. 2.18 (Fig. 2.2ii)). The other travels outwards as a

diverging compression wave, represented by the third term (Fig. 2.2iii)). These two spherical waves interact at the center of the spherical object, and become a diverging spherical rarefaction wave, represented by the second term (Fig. 2.2iv)).

Experimentally, this appears as a bipolar wave, where the pressure peak is proportional to the differential of the incident intensity. The efficiency of the photoacoustic wave generation η_{PA} can be described using the energy of the laser pulse E_{pulse} and the energy of the resulting acoustic signal.

$$\eta_{PA} = \frac{E_a}{E_{pulse}} \tag{2.19}$$

Here, the energy of the acoustic signal can be approximated by considering the density ρ and sound velocity c_s of the medium, along with the measured acoustic pressure p and spot area A [79].

$$E_a = \frac{1}{\rho c_s} A \int_0^\infty p^2(t) dt \tag{2.20}$$

2.2.3 Directivity

Both diagnostic and therapeutic US applications require careful consideration of the directivity patterns of the transducers [80]. The directivity pattern of the generated US is a dimensionless parameter of the US transducer, affecting the imaging depth and image reconstruction. It is typically determined by the characteristics of the emitting substrate. It consists of a main lobe and side lobes, typically showing peak radiation intensity in the front region of the transducer source [81]. The shape of the main lobe and side lobes are determined by factors including the size, shape, and acoustic phase characteristics of the emitting surface. The directivity of laser-generated US is additionally impacted by the features of the laser beam.

For synthetic aperture imaging, a large angular divergence is required to insonify a larger region giving reflections from multiple angles, albeit to the detriment of the available penetration depth. Here, the side lobes can enhance the contrast of the reconstructed image through detectable echoes from strong reflectors situated off the central axis of the main beam [82]. However, side lobes and grating lobes

can decrease the lateral resolution [83]. In comparison, for M-mode imaging, where single A-lines are concatenated in time to produce a motion image, or other modalities where reconstruction is unneccessary, a highly directional beam will reduce the out-of-plane contributions.

A study by Yaping et al. [84] found that the angular distribution of the generated beam is dictated by the disk diameter; for small diameters, the angular range becomes more isotropic and similar to a point source. Assuming that this theory holds for the disk-like shape of the distal face of an optical fibre, it would be expected that a smaller fibre diameter would create a larger US divergence, thus creating a loss of penetration depth due to pressure loss in beam spreading. Yaping et al. additionally found that the directivity pattern is dependent on both the thermal diffusion and the optical absorption, provided that thermal confinement holds [84].

Ni et al. [85] proposed a solution for controlling the directivity of bulk waves using a pulsed laser array. However, transducer arrays, unlike single element transducers, can suffer from the effects of 'grating lobes', thereby making this method impractical.

2.2.4 OpUS Parameters

2.2.4.1 Acoustic Pressure

In general, relatively high pressure is necessary for reasonable penetration depths. The absolute pressure requirements will depend on the purpose of the transducer and the sensitivity of the receiver. The directivity of the transmitter is also a key consideration in determining the optimal pressure generation. For example, a divergent transmitter will suffer from beam spreading loss, while a highly directional transmitter will not. Using the safety limits for diagnostic US, given as:

$$\frac{P_r}{\sqrt{f_c}} \leq 0.7 \tag{2.21}$$

the upper limit for the peak rarefactional pressure P_r can be calculated, assuming a known central frequency f_c of the US beam. A cylindrical beam spreading in a homogeneous medium with negligible acoustic attenuation is subject to a pressure

loss of:

$$p \propto \frac{1}{r} \tag{2.22}$$

Using the required penetration depth and the sensitivity of the optical receiver, the lower limit of the pressure can be calculated. Given this required pressure spectrum, the transmitter can be designed according to the theory laid out in Section 2.2.1.

The importance of peak pressure generated was highlighted by [86]. This paper is widely regarded as one of the originating papers of the current fibre-based miniaturised transmitters. However, the chromium film coating demonstrated a PA conversion efficiency of just $1.2x10^{-7}$, equating to a peak-to-peak pressure too small to carry out any imaging. Later studies by the authors improved the pressure generation significantly, using composites such as graphite and carbon black [87, 88]. This improvement is likely due to a combination of factors, including the introduction of an elastomeric host to increase the Gruneisen parameter, thus improving the acoustic pressure output [3]. Additional improvements include the reduction of film thickness (Eq. 2.1, 2.2), increasing the optical absorption fraction (Eq. 2.12), and reducing the optical reflectivity (Eq. 2.24).

2.2.4.2 Bandwidth

The bandwidth of the generated US wave is typically given as the frequency at which the pressure p drops a given number of decibels below the maximum pressure. Decibels L_p here are given using Eq. 2.23.

$$L_p = 10\log_{10}\frac{p^2}{p_{ref}^2} = 20\log_{10}\frac{p}{p_{ref}} \tag{2.23}$$

At the maximum pulse length, the temporal profile is proportional to the intensity of the excitation pulse, while a shorter pulse creates a temporal profile proportional to the spatial profile of the absorbing coating [89]. Therefore, the bandwidth of the coating is determined by the the pulse length and the coating thickness; the broadest bandwidth is created by a short pulse and a thin coating. However, an in-

crease in bandwidth is likely to be limited by frequency-dependent US attenuation by the coating [90], and, for *in vivo* imaging, attenuation by the blood and tissue [91]. In practice, there is often a trade-off between maximising US pressure and US bandwidth [3].

For example, minimising the characteristic length of the absorbing coating will create a wider bandwidth. This can be achieved by either increasing the optical absorption coefficient or reducing the coating thickness. If the optical absorption coefficient is increased but the coating thickness is unchanged, the light will be absorbed over a smaller region and therefore the temperature increase will be larger and the composite is at risk of thermal damage. Conversely, if the coating thickness is reduced and the optical absorption coefficient is unchanged, less light will be absorbed and so the generated pressure will be reduced. Additionally, when the characteristic length of the absorbing region is too short, the thermal confinement condition is not met (Section 2.2.1).

2.3 OpUS Generation via Composite Coatings

The typical solution to optimise both the thermal expansion coefficient β and the optical absorption coefficient μ_a is a composite material containing an elastomer and an absorber.

2.3.1 Elastomeric Hosts

Several studies have proposed various elastomeric hosts materials for composites. However, an overwhelming majority of studies use PDMS as an elastomeric host.

PDMS has been widely used in many fields including medical technology due to its unique characteristics, including excellent temperature resistance, biocompatibility [3], strong adhesion to glass [92] and low cost. One of the main beneficial properties of PDMS is its large thermal expansion coefficient ($\beta = 300x10^{-6}\ C^{-1}$ [93]) which creates a large value of Γ. Additionally, the refractive index of PDMS is similar to that of the silica core of an optical fibre. Fresnels equation for reflection at normal incidence [94] states:

$$R = |\frac{n_1 - n_2}{n_1 + n_2}|^2 \tag{2.24}$$

Taking the refractive indices of a silica fibre core (FG400LEP, Thorlabs) n_1 as 1.46 and PDMS n_2 as 1.43 , the reflection R here is calculated as just 0.01%. This minimal reflection means high coupling of excitation light into the coating [95].

However, the primary drawback of PDMS is that it has a negligible optical absorption across the visible and Near Infra-Red (NIR) range; a low value of μ_a will create a low US pressure regardless of the size of the thermal expansion coefficient (Eq. 2.11). This low absorption is the reason for an integration of optical absorbers with the elastomeric host.

However, the hydrophobicity of PDMS limits the integration of the optical absorber to form a homogeneous composite. Additionally, the manufacturing process must also create a suitable small coating thickness to maintain a wide bandwidth (Section 2.2.4), which can be particularly challenging for coatings deposited on highly miniaturised substrates.

2.3.2 Optical Absorbers

Several optical absorbers have been integrated for a variety of applications, but the application process itself is not always straightforward. The hydrophobicity of PDMS prior to curing limits the available types of optical absorbers, as well as creating a challenging fabrication protocol for a homogeneous composite. Additional considerations are dictated by the required properties of the resulting transmitter as outlined in Section 2.2. For example, the method of substrate application impacts the thickness of the coating, subsequently affecting the acoustic attenuation and resulting bandwidth.

2.3.2.1 Carbonaceous

Carbonaceous coatings, especially carbon nanotubes, are another potential material. They often, although not always, show higher generation efficiency than metal-based generators. Chen et al. [96] found that the PA conversion efficiency for Candle Soot Nanoparticles (CSNPs)-PDMS, Carbon Nanofibres (CNFs)-PDMS,

CNT-PDMS and Carbon Black (CB)-PDMS is 13 : 5 : 4 : 1. Overall, carbonaceous coatings tend to demonstrate a higher optical absorption across both the visible and NIR wavelength ranges than metallic materials [97, 98], but the optical absorption and thus resulting acoustic wave generated by metallic films can be improved by techniques like nanostructuring [99]. However, this complex and expensive process is not ideal for the application of low-cost single-use probes such as those required for GI imaging in this context, while the simple fabrication using carbonaceous materials has yielded similar promising results [96], therefore demonstrating both excellent US generation and simple manufacturing.

Several studies demonstrate the potential of CB-PDMS, for example [98], who demonstrated that CB-PDMS has the potential to generate broadband US with a bandwidth above 100 MHz. However, the authors also found that the amplitude produced by CB-PDMS was marginally less than the pressure produced in a Gold Nanoparticles (AuNP) study carried out by the same authors [98, 99]. However, this contradiction to the general rule of carbonaceous coatings creating larger pressures than metallic absorbers is due to the nanostructuring of the AuNP mentioned previously.

Carbonaceous coatings are typically manufactured using solution-based All-in-One (AiO) methods [100, 101]. A popular carbon-based method is the use of CNT, of which the most promising results show bandwidths of around 120 MHz and up to five times more pressure than the nanostructured AuNP [99, 100, 102, 92]. Like AuNP, the nanoscale dimension of the CNT allows fast heat diffusion; as outlined in Section 2.2.1, this characteristic creates a highly efficient generation of high-frequency US. Additionally, CNT has a high damage threshold, measured as ~ 40 mJ/pulse [102]. This is ideal for increasing the pressure generation in order to increase the penetration depth for minimally invasive imaging.

Similar to CNT, CNFs-PDMS films also demonstrate high efficiency and high damage thresholds, such as that demonstrated by [103]. Here, a mesh of CNFs was fabricated through electrospinning - a complex and expensive process - after which the mesh was carbonised by heating and subsequently spin-coated with PDMS cre-

ating a bilayer composite. [103] coated optical fibres with a thickness of 24 μm, and using an incident laser fluence of 3.71 mJ/cm^2, generating a peak pressure of 12.15 MPa, giving a calculated efficiency of $1.56x10^{-2}$ Pa/W.m^{-2} - over two orders of magnitude larger than that demonstrated by CNT [102], CB [98] and AuNP [104]. However, the bandwidth reported by the authors reached only 8 MHz, which would significantly limit the potential imaging resolution. This is likely due to the thickness of the coating; 24 μm is still miniaturised but, as stated in Section 2.2.2, the minimum suitable thickness for an optical fibre of this diameter is in the region of 2 μm. However, the high pressure generated by CNFs has been studied more recently in relation to ablation applications [105], highlighting the importance of application-specific composite design.

2.3.2.2 Metallic

Examples from literature tend to show carbonaceous absorbers outperforming a simple metallic film by up to two orders of magnitude [3]. The characteristic likely responsible for this large difference is the optical reflectivity. One method for reducing the optical reflectivity, thereby increasing the optical absorption of the metallic films, is to nanostructure them.

AuNP's serve as efficient optical absorbers because of the absorption by surface plasmon resonance (SPR) structures, meaning that the spectral absorption can be shifted by varying of the particles spherical diameter [99, 106]. AuNP's have been used previously as PA contrast agents [107, 108].

A promising method of AuNP absorber-host integration is a two-dimensional nanostructure consisting of AuNP's sandwiched between a substrate and a 4.5 μm PDMS layer [99]. This method is more complex and time-consuming than the mechanical mixing of gold salt used by [109], requiring nanoimprint lithography of a polymer on a glass substrate to form a template for the pattern of the gold, after which a layer of AuNP was deposited using an electron beam evaporator. The patterned gold was then removed using acetone in a low-power ultrasonic water bath, and the PDMS layer spin-coated on top. This method gave an acoustic pressure measurement of 2 kPa at 10 mm from a laser pulse energy of 100 nJ. Using

back-propagation, the pressure at the surface of the emitter was calculated as *ca.* 1.5 MPa. This method is complex and both time- and resource-expensive, but creates a peak-to-peak pressure comparable to less complex methods such as the study by [109] (0.64 MPa at 1 mm from a smaller pulse energy of 11 μJ). However, [109] highlighted the difficulty in controlling the coating thickness by dip-coating the substrate in the composite solution which can greatly impact the attainable bandwidth of the composite.

Another advantage shown by AuNP's is the profile of the optical absorption spectra; the absorption peak here would enable the potential for wavelength-selective multi-modal devices and integrated transmit-receive devices. This dual-modality has been researched in PA imaging previously [110, 111, 112]. The Surface Plasmon Resonance (SPR) effect creates changes in the resonant frequency as the size and shape of AuNP change, enabling researchers to exploit the 'biological window' ($700 - 1870$ nm) in which the least blood and tissue attenuation occurs [113]. Tailoring the size, shape and composition of the AuNP enables a shift of the SPR peaks into the target window, improving tissue penetration and PA signal. Applied to OpUS imaging, these absorption-transmission windows could be exploited for many different applications. Cui et al. [104] recently developed a AuNP-PDMS film by adding aqueous AuNP to an uncured PDMS mixture, forming a AuNP-PDMS gel which, when coated on a substrate, was able to create simultaneous PA and US imaging under a single laser pulse irradiation. A transmission rate of 41% at 150 μm coating thickness meant that a larger proportion of the laser energy (59%) was absorbed to create the US signal, while a smaller proportion of light was emitted to be incident on the tissue and create PA signal. However, the resulting bandwidth for the US only reached 1.1 MHz at a distance of 9 mm.

Overall, AuNP demonstrates good potential for clinical imaging. Significant pressure has been shown to be generated by various manufacturing methods of a AuNP-PDMS composite [109, 104, 114]. This again highlights the importance of the PDMS component for high photoacoustic conversion efficiency and robust transmitters. They also demonstrate significant potential for multi-modal transmit-

ters [115, 116].

2.3.2.3 Quantum Dots

Quantum Dots (QD) are increasingly being explored for OpUS generation due to their unique optical and electronic properties. When excited by light, QD can efficiently convert optical energy into heat through non-radiative recombination processes, leading to rapid thermal expansion and the subsequent generation of US waves. This photothermal effect is particularly effective in producing high-frequency US signals with excellent spatial resolution. The tunability of QDs, determined by their size and composition [117, 118], allows for precise control over the generated US frequency, making them highly suitable for applications in high-resolution medical imaging and non-invasive diagnostics [119]. The CuInS2 QD demonstrated by [119] demonstrated a highly selective optical absorption profile, absorbing over 90% of light at the US generation wavelength and less than 5% in the NIR range. This nanocomposite also produced pressures exceeding 3.5 MPa with a corresponding bandwidth of 18 MHz; this pressure outperforms that demonstrated by AuNP [109, 99], dye-based [3] and indeed some carbonaceous coatings [98]. However, these composites are costly and complex to fabricate [119], and are not widely prevalent in literature.

2.3.2.4 Dye-based

Typically, dye-based coatings are fabricated using a top-down fabrication method where the optical absorbers are incorporated into pre-deposited PDMS films using techniques such as diffusion [3] or ion implantation [120]. Typically inexpensive and widely commercially available, a range of absorbing dyes have been applied in a range of applications including a Sudan II-PDMS composite for optical waveguides used in fluorescence detection [121] and a methylene blue-AuNP-PDMS solution for antibacterial activity against E-coli [122]. Whilst dyes are more widely used as exogenous PA contrast agents currently, the absorption and thermal confinement properties of these dyes make them highly suitable for US generation.

Organic pigments such as Crystal Violet (CV) have been demonstrated as both exogeneous contrast agents and OpUS coatings. However, they can display poor

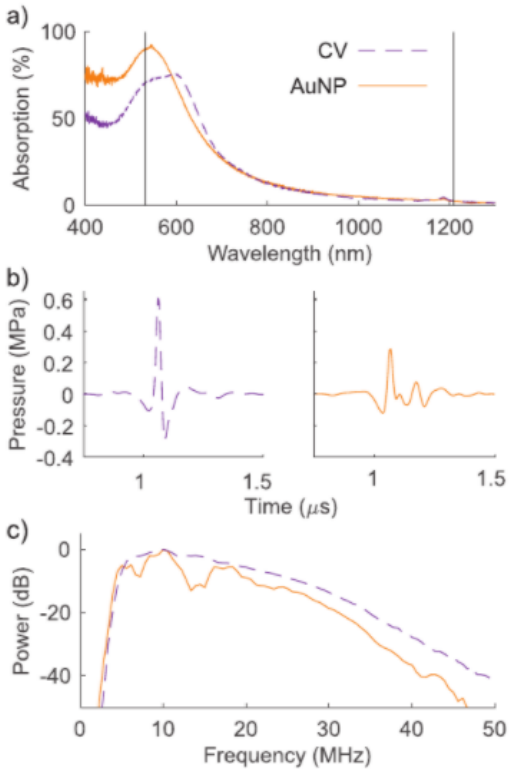

Figure 2.3: a) Optical absorption spectrum of the crystal violet and AuNP composites, with black lines showing the laser excitation wavelengths for ultrasound and photoacoustic imaging. b) Ultrasound time series from crystal violet and AuNP composites. c) Ultrasound power spectra generated by crystal violet and AuNP composites. Taken from [3].

photostability with repeated use causing photobleaching with loss of acoustic conversion efficiency. Noimark et al. [3] demonstrated a CV-PDMS composite, as well as demonstrating an AuNP-PDMS composite for comparison. For an incident optical fluence of 86.3 mJ.cm^{-1} the CV-PDMS composite showed peak-to-peak pressures of up to 0.9 MPa at a distance of 1.5 mm. The -6 dB bandwidth was measured as 15.1 MHz; significantly better than the 4.5 MHz shown by the AuNP-PDMS. The AuNP-PDMS also showed 29% lower efficiency than the CV-PDMS, despite the AuNP-PDMS demonstrating a higher optical absorption, as shown in Fig. 2.3. These differences can potentially be explained by the increased thickness of the AuNP-PDMS in comparison to the CV-PDMS due to the different fabrication methods.

This is comparable with the increase in efficiency demonstrated by carbona-

ceous coatings in comparison to AuNPs. However, as expected, the CV-PDMS demonstrated significant photobleaching, showing an 80% reduction in the generated US pressure within 15 minutes of constant exposure. This raises concerns about the viability and safety of dye-based composites for invasive use, so the photostability must be improved before clinical application.

2.4 OpUS Reception

Optical reception of US is a relatively well-established technique. While piezoelectric counterparts can be highly miniaturised [123], the use of a fibre-optic receiver completes the all-optical system. This has a wide range of benefits, including MRI compatibility, reducing the amount of bulky electronics required, and reducing the potential manufacturing costs.

2.4.1 Receiving Parameters

Optical receivers are evaluated based on various parameters, often requiring trade-offs to achieve the right balance among them. These parameters are:

- **Bandwidth and Central Frequency.** The acoustic bandwidth is a measure of the frequencies that can be efficiently detected. A broad bandwidth will be capable of resolving shorter US pulses and thus lead to a higher imaging resolution, which is key for imaging small structures such as vessel walls. For miniaturised applications, small sensor sizes are required to fulfil the size requirements for endoscopic or through-needle integration. With small receivers, diffraction effects may influence the frequency response of the receiver, such as that modelled by [124], thereby creating a complex frequency response. As such, a simple definition of bandwidth determined from the peak frequency may not sufficiently describe the frequency response.

- **Sensitivity and Noise Equivalent Pressure (NEP).** The sensitivity is typically defined as the minimum detectable signal pressure. Using the Boltzmann constant k_B, the NEP in a medium of temperature T and acoustic impedance Z_a is defined as the minimum measurable pressure above the in-

herent level of noise within the system.

$$NEP(f) = \sqrt{\frac{k_B T[1 + \frac{F_n}{\eta(f)}]Z_a}{A}} \tag{2.25}$$

Here, the key detector parameters that influence the NEP are the active area A, the on-resonant efficiencies η_f at frequency f and the noise factor F_n, which is the ratio of noise at the output of the preamplifier to the thermal noise of the source [125]. For high penetration depth and detection of signals from weakly reflecting boundaries, a low NEP ($\leq$ 100 Pa) is necessary.

- **Detector Aperture.** Also known as the acceptance angle, the detector aperture is the range of angles over which the detector can receive signals. Typically, piezoelectric transducers are directional, offering acceptable angles of below $\pm 20°$ [126]. As a result, many require acoustic lenses to increase their imaging capability [127]. In comparison, optical detectors have inherently higher acceptance angles, such as the omnidirectional receiving angle of the Fabry-Pérot (FP) hydrophones [128]. This would be well suited to synthetic aperture imaging, where US received from outside the line of sight contributes to the reconstruction. However, for alternative US imaging modalities, such as M-mode imaging where reconstruction is not necessary, a directional receiver may be preferable to reduce the effect of US reflections from outside the imaging plane.

- **Size.** Detector size is a critical parameter in the context of highly-miniaturised invasive imaging, and is a key driver in the development of OpUS detection. Piezoelectric elements are restricted from miniaturisation by a key relationship: the sensitivity of the transducer is proportional to the active area of the transducer. In comparison, OpUS transducers do not tend to demonstrate a similar dependence on active detection area so can be miniaturised extensively without a loss of sensitivity. Indeed, it has been demonstrated that a piezoelectric element with a diameter of 1 mm registered a bandwidth and

NEP of 16 MHz and 1.8 kPa respectively, while an interferometric optical transducer with a sensing area of just 0.13 x 0.27 mm - an area reduction of over 95% - created a bandwidth of 77 MHz and a 100 Pa NEP [123].

An additional consideration in the selection of a receiver is the maximum acoustic pressure measurable. This has two levels: firstly, when the induced voltage is no longer proportional to the applied pressure, and secondly, when physical damage occurs to the receiver. However, for imaging applications such as those described here, it is highly unlikely that the pressure will exceed either of these limits, and thus these limits should be of little concern.

2.4.2 Hydrophones

In general, an all-OpUS system possesses three distinct advantages over a combined piezoelectric-OpUS system; immunity to electromagnetic interference, greater robustness to mechanical and thermal damage, and potential for extreme miniaturisation [129]. As such, only fibre-optic hydrophones were considered for the imaging component of the following work. A notable exception is the Polyvinylidene Fluoride (PVDF) piezoelectric hydrophone, which is used for acoustic characterisation of fabricated transmitters.

In broad terms, optical detectors rely on physical deformation caused by US, and can be categorised as either refractometry- or interferometry-based detection [123]. Refractometry-based detection utilises the photoelastic principle and uses an interrogation laser beam to measure the difference in the refractive index of the receiving medium caused by the acoustic waves inducing mechanical stress on the medium [130]. The interferometric method relies on the premise of optical resonance, where the incident acoustic wave causes vibrations of a reflector or a change in resonant frequency, otherwise known as a change in interference condition, which is subsequently detected using a photodiode or wavelength meter [131].

2.4.2.1 Piezoelectric Needle Hydrophone

PVDF piezoelectric needle hydrophones are widely used in US measurement and imaging due to their high sensitivity and broad frequency response. These hy-

drophones are constructed using PVDF, a polymer known for its strong piezoelectric properties, allowing it to efficiently convert pressure waves from ultrasonic fields into electrical signals. The needle design, typically with diameters ranging from $0.2-1$ mm, enables high spatial resolution, making them ideal for measuring localized acoustic pressure fields with minimal disturbance to the US wave. PVDF needle hydrophones are particularly valued in medical US applications for characterising and calibrating diagnostic and therapeutic US equipment. They demonstrate an NEP of $1-10$ kPA, a broad bandwidth, and a central frequency of $1-40$ MHz. Their robustness and ability to withstand high-intensity fields without significant degradation further enhance their reliability in clinical and research settings [129, 132]. These characteristics make PVDF piezoelectric needle hydrophones essential tools in ensuring the safety and efficacy of OpUS devices.

2.4.2.2 Fabry-Perot Polymer Film Hydrophone

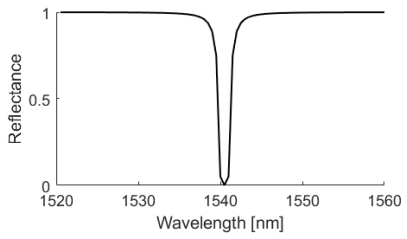

Figure 2.4: Reflectance spectra of a Fabry-Perot cavity interferometer with a reflectivity of 0.9 and a cavity length of 15 µm.

The FP interferometer is an optical cavity made from two parallel reflecting surfaces first created by Charles Fabry and Alfred Pérot in 1899 [133]. The FP polymer film hydrophone relies on acoustically induced thickness changes in an interferometric film [129]. Here, the film consists of two mirrors separated by a polymer spacer. Assuming mirrors of identical reflectivity and perpendicular incident illumination, the reflectivity can be calculated using the reflectance of the mirrors R, the wavelength λ, and the cavity thickness d.

$$R_{FP} = \frac{4R\sin^2(\frac{2\pi}{\lambda}d)}{(1-R)^2+4\sin^2(\frac{2\pi}{\lambda}d)} \tag{2.26}$$

Using a typical cavity length of 15 µm, the calculated cavity reflectance is

shown in Fig. 2.4. By tuning an interrogating laser to the midpoint of the trough in the reflectance, small cavity length changes can measured by the proportional change in reflectance [134, 135].

FP hydrophones are primarily well-suited for OpUS imaging due to their broadly omnidirectional nature; [135] demonstrated the difference between a planar fibre tip and a concave fibre tip in their interactions with complex acoustical waves. Here, the authors concluded that a concave FP cavity is more likely to direct the light to the fibre core with reduced beam divergence than a planar FP hydrophone. In a further study, [136] investigated the directionality of concave FP interferometers, showing them to be omnidirectional at frequencies up to 30 MHz, which is ideal for synthetic aperture reconstruction using out-of-plane contributions, as stated in Section 2.4, and therefore suited to a side-viewing US device. Additionally, FP hydrophones can be used to measure temperature, due to the cavity length being sensitive to the temperature fluctuations through thermal expansions, giving them significant potential for multi-modal devices [134]. Planoconcave FP sensors were shown to provide sensitivity of 9.3 Pa over 20 MHz [131].

Much of the development of the FP hydrophone has been carried out with the Photoacoustic Imaging (PAI) Group at UCL. Working in close proximity to this group makes it a preferable choice for an optical receiver in an OpUS device. The expertise and devices available will make this sensor easier to incorporate.

2.5 OpUS Imaging

OpUS imaging can be achieved using a combination of the transmission and receiving devices discussed in Sections 2.2.4 and 2.4. While many combinations of these elements have been explored, relatively few employ a lateral configuration, which is particularly desirable for imaging vessel walls, such as in GI imaging.

A key method for designing an all-OpUS probe is to place the transmit and receive elements on the same axis, much like a piezoelectric transducer where the transmit and receive functions occur in the same physical space. This design has key advantages in terms of size but may limit performance when integrating the

elements, especially in the development of a lateral probe. Forward-viewing probes using a single axis design include the device developed by [98], and the in-line probe presented by [137]. Both devices included an absorbing layer overcoated with a FP cavity, with imaging achieved through scanning a transmission and reception laser (or interrogation and generation laser). The resolution quality measured on a wire phantom for both devices were high, suggesting that the devices should provide good signal and penetration depth, but neither was used for tissue imaging due to the number of averages required, thereby making the device unsuitable for clinical application, meaning that conclusions on the imaging capabilities cannot be drawn. However, more recently, [138] presented a single dual-clad optical fibre to provide both US transmission and reception in a lateral field-of-view. Whilst this probe generated a comparatively low pressure (~ 0.4 MPa), the corresponding bandwidth was measured in excess of 27 MHz with measured imaging resolutions of 50 µm and 190 µm in the axial and lateral extent respectively. Notably, *ex vivo* tissue imaging was carried out, demonstrating detailed US images [138].

Another design considered in this work consists of adjacent transmit and receive elements. In the case of a lateral probe, this design is more easily applied, and indeed has previously been applied [139]. This probe was used for rotational imaging as opposed to pullback imaging, but was able to display B-mode images in real time. The high bandwidths combined with the wide dynamic range of the FP hydrophone allowed for high spatial resolution as well as high imaging depths, which would be beneficial for minimally invasive GI imaging.

2.5.1 Multi-Modality Probes

Multi-modal or hybrid optical imaging can be accomplished through two approaches: using additional fibres or applying wavelength-selective composite coatings (Fig. 2.5). Each method has its own advantages and limitations. Additional fibres enable greater optimization of each modality independently but increase the device's diameter. In contrast, wavelength-selective coatings offer a more compact integration of optical modalities, resulting in a smaller device size and increased mechanical flexibility.

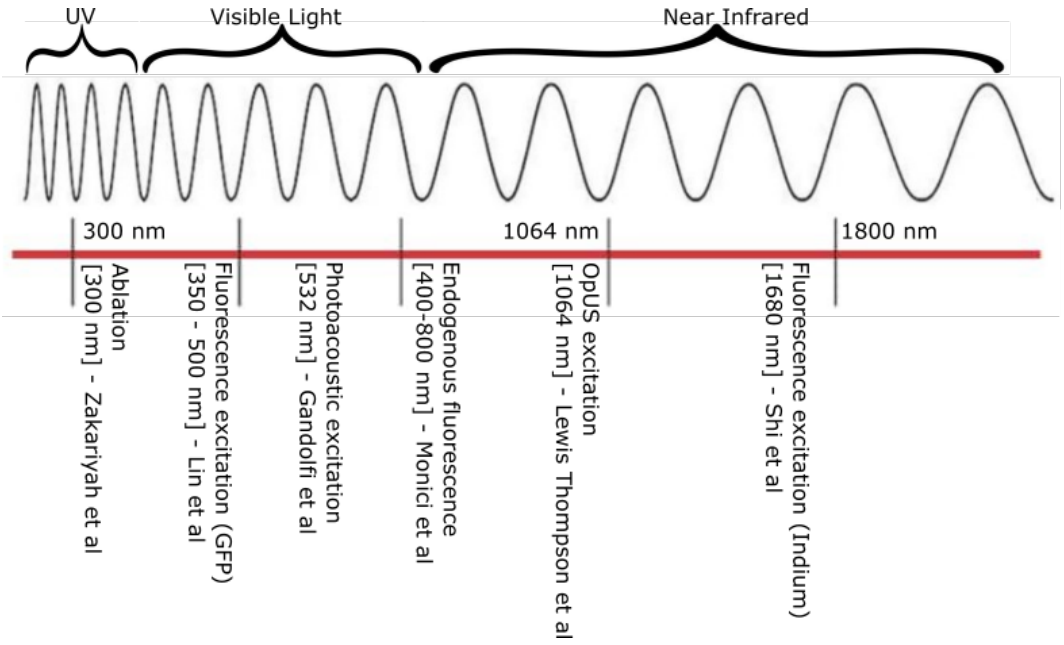

Figure 2.5: Wavelength-selective optical imaging modalities [4, 5, 6, 7, 8, 9].

Zhang et al. [140] presented a dual-modality device combining optical ablation and OpUS imaging through an additional fibre. Here, OpUS imaging was achieved with the typical combination of OpUS transmitter and receiver, with the additional modality carried out through a separate fibre delivering laser light for ablation, while maintaining a device diameter of ≤ 1 mm. This probe highlighted the benefit of separated fibres; the ablation lesions were found to vary greatly with tissue type and application parameters, so maintaining full and real-time adaptability of power deposited is essential to ensure the procedure is applied safely. However, the physical characteristics of this device pose challenges for medical translation; its diameter limits clinical integration such as lack of housing within a typical medical device such as a catheter. Additionally, its mechanical flexibility is inadequate for clinical applications.

In comparison, [141] described a US-PA design consisting of a dual-modal transmit element with an adjacent receiving element. As PA signals are also acoustic waves, they can be detected by the same optical sensor. The dichroic filter incorporated into this design allows US generation as well as transmission of certain wavelengths to carry out simultaneous PA and US imaging, with a microring re-

ceptor for US reception. Using this configuration, imaging was performed using a linear scan on several subjects, including a wire phantom of 100 μm tungsten wires and an *ex vivo* rabbit aorta. The dual modality is designed to assist clinicians by providing images with complementary detail, but the configuration shown did not achieve this aim, with the imaging of the rabbit aorta showing no distinct features, thereby requiring improvement for satisfactory clinical imaging. However, the wire phantom image showed promising detail.

Similarly, Colchester et al. [142] presented a hybrid US-PA probe utilising a wavelength-selective composite based on permanent marker ink. This probe also demonstrated promising detail in the imaging of a wire phantom, but the low pressure generated resulted in a poor penetration depth and a limited axial resolution. While this coating could be optimised for greater US generation, this would likely be at the expense of the complementary modality.

2.6 Fluorescence Spectroscopy

Monodimensional fluorescence imaging is a noninvasive, nondestructive, and sensitive technique requiring minimal sample pretreatment [143]. Fluorescence is used to determine the molecular specificity of biological materials through the presence of fluorophores. In this technique, a beam of light is passed through the solution to stimulate the electrons in the molecules of specific compounds. The light released throughout a wide range of wavelengths upon stimulation at a specific wavelength is measured as spectral data, resulting in a plot that depicts the intensity of fluorescence against the wavelengths of emission. The obtained emission spectra have been considered as a unique fingerprint of the sample [143, 10].

2.6.1 Principles of Fluorescence Imaging

2.6.1.1 Excitation and Emission

Every molecule in a substrate possesses a series of closely spaced energy levels. When a quantum of light impinges on a molecule and is absorbed, the electron is promoted from the singlet groundstate S_0 to an excited singlet state S_n. When these electrons return to the ground state S_0, there is a loss of vibrational energy. Since the

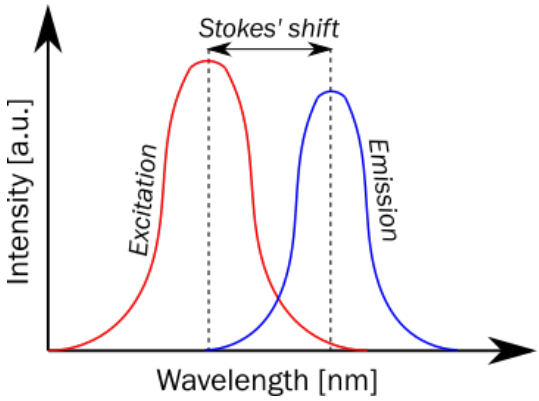

Figure 2.6: Diagram of the Stokes' shift between absorption and emission light spectra.

wavelength λ is inversely proportional to the radiation energy E, and given Planck's constant h and the speed of light c, the energy of the photon can be calculated as:

$$E = hv = \frac{hc}{\lambda} \tag{2.27}$$

This energy loss shifts the emission spectrum to longer wavelengths than the excitation spectrum, known as Stokes' Shift. A typical fluorophore absorption-emission spectra is shown in Figure 2.6. Of note is the spectral overlap between the upper end of the excitation spectra and the lower wavelengths of the emission, as well as the similarity between the absorption and emission curves.

The efficiency with which the absorbed light is converted into emitted light is known as the quantum yield Φ, expressed as:

$$\Phi = \frac{Photons_{emitted}}{Photons_{absorbed}} \tag{2.28}$$

A high quantum yield indicates that a large proportion of absorbed photons are re-emitted as fluorescence, which is desirable for applications requiring strong and clear fluorescence signals. Conversely, a low quantum yield suggests that a significant amount of absorbed energy is lost through non-radiative processes rather than being emitted as light. This is a critical parameter for designing and evaluating fluorescent probes for various applications.

2.6.1.2 Fluorophore Mechanisms

Endogenous and exogenous fluorescence are two key types of fluorescence used in imaging and detection. Endogenous fluorescence originates from naturally occurring fluorophores within biological tissues, such as NADH, flavins, and collagen. This type of fluorescence is advantageous for non-invasive imaging, as it requires no external dyes or labels. However, it often suffers from lower signal specificity and intensity, and can be complicated by autofluorescence from other tissue components [10].

Exogenous fluorescence, on the other hand, involves the introduction of external fluorophores, such as fluorescent dyes or proteins, into a biological system. These fluorophores can be engineered to target specific molecules or structures, providing higher specificity and brighter signals [143]. While exogenous fluorescence offers greater flexibility and precision, it requires careful consideration of factors like fluorophore toxicity, potential for photobleaching, and the complexity of introducing the fluorophore into the system [144]. The mechanisms of exogenous fluorophores can be categorised in one of four types:

- **Excited State Intramolecular Proton Transfer (ESIPT)**. Also known as tautomerization, ESIPT is a photophysical process where a proton is transferred within a molecule from a donor to an acceptor site upon excitation by light [145]. This transfer leads to a significant change in the electronic structure of the molecule, often resulting in dual fluorescence emissions from two distinct excited states: one before and one after the proton transfer, such as the dual peaks demonstrated by 3-Hydroxychomone derivatives [146]. This dual emission can provide valuable information about the environment around the molecule, such as polarity or hydrogen bonding, making ESIPT-based fluorophores highly sensitive for fluorescence imaging in complex biological systems [147]. Additionally, the large Stokes' shifts associated with ESIPT can minimize self-quenching and reabsorption issues, improving the accuracy of detection [143]. However, the complexity of the ESIPT process can lead to non-linear responses and complicate the interpretation of the fluorescence

signal [147].

- **Photoinduced Electron Transfer (PET)**. This is a process where, upon excitation by light, an electron is transferred from a donor molecule to an acceptor molecule within a fluorophore or between a fluorophore and its surrounding environment [148]. This transfer can quench the fluorescence of the fluorophore, reducing or even completely suppressing its emission. PET-based fluorophores are valuable for creating highly sensitive and specific fluorescence, as the fluorescence 'on/off' response can be used to detect the presence of specific analytes, such as metal ions, pH changes, or biological molecules [148]. PET fluorophores can be designed to respond to very small changes in their environment, making them excellent for detecting low concentrations of target molecules [149]. Additionally, PET sensors can be engineered to be reversible, allowing for real-time monitoring of dynamic processes in biological systems [149]. However, PET can sometimes lead to non-specific quenching, where factors other than the target analyte (such as changes in temperature or solvent polarity) can also trigger electron transfer, leading to false-positive or ambiguous results [148].

- **Fluorescence Resonance Energy Transfer (FRET)**. Here, energy is transferred non-radiatively from an excited donor fluorophore to a nearby acceptor fluorophore through dipole-dipole interactions. This energy transfer occurs when the emission spectrum of the donor overlaps with the absorption spectrum of the acceptor, and the two molecules are within a specific proximity, typically 1-10 nanometers [150, 151]. FRET is highly sensitive to molecular proximity, which allows it to be used as a 'molecular ruler' to measure distances and detect interactions between molecules with high precision. However, the design of a FRET experiment is complex, as the efficiency is affected by factors such as changes in orientation or the compatible spectra of the donor and acceptor fluorophores; typical pairings used include Green Fluorescent Protein (GFP) and Yellow Fluorescent Protein (YFP) to study real-time protein interactions [152], or Fluors 488 and 594 used for neurological

imaging [153, 154]. Further, the presence of spectral overlap can complicate the interpretation of FRET data, leading to errors or the need for complex correction methods [150].

- **Intramolecular Charge Transfer (ICT)**. In ICT, upon excitation by light, an electron is transferred within a single molecule from a donor group to an acceptor group. This electron transfer significantly alters the electronic distribution within the molecule, often resulting in a shift in the fluorescence emission spectrum, such as a red shift, and changes in fluorescence intensity . ICT fluorophores are highly sensitive to environmental factors, making them ideal for applications like sensing local polarity changes in cellular membranes (such as Nile Red, which changes its fluorescence emission depending on polarity [155]) or detecting specific ions in biological systems [156]. However, this sensitivity can also create complexity in interpreting ICT signals, as the fluorescence response can be influenced by multiple factors simultaneously [157].

2.6.1.3 Fluorescence Detection

Simply stated, fluorescence detection involves collecting the emitted light from an excited fluorophore and converting it into an electrical signal that can be analysed. Typically, the emitted fluorescence is collected using lenses, mirrors, or optical fibres, which direct the emitted light towards a detector [143]. The aim here is to maximise the amount of fluorescence captured while minimising the collection of other light sources such as reflected excitation light. Prior to reaching the detector, the light will typically pass through an emission filter that blocks the light at other unwanted wavelengths, allowing just the desired fluorescence signal to pass through [144, 158]. The separation of excitation and emission wavelengths is achieved by the proper selection of filters.

Fluorescence detection is influenced by several critical factors, including photobleaching, autofluorescence, sensitivity, and resolution [143]. Photobleaching refers to the irreversible loss of fluorescence as fluorophores degrade under pro-

longed exposure to excitation light. This degradation reduces signal strength over time, limiting the duration of experiments and the ability to capture long-term data [159]. Background autofluorescence - the natural emission of light by biological tissues or other materials - can interfere with the detection of specific signals by adding background noise, making it difficult to distinguish the target fluorescence from the background [10, 160]. Sensitivity is another key factor, determining the ability of the detection system to identify low levels of fluorescence. High sensitivity is essential for detecting weak signals but can be compromised by noise from photobleaching and autofluorescence [159, 158]. Finally, resolution impacts the ability to distinguish between closely spaced fluorescence signals. High resolution is crucial for accurately mapping the spatial distribution of fluorophores, particularly in complex biological tissues [143, 158]. Balancing these factors is essential for optimizing fluorescence detection in various imaging and analytical applications. A variety of detectors are used for fluorescence detection, detailed as follows:

- **Photomultiplier Tubes (PMTs)** These are highly sensitive detectors that convert light into an electrical signal by amplifying the signal through a series of dynodes [161]. Each dynode stage multiplies the number of electrons, resulting in a significant amplification of the original signal. A PMTs gain μ can be estimated using the emission ratio δ and the number of dynodes n as:

$$\mu = \delta^{\mathrm{n}} \tag{2.29}$$

  However, PMTs are large, fragile, and sensitive to magnetic fields, which can make them challenging to integrate into compact systems. They are often used in low-light applications such as confocal microscopy.

- **Charge-Coupled Devices (CCDs)** Widely used in cameras for fluorescence imaging, these are sensors that accumulate charge in response to light exposure. They capture photons on a silicon-based chip and convert them into electronic signals. CCDs offer high sensitivity and resolution, making them

suitable for detailed imaging tasks [162]. However, they can be slower and consume more power compared to Complementary Metal Oxide Semiconductor Sensors (CMOS) sensors.

- **CMOS** Similarly to CCDs, these capture charge in response to light, but with a faster readout and lower power consumption. They are more robust and can be integrated into smaller devices, making them ideal for portable imaging systems. However, CMOS sensors generally have higher noise levels compared to CCDs, which can affect image quality [163].

- **Avalanche Photodiodes (APDs)** These are highly sensitive detectors that operate by amplifying the photo-generated current through an avalanche effect. They offer high gain and fast response times, making them suitable for time-resolved fluorescence detection. However, APDs are also prone to noise, particularly at high gains, which can limit their sensitivity and dynamic range [164].

2.6.2 Techniques in Fluorescence Imaging

Fluorescence imaging is a cornerstone of modern biological and medical research, offering the ability to visualise and analyse specific molecules within cells and tissues with high sensitivity and specificity. The diversity of techniques available in fluorescence imaging, ranging from widefield microscopy to more advanced methods like confocal microscopy, allows researchers to tailor their approach based on the resolution, depth, and temporal dynamics required by their studies.

2.6.2.1 Widefield Fluorescence Microscopy

Widefield fluorescence microscopy is a powerful imaging technique that enables the visualisation of fluorescent labelled samples across a wide field of view. In this method, the entire sample is illuminated simultaneously with a light source, typically a mercury or xenon lamp, that excites fluorescent molecules within the sample. The emitted fluorescence from these molecules is then captured by a camera, such as a CCDs or CMOS sensor, creating an image that displays the distribution and intensity of fluorescence across the sample.

One of the major advantages of widefield fluorescence microscopy is its ability to rapidly acquire images, making it suitable for live-cell imaging and large-scale screening applications [165]. However, a significant limitation is that out-of-focus light from other parts of the sample can contribute to the image, leading to reduced contrast and potential blurring. This issue is particularly pronounced in thick samples, where light from above and below the focal plane can interfere with the sharpness of the image [166]. To mitigate these effects, deconvolution algorithms are often employed to improve image clarity by computationally removing out-of-focus light [165]. Despite this limitation, widefield fluorescence microscopy remains a widely used and accessible technique, particularly when speed and simplicity are key considerations.

2.6.2.2 Confocal Microscopy

Confocal microscopy is an advanced fluorescence imaging technique that enhances optical resolution and contrast by employing a spatial pinhole to eliminate out-of-focus light from the sample. Unlike widefield microscopy, where the entire sample is illuminated, confocal microscopy focuses light onto a specific point within the sample, scanning it point by point to construct a detailed image. This method is particularly beneficial for imaging thick specimens, as it allows for the collection of optical sections at different depths, enabling three-dimensional reconstruction of the sample [158].

The key advantages of confocal microscopy include its ability to produce high-resolution images with improved contrast and its capacity for generating 3D images of complex structures. However, these benefits come at the cost of longer acquisition times and potential photobleaching due to the intense laser light used for excitation [158, 167]. Additionally, the need for precise alignment and calibration of the optical components can make confocal microscopy more technically demanding than widefield techniques. Confocal microscopy has been widely adopted in biological and medical research, particularly for detailed studies of cellular structures, protein localisation, and tissue architecture [158].

2.6.2.3 Two-Photon Microscopy

Two-photon microscopy is an advanced fluorescence imaging technique that allows for deep tissue imaging with reduced photodamage and photobleaching compared to traditional single-photon methods. This technique utilises NIR laser light to excite fluorophores through the simultaneous absorption of two lower-energy photons. Because two-photon absorption is a nonlinear process, it occurs only at the focal point of the laser, thereby minimising out-of-focus excitation and allowing for precise, three-dimensional imaging of biological specimens.

One of the significant advantages of two-photon microscopy is its ability to image deeper into tissues, often up to 1 mm [168], which is significantly further than conventional fluorescence techniques. This depth penetration, combined with reduced scattering of NIR light, makes two-photon microscopy particularly valuable for imaging in thick, living tissues, such as brain slices [169, 170] or whole embryos [171]. However, the technique requires expensive and complex laser systems, and the need for high laser power at the focal point can still result in localised photodamage if not carefully managed [170]. Two-photon microscopy has become a vital tool in neuroscience, developmental biology, and other fields where deep tissue imaging is essential. It is especially renowned for its ability to image living tissues over extended periods with minimal phototoxic effects.

2.6.2.4 Fluorescence Lifetime Imaging

Fluorescence Lifetime Imaging (FLIM) is an advanced microscopy technique that provides insights into the dynamics of fluorescent molecules by measuring the time they spend in their excited state before returning to the ground state. Unlike traditional fluorescence microscopy, which relies on intensity measurements, FLIM captures the decay times of fluorescent signals, offering enhanced contrast and specificity. This technique is particularly useful for studying molecular interactions, cellular environments, and dynamic processes at the nanometre scale. For instance, FLIM can be used to investigate protein-protein interactions through FRET by analysing the changes in fluorescence lifetime when energy transfer occurs between donor and acceptor molecules [150, 172]. Additionally, FLIM has existing

applications in cancer research, where it helps to identify changes in cellular microenvironments that may indicate disease progression [143].

2.7 Chapter Conclusions

This chapter has discussed relevant literature pertaining to the development of a hybrid tool for use in multi-modal optical imaging of the GI tract. Initially, a review of the various techniques used to visualise and diagnose conditions within the GI tract was conducted. Endoscopy is the most common method, using a flexible tube with a camera to directly view the GI vessel wall. CT provides cross-sectional images that can detect structural abnormalities, masses, and inflammation. US is frequently used for evaluating the liver, gallbladder, and other abdominal organs, often supplemented by EUS, which combines endoscopy with US to obtain detailed images of the GI wall and surrounding structures. Fluorescence imaging and spectroscopy offers real-time molecular insights by detecting fluorescent signals from targeted dyes, which can reveal early-stage disease not visible with standard techniques. OCT provides high-resolution cross-sectional images of tissue microarchitecture, aiding in early detection of dysplasia and cancer. These methods, often used in combination, enable comprehensive assessment and diagnosis of GI conditions. It was concluded that there is a requirement for a tool combining the structural information of US and the molecular specificity of fluorescence sensing.

Subsequently, the theory and current literature demonstrating OpUS probes was discussed. From this, there are a few key conclusions to be drawn, and applied to the subsequent work:

- The composite coating requires an optical absorber with a high absorption coefficient and an elastomeric host with a high thermal expansion coefficient in order to efficiently generate a sufficient US profile. A high pressure is required for the potential obtainable penetration depth, and a broad bandwidth is necessary for high-resolution imaging.

- The application of this composite coating must be considered in relation to the incident laser pulse width and energy to maintain the thermal and stress

confinements, as well as begin a similar impedance to that of the medium.

- The profile of the transmitter must be carefully considered to tailor the beam divergence and penetration depth of the US. This depends on the application: for synthetic aperture imaging, a wider beam divergence is preferred at the expense of penetration depth, while M-mode images rely on a highly directional profile.

- The receiver best suited for the intended lateral imaging probe would be omnidirectional, miniature, and demonstrate a broad bandwidth. These requirements are satisfied by the FP interferometer. This is also developed primarily by the PAI group at UCL, so this sensor is the preferable choice due to the expertise and devices easily available.

- Multi-modality probes can be configured with either a wavelength-selective composite coating or a dual-fibre approach. If a wavelength-selective coating is used, the transmission window must demonstrate an absorption of $\leq 20\%$ of the incident light to be efficient excitation for complementary modalities.

Finally, the theory and current techniques used in fluorescence sensing were thoroughly discussed, highlighting the principles, methods, and innovations that shape this field. The key conclusions drawn emphasise that the configuration of a designed fluorescence sensing system is primarily influenced by the characteristics of the targeted fluorophore. Factors such as the fluorophore's emission and excitation spectra, sensitivity to environmental conditions, and photostability play crucial roles in determining the optimal design and functionality of the excitation element and the selected receiver. This underscores the importance of carefully selecting and tailoring the system components to achieve the desired specificity and performance, ultimately enhancing the accuracy and reliability of fluorescence-based measurements.

Chapter 3

Photostable NIR Dyes for Ultrasound Generation

This chapter is based on work published in [5] and [35], and describes the development of novel US transmitters, comprised of Epolight-PDMS coatings on optical fibres.

3.1 Introduction

The generation of US via all-optical methods is covered in Chapter 2. Briefly, both a large optical absorption μ_a and thermal expansion coefficient β are required for an efficient PA effect; these parameters are typically maximised through composite materials consisting of an elastomeric host and an optical absorber.

One specific area of interest for optical US generation is the capacity for complementary therapeutic and imaging modalities to be integrated [119]. However, combining modalities requires carefully engineered composite materials with wavelength-selective absorption [3]. Here, the US can be generated at one wavelength via optical absorption within the coating, whilst at other wavelengths light can be transmitted through the coating and be used or a complementary modality such as PA imaging [104, 141] or laser ablation [140]. Previous research has demonstrated the use of CV or AuNP embedded in a PDMS host for co-registered US and PA imaging [3]. However, these composites suffered from poor photostability under prolonged laser exposure, as well as limited US pressures and bandwidths.

Recently, QD's have been demonstrated for co-registered US and PA imaging, but these were fabricated through a complex process [119].

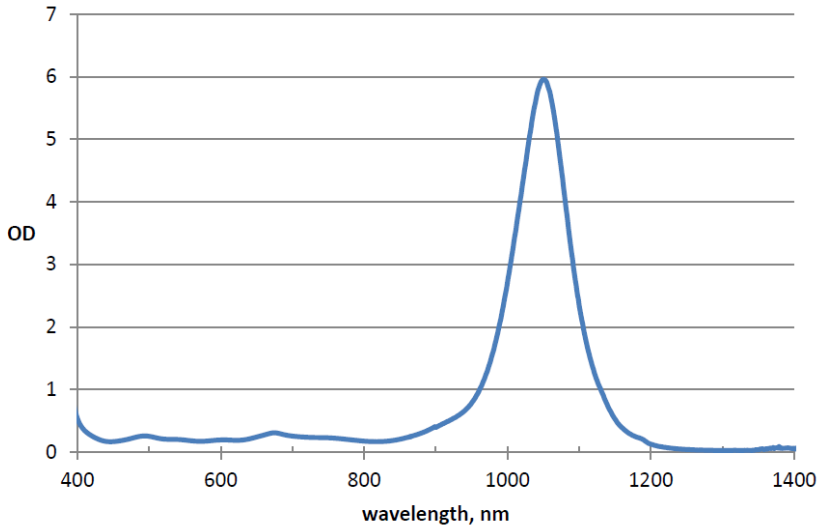

Figure 3.1: Optical density spectrum of Epolight 9837 in polycarbonate, provided by Epolin, UK.

The work in this chapter details an investigation into the use of a photostable NIR dye - Epolight 9837 - as a dichroic optical absorber. This dye was selected due to its selective absorption window centered at 1064 nm (see Fig. 3.1) as demonstrated by the manufacturer. The optical density profile provided by the manufacturer is based on a 1 mm thick film consisting of a dye mass fraction of 0.5 suspended in a polycarbonate host, which ensures optical transparency in the 400–1400 nm range while offering a stable, solid medium that preserves the absorber's optical properties. The optical density of a material with a molar extinction coefficient ε, a concentration C and path length d is given as:

$$OD = \varepsilon C d \tag{3.1}$$

Using this, the optical density of a comparative absorber such as CV at 1064 nm would be *ca.* 0.15 with a selective peak of *ca.* 9 at 532 nm while Reduced Graphene Oxide (rGO) would show a consistent optical density of *ca.* 5 in the range of $400 - 1400$ nm.

Here, Epolight 9837 was embedded in a PDMS host and deposited on the tip

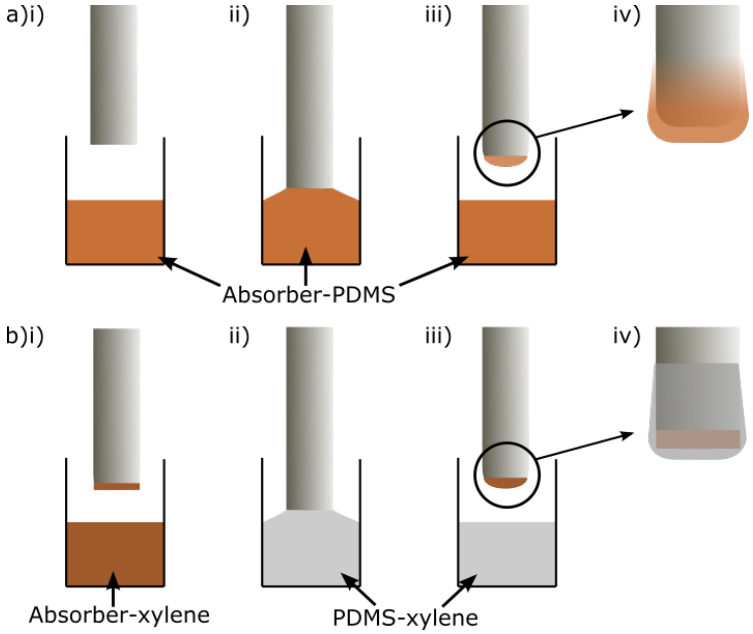

Figure 3.2: a) AiO dip-coating process: i) fibre and AiO solution of optical absorber and PDMS. ii) fibre inserted into the solution. iii) fibre withdrawal leaving iv) a coating on the tip. b) DD dip-coating process. i) fibre coated in a solution of optical absorber and xylene. ii) coated fibre inserted into a solution of PDMS and xylene. iii) fibre withdrawn leaving iv) a bilayer coating on the tip.

of optical fibres; this composite was studied in terms of its suitability for OpUS and complementary modalities. This includes a detailed study of various manufacturing methods, a photostability study, and a comparison with a widely used composite - rGO-PDMS - in imaging applications.

3.2 Methods

3.2.1 Fabrication

All composite coatings were fabricated and tested on proximal-end SMA connectorised optical fibres with a core diameter of 400 µm (FG400LEP, Thorlabs, UK), consisting of a fused silica core/cladding with a core:cladding ratio of 1 : 1.06 and a polyimide buffer jacket.

3.2.1.1 Dip Coating Procedure

Simply stated, dip coating is the application of material to a substrate by immersing and removing the substrate from the liquid to create a film (Fig. 3.2). Typically,

Dye	Dye Weight	Substrate	Fabrication	Ref.
Epolight	2.5 mg 5 mg 10 mg 15 mg	Fibre	AiO	2.5A 5A 10A 15A
Epolight	2.5 mg 5 mg 10 mg 15 mg	Fibre	DD	2.5D 5D 10D 15D
CV	40.8 mg	Fibre	Heat Diffusion	CVO
CV-AuNP	40.8 mg	Slide	Heat Diffusion (backed)	CVAUB
CV-AuNP	40.8 mg	Slide	Heat Diffusion (unbacked)	CVAUU
rGO	500 mg	Fibre	DD	rGO

Table 3.1: Dye-PDMS composites fabricated for characterisation.

this solution contains an adhesive element such as PDMS. After the withdrawal of the substrate from the solution, a homogeneous liquid film is formed on the surface. Subsequently, the solvents in the solution will be evaporated through drying in ambient conditions, resulting in a thin film of coating adhered to the substrate surface. Studies have shown that the thickness of the resulting coating relies on the speed of withdrawal, the viscosity of the solution, the solvent used, and the concentration of the suspension [173, 174].

3.2.1.2 Coating Application

Optical fibres were prepared for coating by first removing the buffer coating from the distal end of the fibre. Subsequently, the distal end was cleaved manually using a tungsten blade. The prepared optical fibres were manually dipped into the prepared composite solutions and left to cure under ambient conditions for 24 hours with the distal end surface facing up.

3.2.1.3 Epolight Preparation

All measurements of Epolight were taken using a scale from Denver Instruments with a standard error of ± 0.05 mg. To form a homogeneous material of PDMS and Epolight, the Epolight powder must first be dissolved into an organic solvent. The solvent used here was xylene, which was standardised as 0.5 ml per solution to maintain the concentration of Epolight as the independent variable. The selected weight of Epolight powder was mixed with the xylene solvent until the dye was visibly dissolved. Two coating methods were then used to apply the materials to the fibres (Fig. 3.2).

All-in-One Synthesisation

AiO synthesisation requires the combining of the elastomeric host and optical absorber prior to their application to the substrate. Here, the Epolight-xylene solution was manually mixed with 0.25 g of PDMS (MED-1000, Polymer Systems Technology, UK). This one-pot solution was then applied to the optical fibre using the dip coating process (Fig. 3.2a).

Direct Deposit Synthesisation

The Direct Deposit (DD) method requires two applications of coating to create a bilayer composite (Fig. 3.2b). Firstly, the Epolight-xylene solution was deposited on the fibre through dip coating. This coating of the optical absorber was left to dry (*ca.* 30 minutes). Subsequently, the coated fibre was dip coated again in the PDMS layer. Here, 0.25 g of PDMS was diluted with 0.5 ml of xylene which is manually mixed.

3.2.1.4 Crystal Violet Preparation

Crystal Violet Fibres

The CV fibres were manufactured as per the top-down protocol outlined by [3]. One concentration of CV fibres was fabricated: 0.0408 g of powdered CV was mixed with de-ionised water to form 10 ml of liquid. Briefly, the fibres were dip-coated in a solution of PDMS and xylene (0.25 g:0.5 ml) and left to cure in ambient conditions. Once cured, these fibres were then submerged in a vial of liquid CV heated to 80°C for $\sim$ 12 hours, allowing the dye to diffuse into the PDMS to achieve large uptake of the dye. These fibres were then removed and left to dry.

Crystal Violet Slides with Gold Nanoparticles

Here, CVAuNP-PDMS composites were fabricated by Dr. Sacha Noimark. These coatings were fabricated on glass slides rather than the distal face of an optical fibre. This was achieved using the heated diffusion method as before, followed by addition of AuNP via *in situ* reduction of gold salt. Two variations were fabricated: the first formation required the CV-PDMS to be backed with Kaplan tape prior to the addition of the gold salt (Table 3.1: CVAUB) while the second was not backed (Table 3.1: CVAUU), meaning that the AuNP particles were able to diffuse from both sides of the composite sheet.

3.2.1.5 Reduced Graphene Oxide

The rGO was prepared as outlined in [175]. 500 mg of rGO functionalised with octadecylamine (805084, Sigma Aldrich, UK) was sonicated for 20 s in 2.5 ml of xylene to give a homogeneous solution. The optical fibres were dip-coated in this solution, followed by a PDMS overcoat to make a bilayer DD composite as outlined previously.

3.2.2 Characterisation

Prior to optical and US characterisation, the coated optical fibres were examined visually using a stereo-microscope. Coatings were examined for uniform surface morphology, aggregation of the absorber within the composite, and thickness of the deposited coating.

3.2.2.1 Optical Characterisation

Optical characterisation of light is a typical tool in materials studies to obtain the proportion of absorption and transmission by the sample at points throughout the spectra. The interaction of light with media that are absorbing, homogeneous and isotropic is governed by Beer-Lambert's law [32]. This states that the difference in intensity of an incident light beam I_0 on a sample and the emerging light intensity I at wavelength λ is directly related to the properties of that substance, such as attenuation μ_a at the given wavelength λ and sample thickness d (Eq. 3.2).

$$I(\lambda) = I_0 e^{-\mu_a(\lambda)d} \tag{3.2}$$

Assuming an homogeneous and isotropic medium, the absorbance A can be directly obtained from the measured transmittance $T = I/I_0$ using Eq. 3.3.

$$A = log(\frac{1}{T}) \tag{3.3}$$

Assuming a constant thermal expansion coefficient β, the optical absorption is proportional to the pressure generated (see Eq. 2.12).

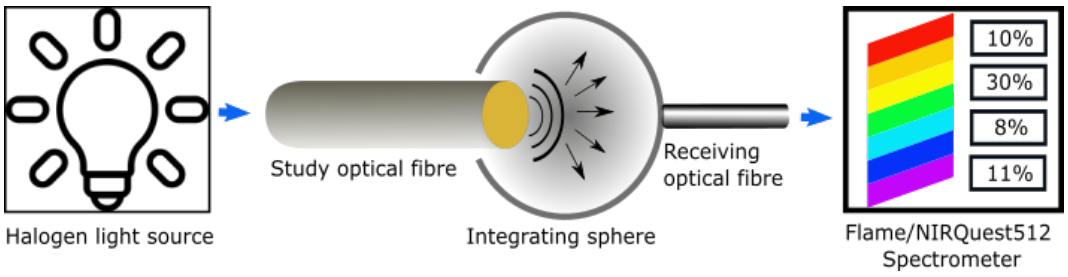

Figure 3.3: Schematic of measurement set-up used for optical characterisation: through-illumination of the fibre using a halogen white light source measured by an integrating sphere and spectrometer.

The wavelength-dependent optical absorption for the dye-PDMS coated fibres was measured between 400 and 1800 nm using a halogen lamp (HL2000 Tungsten Halogen Light Source, Ocean Optics, USA), an integrating sphere, and two spectrometers (Flame $(400-900$ nm) & NIRQuest512 $(700-1800$ nm), Ocean Optics, USA). An uncoated optical fibre was used for reference and a background count was taken for each measurement to remove ambient light and dark counts

(Fig. 3.3). A 'light' and 'dark' measurement was taken for each fibre including the uncoated reference fibre, and the absorbance at each wavelength given by Eq. 3.3. The normalised absorption fraction is then calculated using Eq. 3.4.

$$\alpha = 1 - \frac{\alpha_{light} - \alpha_{dark}}{\alpha_{ref}} \tag{3.4}$$

Here α_{ref} is calculated as:

$$\alpha_{ref} = \alpha_{ref(light)} - \alpha_{ref(dark)} \tag{3.5}$$

Errors in the optical spectra could be caused by background light interference or saturation of light. These risk factors can be addressed by using 'dark' measurements to remove artificial peaks from background light, as well as the use of a blank fibre to calculate the optimal integration time to reduce the risk of saturation.

3.2.2.2 Ultrasound Characterisation

The acoustic characterisation of the fabricated transmitters is carried out at a single point measurement to assess the generated US field in terms of peak-to-peak pressure, spectrum and field profile. The schematic for the measurement set-up is shown in Fig. 3.4.

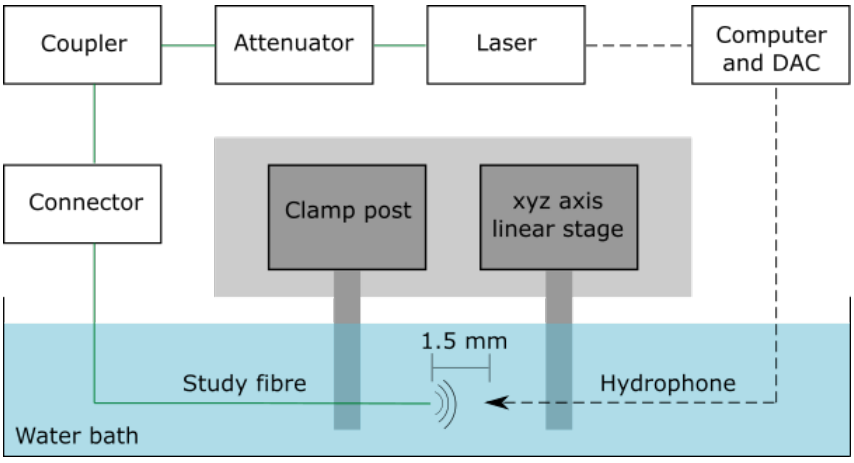

Figure 3.4: Schematic of measurement set-up used for acoustic characterisation.

Two separate pulsed Nd:YAG lasers were used for excitation; one with a wavelength of 1064 nm (pulse width: 2 ns, repetition rate: 100 Hz, Spot-10-500-1064,

Elforlight, UK), and another with a wavelength of 532 nm (pulse width: 10 ns, repetition rate: 100 Hz, FQ-500-532, Elforlight, UK). The pulse energy was measured prior to characterisation measurement using a photodiode detector (Newport, UK), and adjusted to the desired fluence using a rotating Brewster mirror to attenuate the source.

The study fibre was mounted on the stationary clamp stand directly opposite the 200 μm needle hydrophone (Precision Acoustics, UK) with a calibration range $1 - 30$ MHz. This hydrophone was mounted on a 3-axis linear translation stage used to both centre the hydrophone on the US beam and to adjust the hydrophone transmitter separation to ensure that the generated US was measured at a distance of 1.5 mm. The received US pressure generated by the fabricated transmitter was digitised at 14 bits with a sample rate of 100 MS/s (PCI-5142, National Instruments, UK). To obtain the US bandwidth of the study transmitter, a Fourier transform was applied to the acquired time-series, and the hydrophone calibration was applied.

Errors in the acoustic characterisation could be caused several factors. There is an error associated with the digitisation noise which is measured to be less than 0.003 MPa. Assuming the error is constant and the peak-to-peak pressures are sufficiently large, this error can be considered relatively negligible. Potential error can also be introduced by deviance from the central frequency in the source-detector alignment. The Full-Width Half-Maximum (FWHM) of the US profile at short distances is narrow, and therefore the signal maximum can be found relatively easily through trial and error. The estimated error here is less than 5%. The most significant source of error arises from the wavelength-dependent hydrophone calibration which is given by Precision Acoustics to be a maximum of 10%.

3.2.2.3 Photostability Assessment

One of the primary drawbacks of dye-based coatings to date are their poor photostability. To measure the photostability, coatings were continuously exposed to laser pulses for a period of 60 minutes and an US measurement was recorded every 10 s to simulate an imaging scan. The incident laser was set at 100 Hz repetition rate and a pulse energy of 20 μJ.

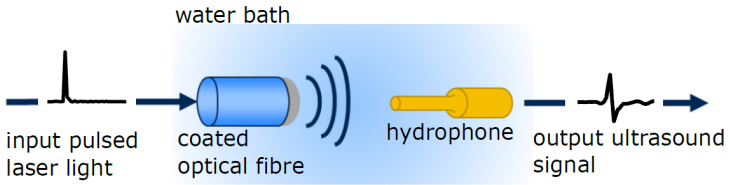

Figure 3.5: Schematic of ultrasound characterisation setup for photostability assessment with input laser pulse and output ultrasound signal.

It is important to note that, while the acoustic characterisation set up here is largely described in Section 3.2.2.2, the hydrophone used is uncalibrated, meaning that the resulting pressure loss is calculated as a percentage drop from the initial measurement. The pressure loss of the calibrated and uncalibrated hydrophone was assessed using a CV composite with a known photostability; it was concluded that the relative pressure loss was sufficiently similar. The use of the uncalibrated hydrophone is to protect the calibrated hydrophone from potential damage caused by direct laser exposure in the event that the composite coating is ablated during long exposure.

3.2.3 OpUS Imaging System

An OpUS imaging system was developed which comprised two elements: an OpUS probe and an imaging console.

3.2.3.1 OpUS Probe

A typical OpUS probe consists of a fibre transmitter in combination with a plano-concave microresonator for receiving signal.

Receiver

The US receiver was fabricated using single-mode optical fibres with core/-cladding diameters of $8/125$ µm (SMF-28, Thorlabs, UK). A plano-concave microresonator was fabricated at the distal end by dip-coating into an optically transparent polymer as described previously [135]. A dielectric mirror was applied to the fibre end prior to the polymer coating, with a second mirror deposited on the outer surface of the polymer. The mirror reflectivities were nominally 98% in the range of $1500 - 1600$ nm. Finally, the plano-concave microresonator was coated in a protective layer (thickness *ca.* 5 µm) of parylene C.

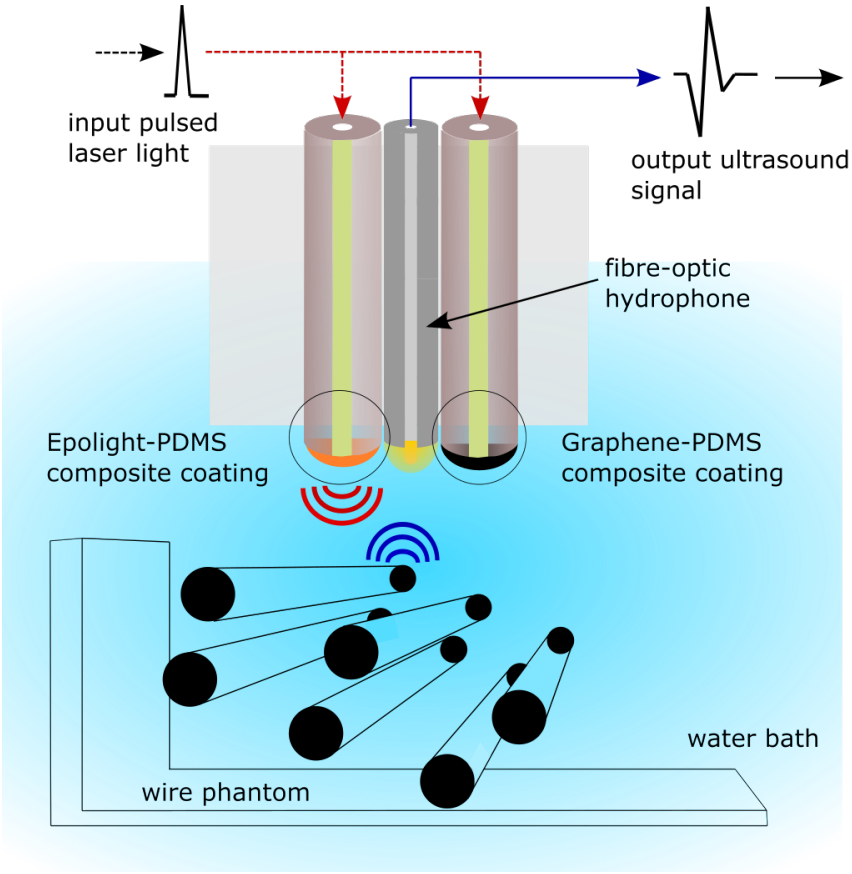

Figure 3.6: Schematic of fibre arrangement for B-mode imaging. Input pulsed laser light (red) is absorbed by one of the composite coatings, generating ultrasound which is subsequently reflected off of the wire phantom. The reflections (blue) are received by a fibre-optic hydrophone.

Imaging Probe

The fabricated transmitters were affixed adjacent to a plano-concave microresonator to provide US generation and reception, respectively (Fig. 3.6).

3.2.3.2 Imaging Console

The console comprised optoelectronic components to both deliver pulsed excitation light to the OpUS transmitter and interrogate the OpUS receiver. The transmitters were coupled to the pulsed Nd:YAG laser for US generation (1064 nm, Elforlight, UK). The plano-concave microresonator was interrogated with a continuous wave laser (Tunics T100S-HP, Yenista Optics, France) with a tuning range of $1500-1630$ nm and a power of 4.5 mW as described in previous studies [140, 175]. The laser was connected via a fibre optic circulator which allowed the reflected sig-

nal to be detected with a photoreceiver. The photoreceiver split the signal into high-frequency ($>$ 500 kHz) and low-frequency ($<$ 50 kHz) components. The low-frequency component was digitised at 16 bits (PCI-6251, National Instruments, UK) and was used to record the transfer function of the microresonator and estimate the optimum bias point. The high-frequency component was digitised at 14 bits with a sample rate of 100 MS/s (PCI-5142, National Instruments, UK) and was used to record the modulation of the reflection induced by the incident acoustic wave. The sensor was biased to the point of the maximum derivative of the interferometer transfer function of the plano-concave microresonator to optimise the sensitivity [176].

3.2.3.3 Data Acquisition

This probe was then clamped to a motorised stage (MTS50/M-Z8, Thorlabs, UK) controlled by a motor controller (TDC001 T-Cube DC, Thorlabs, UK).

Imaging was performed by translating the probe one horizontal step at a time using the motorised stage and acquiring an A-line at each step. Each A-line consisted of a number of sensor data points corresponding to the required depth d. This is calculated using the speed of sound in the medium c_s and a sampling interval dt of $1.0e^{-8}$ as:

$$d = \frac{n_{samples}\, c_s\, dt}{2} \tag{3.6}$$

The A-lines were then concatenated to form a complete data set. Imaging was performed sequentially with the comparative transmitters; each scan using the Epolight-PDMS transmitter was immediately repeated with the rGO-PDMS transmitter to ensure direct comparison.

3.2.3.4 Image Processing

The data was bandpass filtered (4th order Butterworth, $1.5 - 40$ MHz), followed by the application of a cross-talk algorithm, as described previously [177] Briefly, each scan was fitted with a general linear model of three components: a local average obtained from 40 scans, the derivative of the local average to allow for

temporal offsets, and a constant term. The modelled cross-talk was then subtracted from the signals. This was followed by image reconstruction using the k-Wave toolbox, as described previously [77]. Briefly, for image reconstruction, a fast Fourier transform was computed on both dimensions (t, y) converting the raw data to wavenumber-frequency space. Subsequently, the data was then mapped to wavenumber-wavenumber space using the dispersion relation for a plane wave. Finally, an inverse Fourier transform was then computed back to the spatial domain (x, y). The signal envelope was found using the absolute value of the Hilbert transform followed by a log transformation.

3.2.3.5 Imaging Targets

A custom phantom comprising a series of parallel tungsten wires (diameter: 27 μm) mounted on a plastic frame was used to assess the imaging resolution. This phantom appears in reconstructed images as a series of Point Spread Function (PSF)s which can be used to measure the resolution of the imaging system. The imaging targets were fixed in position in a water bath (Fig. 3.6), while the OpUS probe was translated relative to the target. Data acquisition was carried out using A-line spacings of $25 - 200$ μm. For each of the reconstructed images, the axial and lateral resolution were calculated as the FWHM values of the PSFs that represented the tungsten wires in the images.

The SNR of the imaging targets was calculated for each reconstructed image. First, a Region of Interest (ROI) representing noise was identified in an area of the image where no imaging target was present, with the mean intensity of this ROI used as the noise value. Next, ROIs were selected around the imaging targets, such as the PSFs from the wire phantom, where the maximum intensity within these regions was taken as the signal. The SNR was then determined using these signal and noise values.

Imaging of *ex vivo* swine aorta tissue (Medmeat, UK) was carried out to ascertain the potential for visualising biological structures. In preparation for imaging the vessels were cut parallel to their longitudinal axis and fixed to a cork mount with the inner surface facing up towards the US probe (Fig. 3.7). The cork mount and

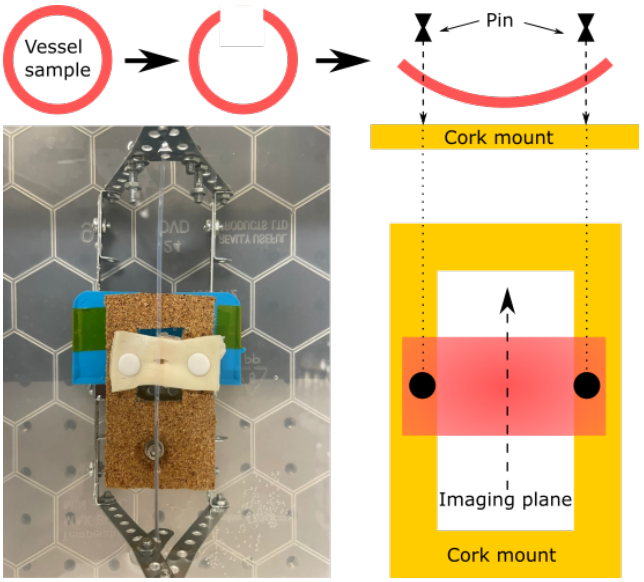

Figure 3.7: Schematic of aorta tissue arrangement for *ex vivo* B-mode imaging.

tissue were placed in the water bath.

3.3 Study I: PDMS Composites with Photostable NIR Dyes

One particular area of interest in the fabrication of miniaturised OpUS devices in the capacity to integrate complementary modalities. However, combing modalities requires carefully engineered composite materials with wavelength-selective absorption [3, 104, 141, 119]. Previous research has demonstrated the use of CV or AuNP embedded in a PDMS host for co-registered US and PA imaging [3]. However, these composites suffered from poor photostability under prolonged laser exposure. Here, the use of a highly-photostable NIR-absorbing dye (Epolight 9837, Epolin, USA) was explored. This dye was recommended for absorption of 1064 nm laser light as well as demonstrating a high optical transmission in the visible range [178]. This wavelength-selective nature is highly desirable for combining complementary modalities with OpUS imaging. Several composite coatings were fabricated to assess the optimal dye concentration and manufacturing method; these are detailed in Table 3.1. Additionally, comparable composites were fabricated; these are also detailed in Table 3.1.

3.3.1 Fabrication

Seven composite coatings were fabricated; four using Epolight 9837 with varying concentration of dye by weight (Table 3.1: 2.5A, 5A, 10A), one using pure CV (CVO) for comparison as previous studies show this dye is susceptible to photobleaching [3], and two using CV stabilised with AuNP (CVAUB, CAVUU). For each composite coating, five US generators were fabricated to test for consistency. The US generation here was characterised at a pulse energy of 20 μJ, which corresponded to a fluence deposited within the coating of 15.9 mJ/cm^2.

3.3.2 Results

3.3.2.1 Microscope Images

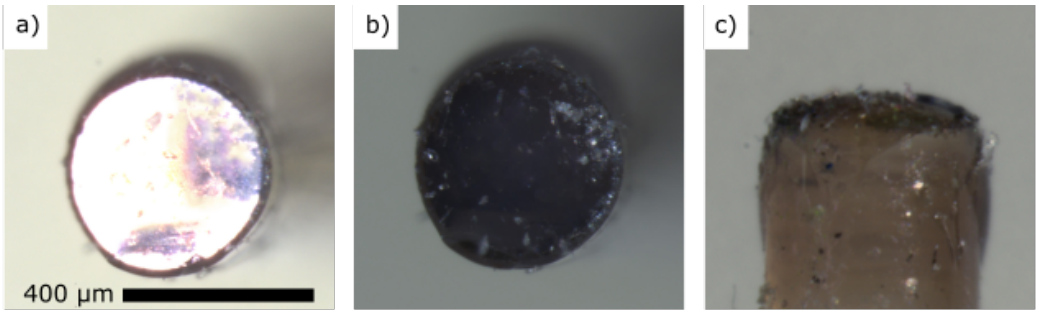

Figure 3.8: Stereo-microscopy images of 2.5A Epolight composite coated optical fibre. a) End-view with through illumination. b) End-view with no through illumination. c) Side-view. Scale bar: 400 μm.

The microscope images were examined for coating uniformity and thickness (Fig. 3.8). Fibres with excessively thick coating layers ($\geq$ 0.15 mm) or visible agglomerations of optical absorber were eliminated prior to characterisation. No visible difference was noted in the colour or consistency in the range of Epolight-PDMS coatings.

3.3.2.2 Optical Absorption

	@ 1064 nm	@ 532 nm	@ 400 – 800 nm
2.5A	78 ± 4	67 ± 7	65 ± 8
5A	86 ± 2	73 ± 5	72 ± 4
10A	96 ± 2	86 ± 7	86 ± 6
CVO	29 ± 11	66 ± 14	51 ± 15
CVAUB	31 ± 11	80 ± 7	40 ± 17
CVAUU	36 ± 12	83 ± 6	39 ± 20

Table 3.2: Optical absorption of Epolight and CV composite coatings at 1064 and 532 nm, as well as the average absorption in the visible range.

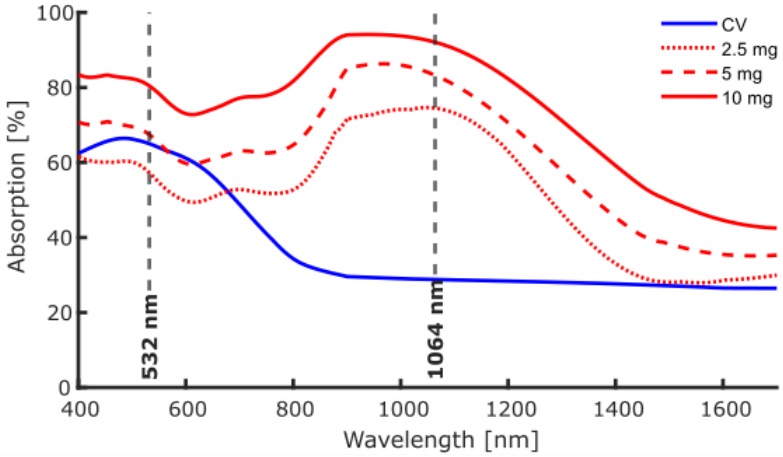

Figure 3.9: Optical absorption spectra for the CV (blue solid line) and Epolight composites (2.5A: red dotted line, 5A: red dashed line, 10A: red solid line).

The CV and Epolight dyes exhibited different optical absorption profiles (Figure 3.9). The Epolight composites exhibited an optical absorption peak at *ca.* $900 - 1100$ nm for all dye concentrations (Table 3.2, Figure 3.9) with a maximum of $> 90\%$ for the composite with the highest concentration of dye (10 mg).

For wavelengths shorter than 900 nm and longer than 1100 nm the optical absorption decreased. The optical absorption at all wavelengths decreased proportionally with dye concentration for the Epolight composites. The CV composite exhibited an absorption peak at *ca.* 532 nm with a value *ca.* 66%. The optical absorption decreased for longer wavelengths to a value $< 30\%$. The CVAuNP demonstrated an absorption peak at 532 nm with a value of *ca.* 80%. The optical absorption decreased for longer wavelengths; it is of note that these demonstrated a significant variability.

3.3.2.3 Ultrasound Generation

	Pressure [MPa]	Bandwidth [MHz]
2.5A	0.46 ± 0.14	16.0 ± 2.7
5A	1.03 ± 0.13	20.7 ± 3.3
10A	0.92 ± 0.17	20.5 ± 2.3
CVO	0.31 ± 0.02	10.6 ± 1.6
CVAUB	0.42 ± 0.24	8.23 ± 0.46
CVAUU	1.69 ± 0.04	16.25 ± 0.18

Table 3.3: Ultrasound generation properties of Epolight and CV composite coatings using a 20 μJ incident pulse energy at a transmitter-receiver distance of 1.5 mm.

The Epolight composites exhibited peak-to-peak US pressure with values up to 1 MPa, with corresponding -6 dB US bandwidths *ca.* 20 MHz (Figure 3.10). The generated US pressure was found to increase with increasing dye concentration from 2.5 mg to 5 mg with maximum values of 0.46 and 1.03 MPa, respectively. For the highest dye concentration of 10 mg, the peak-to-peak pressure was found to decrease slightly, with a value of 0.92 MPa.

The CV composites used for reference in general created narrower bandwidths

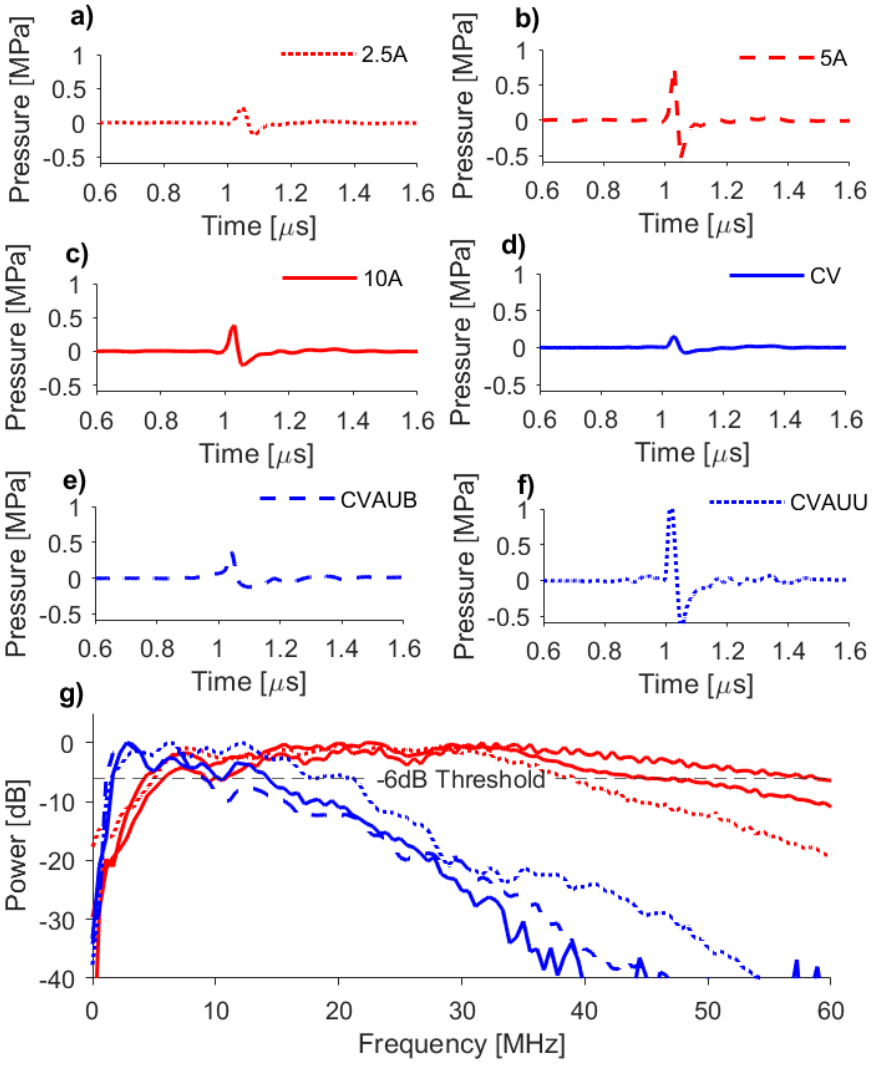

Figure 3.10: a) - f) Ultrasound time-series for the composite coatings, including Epolight coatings: a) 2.5A - red dotted line, b) 5A - red dashed line, c) 10A - red solid line and CV coatings: d) CV: blue solid line, e) CVAUU: blue dashed line, f) CVAUB: blue dotted line. g) Corresponding ultrasound power spectra for the composite coatings.

(Table 3.3, Figure 3.10). While the CVO and CVAUB composites generated lower peak-to-peak pressures than the Epolight composites (0.31 and 0.42 MPa respectively), the CVAUB composite generated the largest pressure overall (Table 3.3: 1.69 MPa).

3.3.2.4 Photostability

	2.5A (@1064 nm)	5A (@1064 nm)	10A (@1064 nm)
Loss[%]	22.6 ± 2.5	15.2 ± 0.7	13.0 ± 0.6
	CVO (@532 nm)	CVAUB (@532 nm)	CVAUU (@532 nm)
Loss [%]	58.6 ± 3.3	35.2 ± 3.5	20.2 ± 2.2

Table 3.4: Normalised pressure loss of Epolight and CV composite coatings using a 20 μJ incident pulse energy at a transmitter-receiver distance of 1.5 mm over a period of an hour.

The photostability of the Epolight composites was compared with CV composites. Initially, a direct comparison was conducted between a CVO composite and an Epolight composite, both excited by a 532 nm source. The Epolight composite used in this comparison contained 10 mg of dye, which, as shown in Fig. 3.9, exhibited a similar optical absorption at 532 nm to the CVO composite. With a pulse energy of 20 μJ, the peak-to-peak pressure generated by the CV composite fell by 68% in 1 hour, compared with a reduction by 7% for the 10 mg Epolight composite.

Subsequently, the photostability of the variations of AiO Epolight and CV composites was compared (Table 3.4, Fig. 3.11). All Epolight concentrations demonstrated good photostability at 1064 nm, with the pressure dropping by 22%, 15% and 13% for the 2.5A, 5A and 10A composites, respectively. By comparison, the CV composites performed poorly under constant exposure, with normalised pressure losses of 58%, 35% and 20% for the CVO, CVAUB and CVAUU composites respectively.

3.3.3 Discussion

3.3.3.1 Epolight Concentrations

It was found that by reducing the concentration of the Epolight dye, the optical absorption in the range 400 to 800 nm and for wavelengths > 1200 nm could be reduced whilst maintaining a relatively high optical absorption at 1064 nm for US generation. The lower optical absorption at wavelengths from 400 to 900 nm and > 1100 nm is well-suited to a variety of complementary modalities, including PA imaging and optical ablation [142, 140]. However, whilst the presence of these

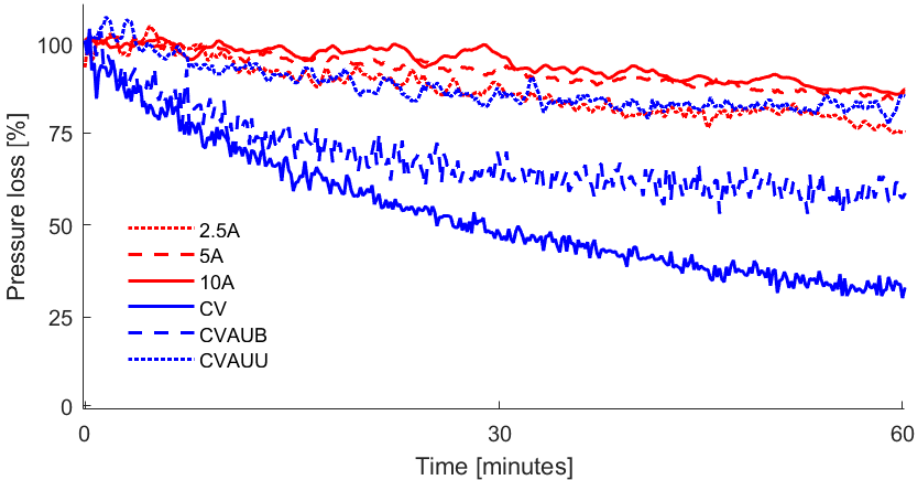

Figure 3.11: Normalised photostability for the Epolight composites compared to the CV composites.

optical absorption windows are promising for multi-modality imaging, further optimisation is needed to reduce the absorption on either side of the peak at 1064 nm. This will be explored further in the following studies, using different concentrations and alternative fabrication methods, such as the bilayer approach highlighted in [3].

The US generated by the composites was comparable with that used in previous studies for imaging [109, 179, 139]. Composite 2.5A generated lower US pressures than the 5A, as expected from the corresponding decrease in optical absorption. However, for the higher dye concentration of 10A, the peak-to-peak pressure was found to decrease. This may be due to increased US attenuation within the coating caused by the higher dye loading. US bandwidths up to 20 MHz were achieved, sufficient for high resolution US imaging. However, the lower dye concentration in 2.5A exhibited narrower bandwidths than other composites. This could be caused by the longer absorption length, leading to a wider temporal profile in the generated US pulse (see Chapter 2 Section 2.2.2).

3.3.3.2 Epolight vs CV

In general, the Epolight composites here outperformed the CV composites in terms of US characteristics and photostability. It should be noted however, that previous studies with CV have achieved higher pressures and bandwidths [3] than that of the

CVO used here.

Crucially, the photostability of the Epolight composites was measured and compared with the CV composites. CVO has previously been used for *ex vivo* imaging, but demonstrated poor photostability [3]. All Epolight composites exhibited acceptable photostability compared to CVO, with pressure decreasing by only approximately 10% over one hour, in contrast to a 58% drop for the CVO composite over the same period. Notably, the photostability measurements in Fig. 3.11 show considerable variation rather than a consistent decline, and the overall pressure loss trend for Epolight composites remains relatively flat, indicating minimal degradation. In contrast, the CVO composite demonstrates a significant decrease.

It is important to note that the hydrophone used for sensing was uncalibrated, likely introducing some error. Additional sources of error may include movement of either the transmitter or the hydrophone during exposure, as well as heating of the PVDF needle hydrophone over the hour-long period. Variations in ambient temperature could also affect the hydrophone's sensitivity, potentially altering the recorded pressure values. Electrical noise or interference from surrounding equipment may introduce signal fluctuations, while inconsistencies in the alignment of the acoustic beam with the hydrophone over time could further impact the accuracy of the measurements. Finally, minor fluctuations in the light source intensity or the optical stability of the experimental setup may also contribute to variations in the recorded data. As such, it can be concluded that the loss observed in the Epolight composites is largely within the expected experimental error range.

Of note is the impact of adding AuNP to the CV-PDMS composites. Here, the CVAUU outperforms both the CVO and CVAUB composites in terms of photostability, as well as the Epolight composites in terms of US pressure generation. This is likely due to the larger percentage of AuNP particles in the composite; the unbacked fabrication (CVAUU) allows infusion of AuNP from both sides in comparison with the single-sided infusion in the backed fabrication (CVAUB). The larger concentration of AuNP increases the SPR, where the light incident on the surface of metallic Nanoparticles (NPs) causes the electrons in the conduction band to resonate, thus

enhancing the optical properties such as optical absorption μ_a [180]. This increase in optical absorption is likely responsible for the increased peak-to-peak pressure generated (see Eq. 3.3). Further, the heightened absorption of the AuNP is likely responsible for the reduced pressure loss under constant exposure; here, the AuNP acts as a photoprotector for the host absorber [181]. However, the amount of AuNP incorporated as a photoprotector, as well as the size of the NPs, has a considerable effect on the location of the absorption peak, for example, larger NPs will create a 'red-shift' to longer wavelengths, whilst smaller NPs will create a 'blue-shift' in the opposite direction. A significant change in absorption peak for an incident light-source of a fixed wavelength could mean that the improvement in absorption created by the SPR is negated by the shift of the peak.

3.4 Study II: Optimising of Manufacturing Method for Dichromacity

3.4.1 Coating Methodology

After determining that the transmission percentage in the NIR and visible range for the coatings produced using AiO was inadequate for wavelength-selective multi-modality, an alternative fabrication method was explored. The optical density spectrum provided by the manufacturer of Epolight 9837 in polycarbonate indicates a sufficiently low absorption at all wavelengths ≤ 1000 and ≥ 1200 nm (Fig. 3.1). However, this was not observed in the previously fabricated coatings, possibly due to interactions with xylene and PDMS during the AiO coating process. In this study, an alternative approach was employed to assess the impact of minimising the absorbers interactions.

3.4.1.1 Fabrication

To assess the impact of coating methods, DD and AiO coatings were fabricated (Fig. 3.2). Coatings were fabricated for each method using three concentrations of optical absorber (Table 3.1: 5A, 5D, 10A, 10D, 15A, 15D). As with the previous study, five US generators were fabricated of each type to test for consistency. The

US generation here was characterised at a pulse energy of 20 µJ.

3.4.1.2 Results

	@ 1064 nm	@ 400 – 800 nm	Pressure [MPa]	Bandwidth [MHz]
5A	86 ± 2	72 ± 4	1.03 ± 0.13	20.7 ± 3.3
10A	91 ± 2	78 ± 6	0.92 ± 0.17	20.5 ± 2.3
15A	95 ± 2	71 ± 15	1.21 ± 0.15	23.1 ± 2.7
5D	59 ± 7	46 ± 12	0.62 ± 0.23	29.3 ± 3.2
10D	76 ± 4	76 ± 15	1.01 ± 0.45	29.2 ± 2.8
15D	96 ± 2	81 ± 8	1.30 ± 0.36	31.6 ± 3.6

Table 3.5: Optical absorption of Epolight AiO and DD composite coatings at 1064 nm and the average absorption in the visible range, and corresponding ultrasound generation properties using a 20 µJ incident pulse energy including peak-to-peak pressure and corresponding −6 dB bandwidth.

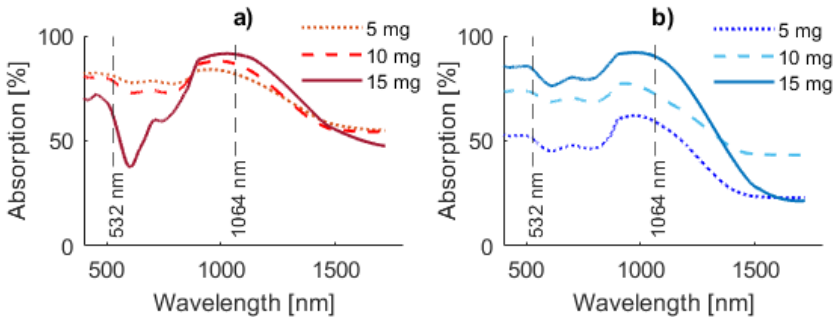

Figure 3.12: Optical absorption spectra for the a) AiO and b) DD composites with Epolight concentrations of 5 mg (dotted line), 10 mg (dashed line), and 15 mg (solid line).

All US transmitters exhibited an optical absorption peak at *ca.* 900 – 1100 nm (Table 3.5, Fig. 3.12) with a maximum of 96% demonstrated by both 15 mg transmitters. The optical absorption decreased for wavelengths ≤ 900 nm and ≥ 1100 nm for all composites. The DD composites showed a distinct relationship between Epolight concentration and optical absorption; this is demonstrated to a lesser extent with the AiO composites.

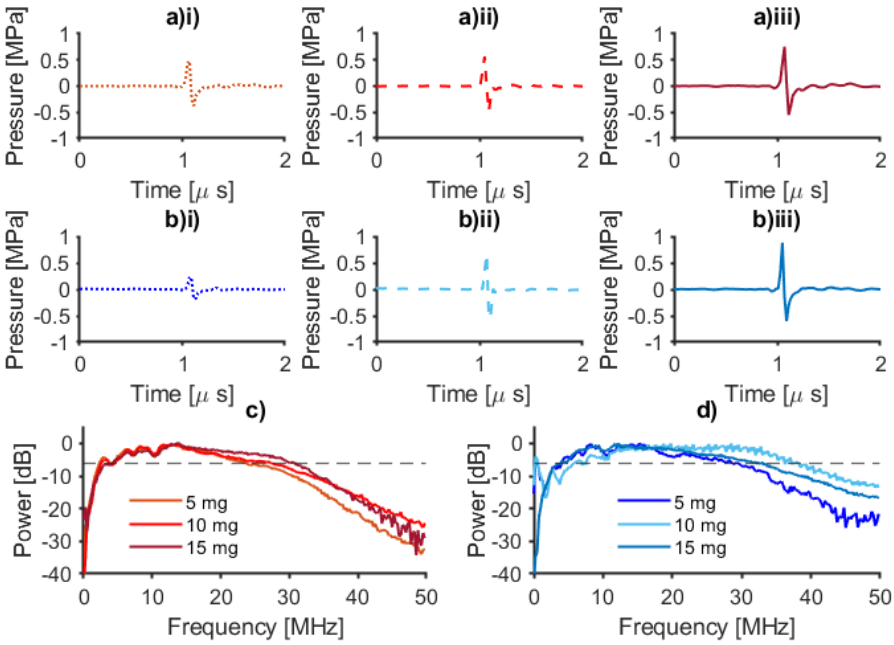

Figure 3.13: Ultrasound time-series for Epolight a) AiO and b) DD composite coatings (5 mg: dotted line, 10 mg: dashed line, 15 mg: solid line). Corresponding ultrasound power spectra for c) AiO and d) DD composite coatings.

The AiO composites exhibited peak-to-peak US pressure with values up to 1.2 MPa, with corresponding -6 dB US bandwidths *ca.* 21 MHz (Table 3.5, Fig. 3.13). The generated US pressure was largest for the largest dye concentration 15A. However, the increased pressure with dye concentration was not shown to be linear, with the lowest pressure shown by 10A (Table 3.5).

The DD composites, in comparison, demonstrated peak-to-peak pressures of up to 1.3 MPa, with a distinctly linear correlation between Epolight concentration and pressure generation. The corresponding -6 dB bandwidth was measured at up to 31 MHz (Table 3.5, Fig. 3.13).

	5A	10A	15A
Loss [%]	15.2 ± 0.7	13.0 ± 0.6	10.3 ± 0.2
	5D	10D	15D
Loss [%]	20.1 ± 0.3	16.2 ± 0.3	12.5 ± 0.3

Table 3.6: Normalised pressure loss of AiO and DD Epolight composite coatings using a 20 µJ incident pulse energy at a transmitter-receiver distance of 1.5 mm over a period of an hour.

The photostability trend here shows that, for both manufacturing methods, concentration of the optical absorber is inversely proportional to the pressure loss. The DD coatings experienced a marginally larger pressure loss than the AiO coatings. The lowest loss was observed in 15A (*ca.* 10%), while the highest loss occurred in 5D (*ca.* 20%).

3.4.1.3 Discussion

The best performing composite here was 15D, both in terms of optical absorption at the US generating wavelength and the corresponding acoustic profile. Of particular note was the drastic increase in bandwidth shown by the DD composites in comparison with the AiO composites (Table 3.5). As the optical pulse length remains constant, this difference in bandwidth is likely due to the difference in absorption path length [89] (see Section 2.2.4). The DD method creates a bilayer composite, meaning that the optical absorber sits against the distal face of the fibre, thus decreasing the heating time. However, a thin coating, whilst exhibiting a broad bandwidth, is also more susceptible to heat damage (Eq. 2.8). This is demonstrated by the DD composites; a broader bandwidth was generated, but a slightly lower photostability than the AiO method was exhibited.

The photostability results also showed that pressure loss increased as the concentration of Epolight decreased. This effect is likely due to the impact of the thickness of the optical absorber within the composite coating on photobleaching. Photobleaching occurs when the molecules are excited from the singlet state to the triplet state but are unable to fluoresce [182]. The amount of bleaching can be controlled by reducing incident intensity, increasing the absorber concentration, or reducing incident frequency [183]. With lower concentrations, as particles near the surface photobleach under laser pulses, a greater proportion of light passes through rather than being absorbed. In contrast, with higher concentrations, photobleaching at the surface is compensated by a denser agglomeration of particles deeper within the composite. This is supported by both the optical and acoustic behaviour of the composites: lower concentrations demonstrate poorer absorption and lower peak-to-peak pressure (Table 3.5). This could also provide an explanation for the differ-

ence between AiO and DD composites; since the dye is distributed throughout the PDMS matrix in an AiO composite, laser incidence and therefore photobleaching would occur gradually throughout the volume, leading to a less noticeable performance loss. In comparison, the absorber in a DD composite is confined to a single layer, so laser incidence and photobleaching would be more concentrated in that layer, potentially leading to a sharper performance loss than the AiO counterpart.

An interesting observation from the photostability measurements is the apparent recovery of the composites. A pressure loss of just 10% would negatively impact the SNR of an imaging scan. However, after each fibre sample underwent photostability testing, the acoustic spectra in subsequent tests returned to their initial values. Additionally, the probe used in Chapter 4, which utilised an Epolight-PDMS composite coating for over a year, compiling many hours of imaging time, theoretically should have experienced complete degradation of the coating. Instead, the pressure generated remained stable until it suddenly degraded very quickly after *ca.* one year of use. This behaviour is likely due to the number of excitation cycles required for full bleaching. This is defined approximately as:

$$lifetime[s] = I_0 tC \tag{3.7}$$

where I is the incident intensity, t is the exposure time, and C is the number of excitation-relaxation cycles that the molecule is capable of [182]. Theoretically, each cycle has an equal probability of causing photobleaching given a constant environment, but dyes that are considered photostable can, by definition, withstand a larger number of cycles. This combination of recovery and sudden degradation after a year of use suggests that photobleaching is not occurring during the hour-long tests. Instead, the observed pressure loss is more likely due to experimental errors. As noted in Section 3.3.3.2, the hydrophone itself may contribute to inaccuracies, given the uncertainty introduced by its uncalibrated state. Additional sources of error could include movement of the transmitter or hydrophone during exposure, heating of the hydrophone, or fluctuations in light source intensity. The behaviour of Epolight dyes across the concentrations and manufacturing methods implied that

the lifetime of Epolight is sufficient for application in minimally invasive imaging, particularly in scans that require ≤ 1 hour to acquire.

The most promising optical spectra for multi-modal imaging was shown by 15D with a transmission of 75% in the NIR range. Indeed, all DD composites exhibited a higher transmission in the NIR range than their AiO counterparts. Multi-modal imaging requires carefully designed optical profiles, with high absorption ($\geq$ 80%) at the designated US wavelength and low absorption at other wavelengths [3]. It follows, therefore, that the designated transmission windows should transmit $\geq$ 80% of the incident light. As stated in Table 1.1, the optimal excitation wavelengths for complementary endogenous fluorescence GI imaging is *ca.* 400 nm for targeting porphyrins and *ca.* 350 nm for targeting collagen III. Despite the optical density profile of Epolight showing *ca.* 90% transmission at these wavelengths, this is not exhibited by the optical spectra of any of the composites. Instead, a promising secondary modality is using exogenous fluorescence imaging, such as Indium-based fluorescence, which has an excitation wavelength of 1650 nm [4]. However, the transmission of 75% shown by 15D is not sufficient for this imaging method.

It is interesting to note that both 15A and 15D demonstrate differing absorption profiles than either of the 10 or 5 mg coatings. The sample size, as well as the consistent variation in generated pressures, implies that this is unlikely to be due to a fabrication error. This behaviour requires further investigation but is likely to be related to the interaction between the dye and the xylene solvent. Alternatively, this could be related to the saturation point of the xylene, meaning that a proportion of the dye molecules are not dissolved and therefore following an absorption behaviour more similar to that of the manufacturers optical density (Fig 3.1). This is supported by the pressure generated by the transmitters; for both AiO and DD composites, the variation in the maximum pressure reported by any concentration overlaps with other concentrations (Table 3.5). However, this variation requires further investigation.

3.4.2 Impact of Sonication

A key factor in the reliable manufacturing of US generation coatings is the homogeneity of the composite. The previous studies detailed in this chapter have shown significant variations in both optical and acoustic spectra, especially in the pressure generated, where the differences are substantial enough to overlap with other concentrations. Here, the impact of sonication on composite homogeneity is assessed.

Sonochemistry is the enhancement of chemical reactions using US, almost exclusively in liquids [184]. Here, kinetic energy is introduced to the solution through acoustic cavitation: the formation, growth, and implosive collapse of bubbles in a liquid [185]. This has been used previously to dissolve organic compounds in water with great success [186], so could theoretically be used to aid in the dissolving of agglomerations of dye in the composite coatings here.

3.4.2.1 Fabrication

Here, 12 batches of composites were fabricated: three batches each of 5A, 5D, 10A and 10D. Of these, one batch from each composite was not sonicated, one was sonicated for 20 s at 120 W and 20 kHz, and one was sonicated twice for 10 s at 120 W and 20 kHz (Fisherbrand Sonic Dismembrator, Fisher Scientific, USA). Only the Epolight-xylene solution was sonicated in the case of the DD composites.

3.4.2.2 Results

Sonic.	Param.	5A	5D	10A	10D
0 s	@1064 nm [%]	86 ± 2	59 ± 7	91 ± 2	76 ± 4
	Pressure [MPa]	1.03 ± 0.13	0.62 ± 0.23	0.92 ± 0.17	1.01 ± 0.45
	Bandwidth [MHz]	20.7 ± 3.3	29.3 ± 3.2	20.5 ± 2.3	29.2 ± 2.8
20 s	@1064 nm [%]	78 ± 9	61 ± 3	88 ± 7	80 ± 3
	Pressure [MPa]	0.88 ± 0.33	0.81 ± 0.13	0.98 ± 0.20	1.10 ± 0.25
	Bandwidth [MHz]	14.6 ± 3.5	30.5 ± 3.0	15.0 ± 3.2	29.8 ± 2.9
10 s x2	@1064 nm [%]	82 ± 7	62 ± 2	88 ± 5	79 ± 3
	Pressure [MPa]	0.89 ± 0.25	0.82 ± 0.15	0.92 ± 0.19	1.08 ± 0.22
	Bandwidth [MHz]	15.8 ± 2.8	30.8 ± 3.2	15.5 ± 2.9	30.2 ± 2.5

Table 3.7: Average absorption percentage at 1064 nm, peak-to-peak pressure, and corresponding bandwidth of both hand-mixed, sonicated and twice-sonicated Epolight composites of both AiO and DD manufacturing at concentrations of 5 mg and 10 mg.

3.4.2.3 Discussion

The primary concern with using sonication here was the premature curing of the PDMS. As shown in Section 2.2.4, the thickness of the coating directly impacts the potential bandwidth generation. By partially curing the PDMS prematurely, the viscosity of the solution increases, which affects the thickness of the resulting coating (see Section 3.2.1.1). This is demonstrated by the bandwidths given by the AiO coatings that underwent sonication; the bandwidth of the manually mixed AiO coating was *ca.* 20 MHz, while the sonicated AiO coatings showed bandwidths of *ca.* 15 MHz. The thicker coatings caused by a higher viscosity is likely to attenuate more of the laser incidence, as well as having a larger thermal diffusion distance, therefore emitting a narrow US bandwidth [89]. The second sonication method involved a shorter sonication duration with a rest period in between to minimise the potential curing of the PDMS. However, the bandwidths observed were similar enough to those from the first sonication method to suggest that curing was still occurring.

The peak-to-peak pressures of the sonicated AiO coatings were also lower than the manually mixed counterparts. This is also likely due to the overall thickness of the coating. However, this decrease was less noticeable; indeed, the measured pressures of the sonicated coatings were well within the variance shown by the manually mixed coatings. Additionally, the optical absorption was sufficiently similar across the AiO coatings to imply that sonication had no discernible impact. However, the variance for both the optical absorption and the peak-to-peak pressure increased for the sonicated coatings. This is, again, likely due to partial curing; the use of a probe sonicator likely increases the viscosity of the solution in direct contact with the probe, while having less impact on the outer edges of the test tube. This would create variation within the batch of dip-coated probes. It was noted in Section 3.3 that the relationship between concentration and factors like optical spectra and acoustic pressure was not linear; it was theorised that this was due to saturation of the dye within the solution. However, the absorption and acoustic pressure here fits a linear correlation when considered with the data from 3.4. This implies that, while the so-

lution had not reached saturation, a higher concentration was less easy to disperse, and agglomerations were more likely. Sonication, while creating a thicker coating, does seem to improve the dispersion of the dye within the solution.

The sonication had a positive impact on the DD composites, both in terms of the measured optical and acoustic parameters, and the corresponding variance. Only the bandwidth appeared unaffected; this was expected as no sonication of the PDMS was carried out. However, the improvement shown in optical absorption and peak-to-peak pressure was within the variance of the manually mixed composites for both 5D and 10D. However, the variance reduced by *ca.* 50%. This is likely due to an improvement in the homogeneity and path length of the absorption layer of the bilayer composite.

It can be understood that, in general, sonication does not necessarily significantly improve the overall properties of the DD composite, but the improvement in variance given by the sonicated solutions in comparison with the manually mixed solutions indicates that sonication does improve the manufacturing process. It was concluded to continue the use of sonication in further studies using DD composites.

3.5 Study III: B-Mode Ultrasound Imaging

This study is based on work published in [5]. Here, a 15D Epolight-PDMS transmitter is compared with a previously used rGO-PDMS [175] (Table 3.1: rGO) in terms of optical and acoustic spectra, as well as use in B-mode imaging of both a tungsten wire phantom and *ex vivo* swine aorta tissue.

3.5.1 Methods

3.5.1.1 Characterisation

The coated fibres were examined visually using a stereo-microscope (Fig. 3.14). Subsequently, the optical absorption was measured for wavelengths of 400 - 1800 nm (Section 3.2.2.1), followed by acoustic characterisation (Section 3.2.2.2). Here, the laser had a pulse energy of 20 μJ, corresponding to an incident fluence of 15.9 mJ/cm^2 on the composite coating. The generated US was measured at a distance of 1.5 mm from the coating using a 200 μm needle hydrophone (Precision

Acoustics, UK) with a calibrated range 1 – 30 MHz.

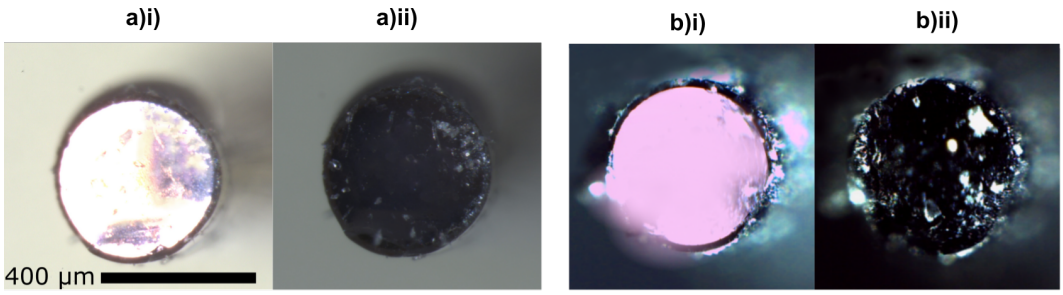

Figure 3.14: a) Stereo-microscope image of distal face of Epolight-PDMS transmitter i) with through-illumination and ii) unlit. Scale bar: 400 µm. b) Distal face of rGO-PDMS transmitter i) with through illumination and ii) unlit.

3.5.1.2 B-Mode Imaging

Both the rGO and 15D Epolight transmitters were combined with a plano-concave microresonator to create a fibre-optic OpUS probe (Section 3.2.3.1). The transmitters were subjected to a laser pulse energy of 25 µJ. This probe was used for acquiring B-mode images of both a tungsten wire phantom (Fig. 3.6) and *ex vivo* swine aorta tissue (Fig. 3.7). The images of the wire phantom were analysed for both SNR and resolutions over a range of depths and A-line spacings.

3.5.2 Results

3.5.2.1 Characterisation

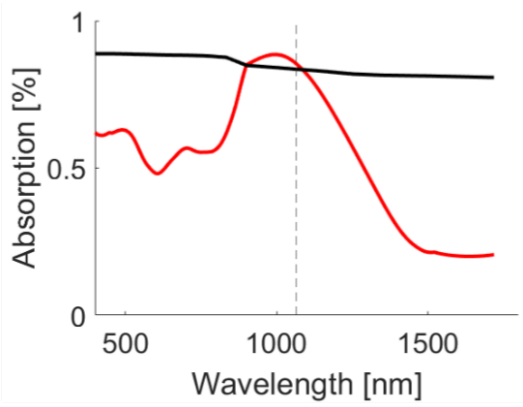

Figure 3.15: Optical absorption spectra of Epolight-PDMS 15D (red line) and rGO-PDMS (black line).

The microscope images were examined for coating uniformity and thickness (Fig. 3.14a-b). Fibres with excessively thick coating layers (> 0.15 mm) or visible agglomerations of optical absorber were eliminated prior to characterisation.

The rGO and Epolight 15D exhibited different optical absorption profiles (Fig. 3.14c). The Epolight composite exhibited an optical absorption peak of *ca.* 95% at *ca.* $900-1100$ nm while demonstrating $< 30\%$ absorption at wavelengths > 1100 nm and *ca.* 50% absorption at wavelengths < 900 nm. The rGO composite, in comparison, exhibited a broadband absorption of *ca.* $90\% \pm 5\%$ at all wavelengths.

The Epolight-PDMS 15D composite exhibited peak-to-peak US pressure of 1.7 MPa (Fig. 3.16a)i)) with corresponding -6 dB US bandwidths 35 MHz (Fig. 3.16b)). In comparison, the rGO-PDMS composite generated US pressures of 1.3 MPa (Fig. 3.16a)ii)) with a bandwidth of 32 MHz (Fig. 3.16b).

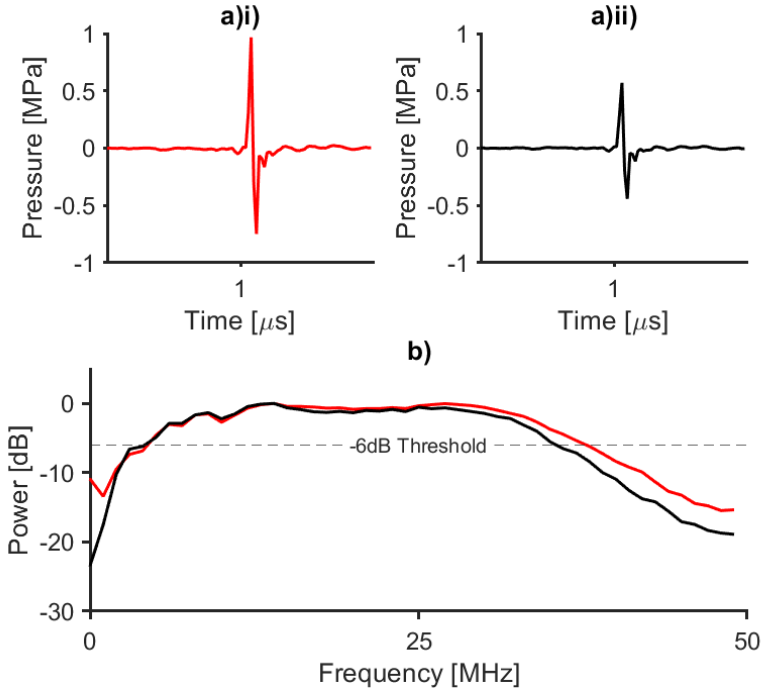

Figure 3.16: a) Transmitted ultrasound time-series measured at 1.5 mm for (i) Epolight-PDMS and (ii) rGO-PDMS coatings. b) Corresponding ultrasound power spectrum.

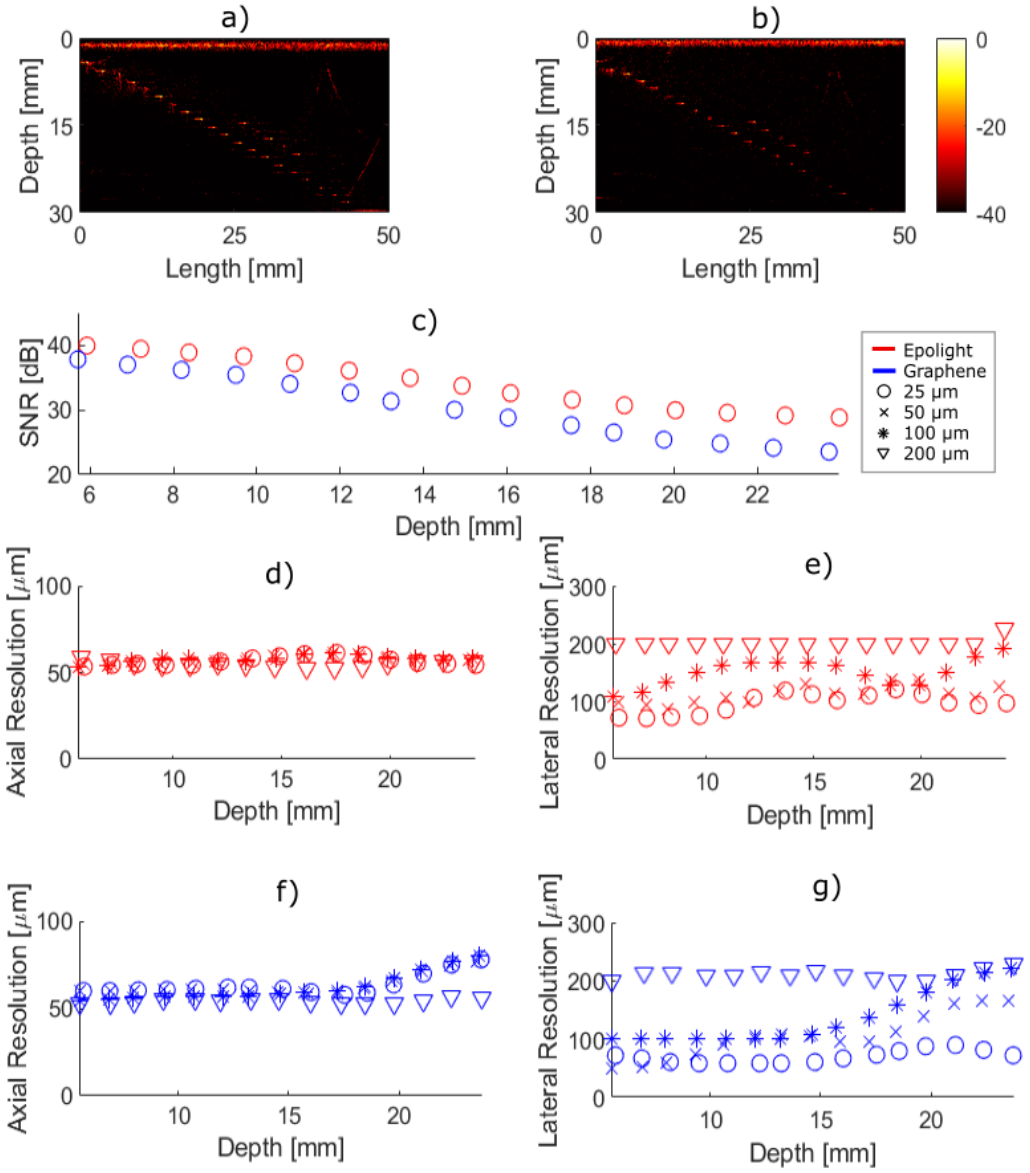

Figure 3.17: B-mode optical ultrasound images of custom 27 µm resolution phantom using a FP hydrophone in conjunction with a) Epolight-PDMS transmitter and b) rGO-PDMS transmitter. c) SNR measurements over depth. d) Axial and e) lateral ultrasound resolutions for the Epolight-PDMS transmitter. f) Axial and g) lateral ultrasound resolutions for the rGO-PDMS transmitter.

3.5.2.2 Resolution Study

All phantom PSF's were visible in the US images acquired by both the Epolight-PDMS and rGO-PDMS transmitters (Fig. 3.17a),b)). The SNR was highest for the tungsten wires closest to the probe (Epolight 15D: 40 dB, rGO: 38 dB). The contrast

of the PSF decreased with depth by *ca.* 2 dB/mm (Fig. 3.17c)).

It was found that decreasing the A-line acquisition step-size improved the resolution. In particular, the lateral resolution given by the Epolight-PDMS transmitter improved from 200 µm to 60 µm at a depth of 4 mm as the spacing was reduced from 200 µm to 50 µm (Fig. 3.17e)). This relationship was also observed in the lateral resolution given by the rGO-PDMS transmitter at decreasing acquisition step-size.

For all images, the lateral resolution deteriorated with depth (Fig. 3.17e),g)). The best resolution was found at 4 mm (Epolight-PDMS: 60 µm, rGO-PDMS: 75 µm), while the larger depths of 25 mm showed poorer resolutions (Epolight-PDMS: 120 µm, rGO-PDMS: 110 µm) at a maintained A-line spacing of 25 µm.

The axial resolution remained relatively constant at all depths and A-line step-sizes (50 ± 8 µm) (Fig. 3.17d),f)).

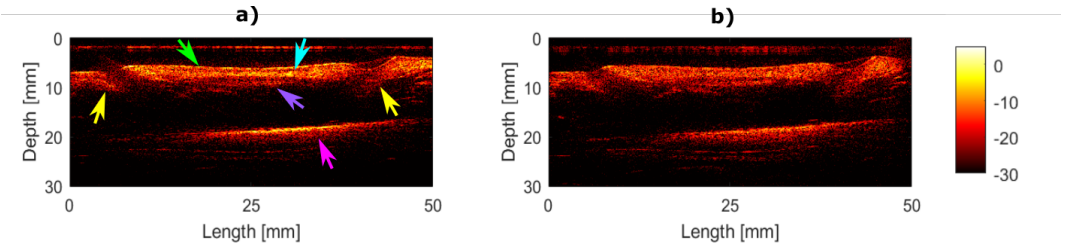

Figure 3.18: B-mode optical ultrasound images of *ex vivo* swine aorta tissue acquired using a) Epolight-PDMS transmitters and b) rGO-PDMS transmitters. Right: dB scale bar. Part a) labels showing: inner edge of tissue (pink), outer edge of tissue (yellow), oesophageal mucosa (green), submucosa with oesophageal glands (blue) and muscularis propria (purple).

3.5.2.3 Swine Aorta

The aorta tissue surface was visible in the OpUS images throughout acquisition. For *ex vivo* images, the vessel was well-resolved and the cork mount behind the vessel could be visualised. For both the Epolight-PDMS (Fig. 3.18a)) and rGO-PDMS (Fig. 3.18b)) composites, three layers were visible in the vessel wall in the reconstructed OpUS images. These were thought to correspond to the intima (represented by a bright region indicated by a green arrow), the media (indicated by a blue arrow) and adventitia (indicated by a purple arrow). Further visible features included the side branches (yellow arrows) and cork mount (pink arrow). The Epolight-PDMS

transmitter generated a peak SNR *ca.* 35 dB. The rGO-PDMS transmitter, in comparison, demonstrated a peak SNR *ca.* 25 dB.

3.5.3 Discussion

The peak-to-peak pressure and bandwidth of the two composites studied here are relatively similar: pressures in excess of 1.3 MPa and corresponding -6 dB bandwidths *ca.* 35 MHz. The small difference in the generated US pressure is likely due to the difference in the optical spectra; Epolight absorbed 95% at the incident wavelength whereas rGO absorbed 89%.

3.5.3.1 Resolution

As with conventional US imaging, axial resolution is typically limited by the bandwidth of the both the generated US and the US receiver [63]. Optical US generation can achieve wide transmission bandwidths with the use of short laser excitation pulses [187]. Since the brevity of the excitation pulse is not altered through the change in acquisition step-size, it would be expected that the axial resolution remains constant with change step-size. However, whilst a shorter pulse length improves axial resolution, it typically reduces penetration depth due to the higher attenuation of high-frequency US. This may explain the slight upward trend in axial resolution observed with the rGO-PDMS transmitters (Fig. 3.17f) from > 20 mm). In contrast, this effect was not observed with the Epolight-PDMS transmitter (Fig. 3.17d)), likely due to its larger peak-to-peak pressure output, which results in stronger signals at greater depths. This improved SNR enhances the system's ability to resolve details along the axial dimension. A similar upward trend in axial resolution would likely occur for the Epolight-PDMS transmitter at a larger depth.

Lateral resolution is dictated by the width of the US beam and the bandwidth of the US [63], as well as the width of the synthetic aperture and element spacing. The narrow aperture size of the US generating elements will lead to a divergent beam which is optimal when image reconstruction is used and was consistent between the two comparative transmitters, thus any variation in lateral resolution

should be proportional to the variation in the bandwidth of the generated US. The lateral resolution values are comparable to a typical commercial US device which can achieve lateral resolutions of 100 μm depending on the bandwidth and frequency of the device [63]. The quality of the lateral resolution was indicated to be inversely proportional to the acquisition step-size. This compromise between resolution and step-size is necessary to quantify prior to further pre-clinical studies to minimise the computationally intensive reconstruction while allowing detailed images of large areas. Fig. 3.17e) and g) show a similar lateral resolution over depth at 25 and 50 μm step-sizes, thereby maintaining comparable resolution while halving the collected data set.

3.5.3.2 Tissue

Ex vivo swine aorta tissue was imaged, showing peak SNR of 35 dB and clear distinction of tissue layers. These images exhibited a higher SNR than those obtained with the rGO-PDMS transmitter, but were comparable in terms of the tissue layer distinction and side branch identification. Accurate identification of tissue layers would necessitate a histological study which was not performed. As such, the tissue layers were identified from previous similar studies such as [177]. Detailed comparisons to histological analyses would be valuable to ascertain the detail quality in the reconstructed images and therefore the future application of Epolight-PDMS transmitters to medical imaging. In particular, concurrent histological studies and OpUS images of tissues encountered in other clinical contexts that have previously been studied with fluorescence or PA imaging, such as lung [188] or gastrointestinal tissue [189], will be valuable in the assessment of the OpUS component of multimodal imaging using Epolight-PDMS transmitters.

3.6 Chapter Conclusions

This chapter demonstrates the fabrication of a composite comprising of an Epolight dye and PDMS host and compares it to a CV-PDMS composite, as well as CV-AuNP-PDMS and rGO-PDMS composites. It was found that by reducing the concentration of the Epolight dye, the optical absorption in the visible range and for

wavelengths $>$ 1200 nm could be reduced whilst maintaining a relatively high optical absorption at 1064 nm for US generation. However, while the presence of these optical absorption windows are promising for multi-modal imaging, the transmission fraction, particularly in the visible range, is not sufficient for fluorescence excitation for any manufacturing method or concentration. However, the transmission window in the mid-infrared range is promising for the generation of fluorescence imaging using Indium-based contrast agents [4].

The US generated by the composites was comparable to that used in previous studies for imaging [139, 179, 109]. All the Epolight composites fabricated outperformed all three reference CV composites fabricated here, exhibiting maximum peak-to-peak pressures of *ca.* 1.3 MPa and bandwidths of *ca.* 30 MHz for the 15D composite. This is sufficient for both the high resolution imaging and the high penetration depth as given in the requirements (Section 1.2). It should also be noted that previous studies with CV composites have achieved higher pressures and bandwidths [3]. As expected, the optical absorption and peak-to-peak pressure decreases with the concentration of the Epolight dye. The bandwidths remained relatively constant, apart from a significant decrease shown by the 2.5A, which could have been caused by the longer absorption length, leading to a wider temporal profile in the generated US pulse. Additionally, the DD composites showed wider bandwidths than any AiO composites, which is likely due to the direct heating of the optical absorber and a thinner PDMS overcoat created by the bilayer application.

Crucially, the photostability of the Epolight composites was measured and compared to the CV composites, which have previously been used for *ex vivo* imaging, but demonstrated poor photostability [3]. All of the Epolight composites had acceptable photostability, with the pressure only dropping by *ca.* 10% over a period of 1 hour, which is well within the expected experimental error, compared to a 68% drop for CV composites over the same period. These timescales are relevant for translation of the devices to minimally invasive imaging contexts, where procedures typically take $>$ 1 hour. The results here demonstrate that composite coatings comprising Epolight 9837 are promising for application in multi-modal all-optical

US devices. Future work could consider other dyes with different wavelength selectivities allowing for application-specific composites. This includes further work on the CV composites used here for reference, including the impact of diffusion time for the gold salt.

After both optical and acoustic characterisation, a 15D transmitter was used in conjunction with a plano-concave microresonator for US imaging and compared to previously-presented rGO-PDMS transmitters. A bench-top OpUS imaging setup was used to acquire 2D images with resolutions as low as 75 μm laterally and 50 μm axially. Tissue images were well-resolved with structures clearly visualised. The comparable imaging parameters demonstrated by this system with both the previously presented transmitter and conventional piezoelectric US is indicative of the potential of this composite material in an OpUS application.

Chapter 4

All-Optical Lateral Ultrasound Probe for Rapid Image Acquisition

This chapter is based on work published in [36], and describes the development of a novel US imaging methodology in tandem with a bespoke miniaturised US probe.

4.1 Introduction

OpUS generation is highly suited to guiding minimally invasive procedures [3, 139]. However, for applications such as GI tract imaging or lung tissue imaging, these devices need to be modified to allow a view of the vessel wall, perpendicular to the fibre axis. Previous research has shown proof of concept for a lateral probe [138] but further development is required to optimise the imaging process and move the system from benchtop to pre-clinical studies. Additionally, there is a need for a rapid acquisition method: current OpUS acquisition methods use a step-by-step raster acquisition process which is time-intensive [35].

The work in this chapter details an investigation into the development of an OpUS transmitter with a lateral field-of-view. This was evaluated in comparison with the forward-viewing transmitters detailed in Chapter 3, and studied in terms of its suitability for minimally invasive imaging. The transmitter was combined with an omnidirectional optical receiver and packaged within an US transparent sheath with compatible dimensions for the working channel of a standard-of-care clinical endoscope.

Additionally, a rapid acquisition method was developed to acquire 2D B-mode images with subsecond acquisition times. This was applied to resolution phantoms and *ex vivo* tissue to assess the imaging capabilities.

4.2 Study I: Lateral Probe Development

Typically, a foward-viewing fibre like that used in Chapter 3 is cleaved perpendicular to the longitudinal axis, after which the flat distal surface of the fibre is coated in a composite coating. The resulting US emission will therefore propagate along the same axis on which the fibre is placed. In order to create a side-viewing fibre, the transmitter had to be modified to transmit signal laterally.

However, this requirement creates a range of difficulties in the manufacturing process. Firstly, the optical fibres are brittle and fragile, so are difficult to adapt. Secondly, lateral emission requires a smooth surface for reflection of the laser pulse to the outer edge of the fibre. Finally, the curved outer edge of the fibre is not conducive to either coating the emission surface or narrowing the focus area of the beam. As such, the fibre was tipped with a square capillary in order to protect the fibre tip, allow for a larger reflection surface for the laser pulse, and create a flat emission surface on the lateral face. This capillary has several uses: firstly, the 45°angle of an already minuscule fibre is highly fragile, so the capillary adds structural protection. Secondly, by aligning one of the flat faces of the capillary with the reflected light emission, the directivity of the resulting US beam can be more easily determined and controlled. The resulting beam divergence is based on the geometry of the transmitting surface; a convex surface creates a larger beam divergence, while a planar or concave surface creates a more focused beam [89]. Additionally, the temporal profile of the wave is proportional to the pulse intensity for a planar source, but proportional to only half the intensity for a cylindrical source [89].

4.2.1 Transmitter Fabrication

The fibres used here were SMA connectorised silica core/silica cladding optical fibres with a 400 μm diameter and a polyimide buffer coating (FG400LEP, Thorlabs,

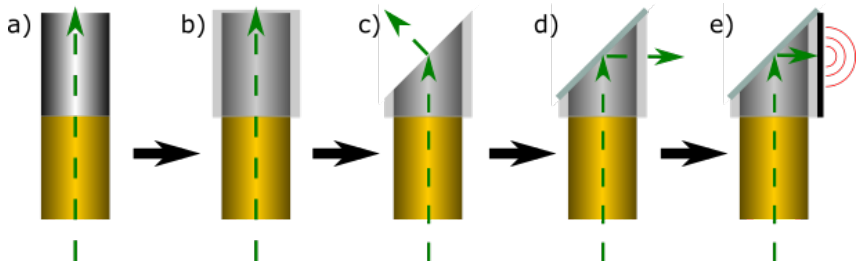

Figure 4.1: OpUS transmitter fabrication process; a) stripped and cleaved optical fibre, b) optical fibre inserted in square glass capillary, c) optical fibre and capillary polished to a 45 °angle, d) silver mirror applied to polished surface, e) OpUS-generating composite coating applied to capillary surface.

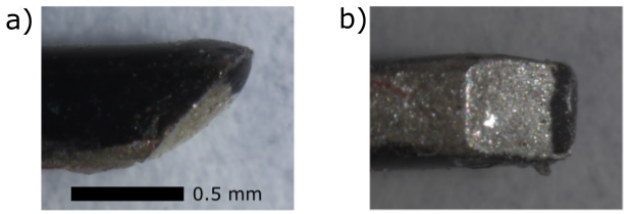

Figure 4.2: Stereo-microscope images of a) side-view and b) bottom view of rGO-PDMS lateral transmitter. Scale bar: 0.5 mm.

UK). The fabrication of the transmitter at the distal end of the fibre in shown in Fig. 4.1.

Briefly, the polyimide layer was carbonised and stripped from the fibre, followed by perpendicular cleaving as normal (Fig. 4.1a)). Next, the stripped fibre was tipped with a square capillary (OD: 0.5 x 0.5 mm, wall thickness: 0.1 mm, Vitrocom Hollow Square 8250 – 100, CM Scientific, Germany) such that the cleaved face of the fibre was aligned with the end of the capillary (Fig. 4.1b)). The square glass capillaries were cut to size (*ca.* 1 cm length) and fastened in place using clear LED-cured epoxy (Norland Optical Adhesive 1665, Edmund Optics, USA).

After this, the flat distal face was polished to a 45°angle (Trig Bare Fibre Polisher, Krell Technologies, USA). The fibre was clamped at a 45° angle to the polishing surface, and, using a 9 µm lapping paper, the bulk of the material was removed to create a 45° surface (Fig. 4.1c)). Subsequently, this surface was polished using both 3 µm and 0.3 µm lapping sheets, and the surface inspected with the 80x magnification tool built into the polisher. The fibre tips were then gently cleaned with lint free paper and isopropyl to remove any remaining material.

The next step was to apply silver mirror paint (RS PRO Conductive Lacquer, RS PRO, UK) to the 45°surface (Fig. 4.1d), Fig. 4.2). The purpose of the coating on the 45° face is to reflect the pulsed light towards the longitudinal surface of the fibre.

Finally, the US-generating composite was applied to the capillary surface (Fig. 4.1e)). Here, two composites were used for direct comparison: Epolight-PDMS 15D and rGO-PDMS, both described previously (see Section 3.2.1.1). The fabrication of the composites is described briefly as follows:

- **Epolight-PDMS**. 15 mg of Epolight 9837 (Epolin, USA) was sonicated for 20 s in 0.5 ml of xylene. This was deposited on the capillary surface to form a bilayer composite. Subsequently, an overcoat of PDMS (MED-1000, Polymer Systems Technology, UK) thinned with xylene (ratio of 0.25 g to 0.5 ml) was applied to the Epolight coating to create a bilayer composite.

- **rGO-PDMS**. 500 mg of rGO functionalised with octadecylamine (805084, Sigma Aldrich, UK) was sonicated for 20 s in 2.5 ml of xylene. This was deposited on the capillary surface opposite the silver mirror and left to dry for *ca.* 12 hours. Subsequently, an overcoat of PDMS thinned with xylene was applied to the rGO coating to create a bilayer composite.

4.2.1.1 Transmitter Characterisation

Here, both Epolight-PDMS and rGO-PDMS composites were characterised in the lateral configuration, alongside their forward-viewing counterparts for direct comparison.

Methods

The US pressure time-series and bandwidth were measured at a single point using the methodology outlined in Section 3.2.2.2 using a pulse energy of 20 μJ. Briefly, the study fibre was mounted on a stationary clamp stand directly opposite a 200 μm needle hydrophone, which was centred on the US beam and set to a transmitter-receiver distance of 1.5 mm. For the laterally-configured fibres, the study fibre was rotated to face the emission surface of the capillary towards to hy-

	Epolight-PDMS		rGO-PDMS	
	Pressure [MPa]	Bandwidth [MHz]	Pressure [MPa]	Bandwidth [MHz]
Forward	1.70	34.9	1.31	32.3
Lateral	1.02	26.5	0.72	18.5

Table 4.1: Comparative ultrasound peak-to-peak pressure and corresponding −6dB bandwidth for rGO-PDMS and Epolight-PDMS coatings in both lateral- and forward-viewing configurations.

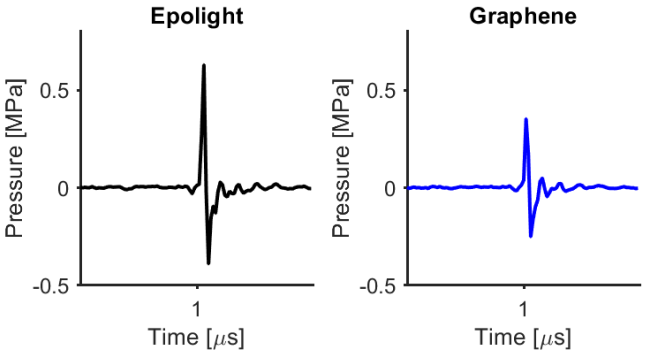

Figure 4.3: Ultrasound time-series measured at 1.5 mm from the emitting face for composite coatings of Epolight-PDMS (black) and rGO-PDMS (blue).

drophone. The received US pressure was measured, and the bandwidth obtained by applying a Fourier transform and the hydrophone calibration to the acquired time-series.

Results

The resulting time-series and power spectra are shown in Fig. 4.3 and Fig.

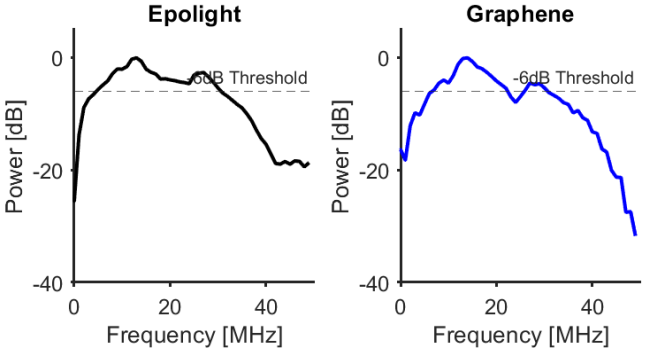

Figure 4.4: Ultrasound power spectra measured at 1.5 mm from the emitting face for composite coatings of Epolight-PDMS (black) and rGO-PDMS (blue).

4.4. The time-series shown in Fig. 4.3 are both bipolar in shape. The peak-to-peak pressures were 1.02 and 0.72 MPa for the Epolight-PDMS and rGO-PDMS composites respectively.

The corresponding power spectra were 26.5 and 18.5 MHz for the Epolight-PDMS and rGO-PDMS composites respectively. The pressure and bandwidth were smaller for both composites in the lateral configuration than in their forward viewing-counterparts (Table 4.1).

Discussion

The US generated by the modified lateral-viewing transmitters was comparable to that of the forward-viewing transmitters (Table 4.1). Indeed, both lateral transmitters produced pressures and bandwidths that exceeded those of a lateral transmitter demonstrated previously [138]. The Epolight power began to fall around 30 MHz which is well within the calibration range of the hydrophone, suggesting that the detector is not limiting the measured bandwidth. However, the pressures and bandwidths were slightly lower for the lateral transmitters. This difference is likely due to the dip-coating process; here, the bilayer composite was applied by dipping only the emitting face of the transmitter into the solution, as opposed to immersing the entire fibre tip as done for the forward-viewing transmitters (Fig 3.2). This could have inadvertently influenced factors such as the concentration of the solution the emission surface is exposed to and the withdrawal speed; these have been determined to be key factors in the quality of the deposited layers [173, 174].

Alternatively, the lower pressures and bandwidths could be due to loss of fluence intensity through inefficient reflection by the mirror-coated surface. The silver mirror paint used here reported reflection of $\leq 95\%$ of light for wavelengths ≥ 400 nm [190]. This assumes a uniform polished surface, which, while great care was taken with polishing the 45° surface, was not guaranteed. As such, while the US generated here was sufficient for US imaging, further development of a more efficient transmitter is necessary.

4.2.1.2 Beam Divergence

As stated in Section 2.2.3, a wider beam divergence will reduce the focus of the emission thereby creating pressure loss through beam spreading and subsequently reducing the available penetration depth [84]. Forward-viewing fibres optical fibres of the same diameter have previously been reviewed [191], but the design of a side-viewing probe will likely change the shape and focus of the emitted US. In order to evaluate the FWHM area and the change in pressure over depth, a beam divergence study was carried out.

Methods

Here, both Epolight-PDMS and rGO-PDMS transmitters in forward and lateral configuration were assessed. First, the hydrophone was moved to a fixed distance from the emitting face of the transmitter (1.5 mm) and centred on the maximum US pressure, as with acoustic characterisation. Vertical and horizontal raster scans consisting of 61 measurements were then acquired intersecting this point using the motorised stages at an acquisition step size of 50 µm. This equated to a 9.3 mm^2 grid. The peak pressure p was extrapolated backwards for each position, resulting in an array of cross-sections of the US beam. The size of the FWHM cross section was extrapolated backwards to give the area of the beam over distance.

Results

	Distance [mm]		0	5	10	15
FWHM [mm^2]	Epolight	F	0.4	3.0	7.7	9.3
		L	0.4	3.3	7.5	9.3
	rGO	F	0.4	3.1	6.9	9.3
		L	0.4	3.2	7.5	9.3
Pressure [MPa]	Epolight	F	1.5	0.6	0.3	0.3
		L	1.2	0.6	0.5	0.5
	rGO	F	1.2	0.4	0.3	0.2
		L	1.0	0.5	0.4	0.4

Table 4.2: Beam divergence of Epolight-PDMS and rGO-PDMS composites in both the forward- (F) and lateral-viewing (L) configurations.

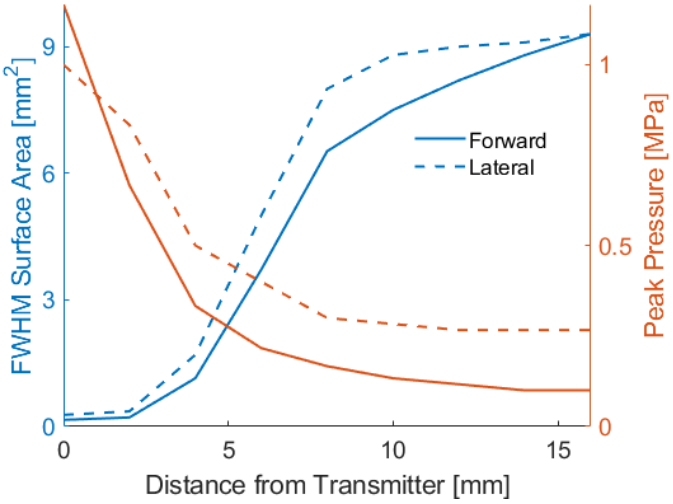

Figure 4.5: Peak ultrasound pressures (orange) and FWHM areas (blue) at distances from the US emission surface for a rGO-PDMS composite coating in both the forward- (solid line) and lateral-viewing (dashed line) configurations.

The beam divergence of the rGO-PDMS lateral transmitter was shown to spread at approximately the same rate as the forward-viewing counterpart (Fig. 4.5). Both transmitters reached a maximum FWHM of *ca.* 9.3 mm^2. The initial spot area for all transmitters was 0.4 mm^2 which corresponds to the size of the emission surface.

However, the pressure loss appears to be greater in the forward-viewing fibre, with a difference of 0.2 MPa shown at 15 mm in comparison with the lateral-viewing transmitter. This was also demonstrated in the Epolight-PDMS coating, with a pressure 0.5 MPa and 0.3 MPa measured at 15 mm for the lateral- and forward-viewing transmitters respectively (Table 4.2).

Discussion

The initial beam spreading is equal to the size of the emission surface for the forward viewing fibre. Technically, the area coated in the US-generating composite for the lateral-viewing transmitter is *ca.* 2.5 mm^2. However, the spot area of the incident laser light theoretically corresponds to the size and shape of the optical fibre within the capillary. This is confirmed by the area of the beam given at 0 mm for both lateral transmitters.

Colchester et al. [175] demonstrated a highly directional forward-viewing US

transmitter; the beam width at 16 mm was found to be 2.1 mm diameter, equating to an area of 3.46 mm^2. However, the fibre used had a diameter of 640 µm; as outlined in Section 2.2.3, a larger aperture size equates to more directional US generation. Colchester et al. [175] also presented a simulation model to show theoretical beam divergence for a range of fibre diameters. This calculated a FWHM area of *ca.* 11 mm^2 at 16 mm for a 400 µm diameter optical fibre. Here, both forward- and lateral-viewing transmitters demonstrated a maximum FWHM of 9.3 mm^2. This equates to the acquired grid size, implying that the FWHM could extend beyond this size. However, the general trend here agrees with the simulated results.

The comparable beam divergence with the forward-viewing transmitter demonstrated in Chapter 3 implies that the lateral-viewing transmitter is suitable for invasive imaging. While a highly directional probe would be necessary for extreme imaging penetration depths, continuous acquisition depends on whole-field insonification, making a larger beam divergence more desirable. However, this must not be at the expense of available penetration depth. The imaging studies in Chapter 3 demonstrate that the forward-viewing probe achieves good resolution and SNR at imaging depths of ≤ 30 mm. As such, it can be concluded that the beam divergence and pressure loss here is sufficient for high-resolution US imaging in the intended context.

4.2.2 Probe Fabrication

In order to fabricate a miniaturised probe for pulse-echo imaging, the transmitters require integration into a singular transmit-receive imaging system. The two main components of an OpUS imaging system are the transmitter and the receiver.

4.2.2.1 EBUS Catheter

As described in Section 1.2, an important element of the probe design is ease of medical translation, including hardware integration for current systems. To this end, the transmitter and receiver were built into Endobronchial Ultrasound (EBUS) sheaths (K201 EBUS Sheath, Olympus, US), which are specifically developed to be used in the working channel of an endoscope, meaning that the diameter is suitable

for medical use and the sheaths themselves are considered medically safe.

The EBUS sheaths acquired consisted of 3 parts:

- An ultrasonically transparent guide sheath.
- Forceps.
- A protective torque coil placed over the forceps.

While the forceps were not used in the optical probe, the other two parts were considerably useful. The cable for the forceps was cut and the forceps removed, meaning that the torque coil (which fits perfectly inside the guide sheath) was able to be used as protection for the optical fibres.

4.2.2.2 Integration of Probe into EBUS Catheter

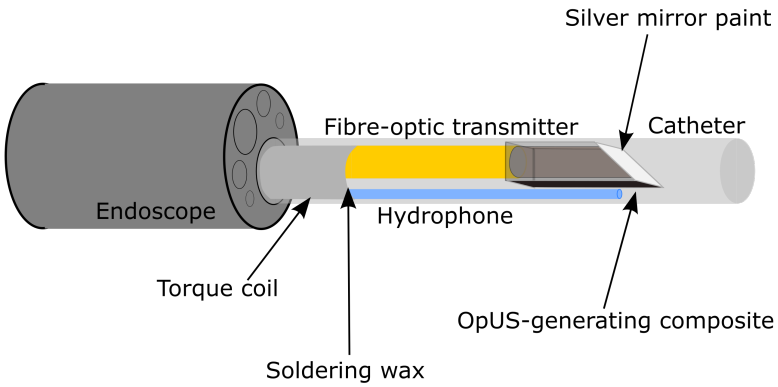

Figure 4.6: Schematic of lateral probe encased in an ultrasonically-transparent sheath inside the working channel of a mock endoscope.

Here, the receiver used was the planoconcave microresonators developed by Dr. Zhang (Dept. of Medical Physics, UCL). These receivers have been described previously [136]. Briefly, a plano-concave microresonator was fabricated on the tip of a single-mode optical fibre (SMF-28, Thorlabs, UK) by depositing a dieletric mirror on the distal face of the fibre prior to dip-coating the distal end into an optically transparent polymer, and finally applying a second mirror on the outer surface of the polymer. These are well suited for lateral use as they have highly omni-directional

sensitivity, meaning no modification is required for integration into a lateral device [136].

Firstly, the transmitter was cleaved at the proximal end and backthreaded through the protective torque coil (diameter: 600 µm) until *ca.* 1 cm of the distal end is visible. The transmitter then required SMA connectorising once in place. This 'fixes' the transmitter within the torque coil, as the capillary prevents the transmitter from sliding through one end, while the SMA connector holds the other end. The diameter of the torque coil was too narrow for the capillary to fit through.

Secondly, the hydrophone was then gently forward-threaded through the torque coil alongside the transmitter fibre until *ca.* 1 cm was visible at the distal end. The hydrophone and transmitter are aligned such that the tip of the hydrophone was adjacent to the emitting face of the capillary (Fig. 4.6).

Subsequently, the two elements were fixed in place at both the distal and proximal end of the torque coil by using a soldering iron to apply sealing wax, taking care to ensure that no heat was applied directly to either fibre (Fig. 4.6). The proxi-

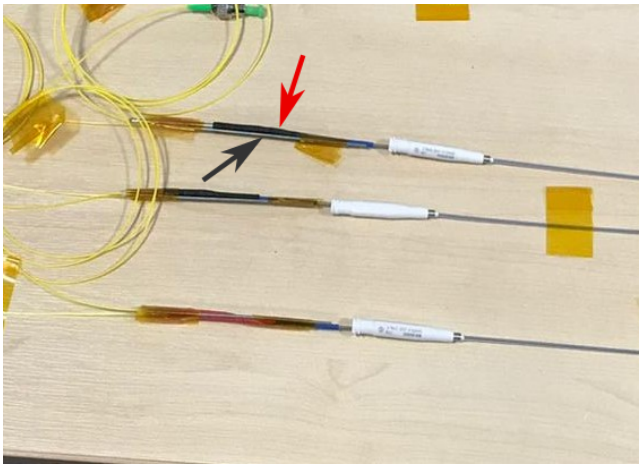

Figure 4.7: Structural support at the distal end of the probe consisting of two layers of heat shrink (red arrow) and strapped torque coil (black arrow).

mal end of the torque coil was then the most fragile element of the probe, especially with the weight of the connector element of the hydrophone. This was reinforced using two layers of heat shrink, and further strengthened by an additional piece of torque coil strapped across the connector element (Fig. 4.7).

A Luer side arm adaptor was slid over the torque coil to meet the structural

support element and secured in place using the strainer clamp. Finally, the US-transparent EBUS sheath was threaded over the probe and the white plastic tubing at the end of the sheath (Fig. 4.7) was clamped into the Luer side arm.

Mock Endoscope

A mock endoscope was fabricated out of steel hypotubing using the same diameters as standard clinical GI endoscopes: a 5 mm outer diameter with a 2 mm working channel [192]. The OpUS catheter was inserted through the working channel of the mock endoscope for imaging (Fig. 4.8). This was important to evaluate the handling, robustness and mechanical flexibility of the probe by replicating a clinical setting as closely as possible.

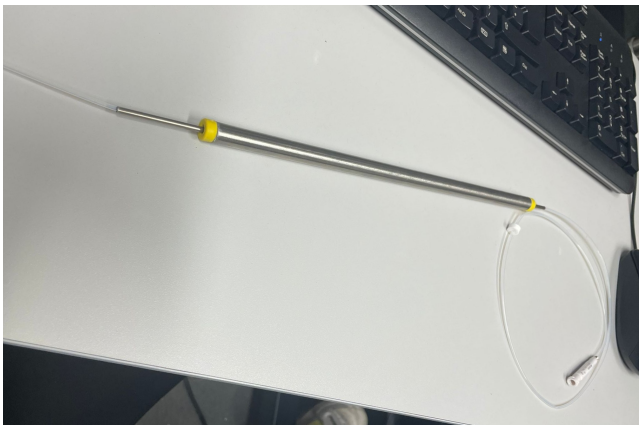

Figure 4.8: Mock endoscope fabricated for use in conjunction with OpUS probe.

4.3 Study II: Comparison of Raster and Continuous Acquisition Imaging

The imaging methodology in Chapter 3 involved a step-by-step raster acquisition of images. In this process, the motor moves the probe a set distance, pauses to acquire an A-line, and then repeats. The concatenation of these A-lines creates the final 2D image. However, this method is highly time-intensive, with each scan taking up to an hour depending on the image size. One potential improvement would be the use of a faster motor with raster scanning capabilities to accelerate the process. However, the step-by-step acquisition approach remains inherently slower than a continuous acquisition method due to the repeated stopping and starting of

the motor at each scanning point. A continuous acquisition approach, such as using a high-speed translation stage, could significantly reduce scan times by eliminating mechanical delays and enabling real-time data collection. Additionally, optimising the synchronisation between the laser, transducer, and motion system could further enhance efficiency while maintaining imaging precision.

In order to meet the acquisition times discussed in Section 1.2, a significant reduction in scan time is necessary. This section introduces a novel imaging methodology developed to achieve this goal. Here, A-lines are acquired at set intervals under continuous motion. This was initially assessed using speeds ≤ 5 mm/s, and compared with images on a tungsten wire phantom and *ex vivo* swine aorta acquired by a forward-viewing probe using both the typical raster scan and continuous acquisition. This study was carried out using the 15D Epolight-PDMS composite coating.

4.3.1 Methods

4.3.1.1 Data Acquisition

Forward-viewing Probe

The configuration of the forward-viewing probe was outlined in Section 3.5. Briefly, the transmitters were combined with a plano-concave microresonator to create a fibre-optic OpUS probe with a 'top-down' view of the imaging target (Fig. 3.6). This probe was clamped to a motorised stage (MTS50/M-Z8, Thorlabs, UK) controlled by a motor controller (TDC001 T-Cube DC, Thorlabs, UK). Imaging was performed by translating the probe horizontally with respect to the target. Images were acquired using both a raster scanning approach and a continuous motion approach with speeds of $1-5$ mm/s. A-lines were acquired at a spacing of 25 µm. The acquisition rate was varied to maintain the the A-line spacing depending on the translation velocity; for example, at a velocity of 5 mm/s, a repetition rate of 200 Hz was used. Each A-line consisted of 4000 sensor data points corresponding to a total imaging depth of 30 mm.

Lateral-viewing Probe

The proximal end of the probe outlined in Section 4.2 was clamped to a

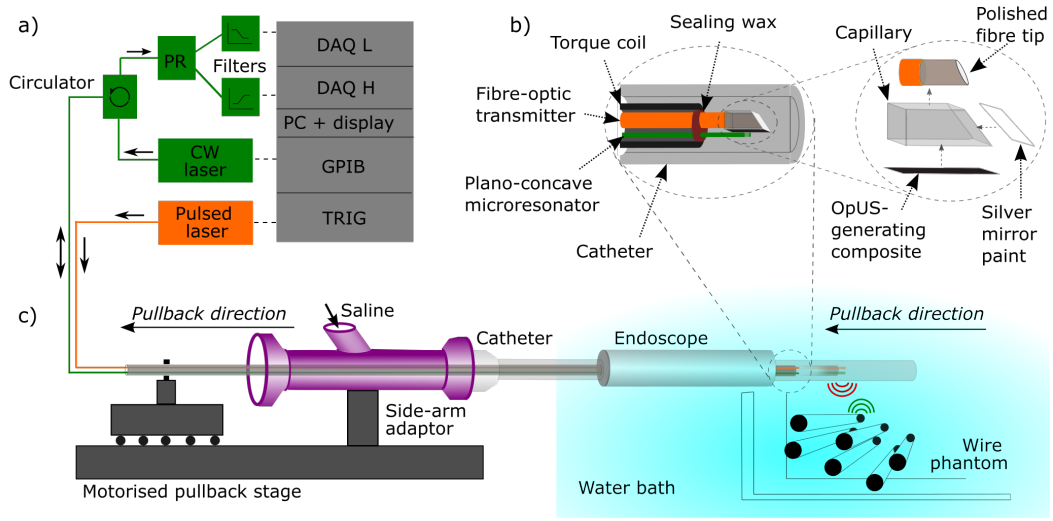

Figure 4.9: System for all-optical lateral ultrasound imaging through fast pullback. a) Imaging console comprising pulsed excitation light delivered to the transmission fibre and CW light delivered from a wavelength-tuneable laser to the receiving fibre. b) Cutaway schematic of the fabricated side-viewing OpUS probe comprising the plano-concave microresonator and side-viewing optical ultrasound transmitter. c) Schematic of the side-viewing optical ultrasound transducer. Ultrasound transmitting fibre (orange) and omnidirectional receiver (green) inside the probe, including OpUS probe submerged in the saline water bath and directed at the wire phantom imaging target.

motorised stage (MTS50/M-Z8, Thorlabs, UK) controlled by a motor controller (TDC001 T-Cube DC, Thorlabs, UK) to provide motion (Fig. 4.9c)). The probe was clamped such that the side arm adaptor and US transparent sheath were held stationary while the torque coil with the optical fibres fixed inside was mounted on the translation stage. This enabled the probe to be pulled back within the sheath, whilst the outer sheath remained stationary. The sheath, along with the contained US probe, was inserted into the mock endoscope and submerged in a water bath for imaging, while saline was injected through the side-arm to provide US coupling. To acquire US images, the probe was translated laterally in both a raster scanning method and at a constant velocity within the sheath with respect to the imaging target. A-lines were acquired at a spacing of 25 µm. The acquisition rate was varied to maintain the the A-line spacing depending on the translation velocity. Each A-line consisted of 4000 sensor data points corresponding to a total imaging depth of 30 mm. The impact of larger A-line spacing was investigated by removing A-lines

in post-processing.

4.3.1.2 Imaging Console

The imaging console was outlined in Section 3.2.3.2. Briefly, the transmitters were coupled to the pulsed Nd:YAG laser for US generation (1064 nm, Elforlight, UK). The plano-concave microresonator was interrogated with a continuous wave laser (Tunics T100S-HP, Yenista Optics, France) with a tuning range of $1500-1630$ nm and a power of 4.5 mW as described in previous studies [140, 175]. The laser was connected via a fibre optic circulator which allowed the reflected signal to be detected with a photoreceiver, which was used to record the modulation of the reflection induced by the incident acoustic wave (Fig. 4.9a)).

4.3.1.3 Image Processing

The image processing was outlined in Section 3.2.3.4. Briefly, the acquired A-lines were concatenated, followed by the application of a bandpass filter (Butterworth, 4^{th} order, $1.5-40$ MHz). Subsequently, a cross-talk algorithm was applied to remove the US signals transmitter directly from the transmitter to the receiver, as described previously [177]. Subsequently, the image was reconstructed using a k-space method based on the fast-Fourier transform from the k-Wave toolbox [77]. Finally, the signal envelope was found using the absolute value of the Hilbert transform, followed by a log transformation. PSF's at two depths were chosen: one at 3.5 mm and one at 7 mm. The SNR was measured for these PSF's, along with the axial and lateral resolutions, for both raster scanning and imaging speeds of $1-5$ mm/s at a set A-line acquisition spacing of 25 µm. Each scan was repeated 10 times to assess the deviation in image quality.

4.3.1.4 Imaging Targets

The imaging targets used here were described in Section 3.2.3.5. Briefly, imaging was carried out using both a resolution phantom consisting of tungsten wires (OD: 27 µm) and *ex vivo* swine aorta. These were both submerged in a water bath for imaging.

4.3.2 Results

4.3.2.1 Resolution Phantom

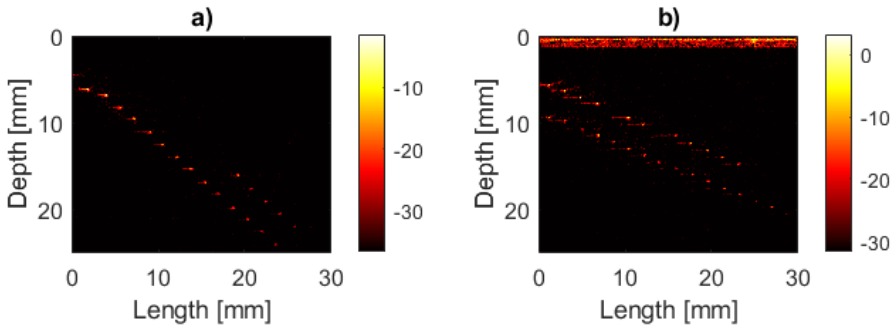

Figure 4.10: Reconstructed OpUS images (A-line spacing of 25 µm) of the tungsten wire resolution phantom acquired using lateral-viewing probe and a) raster acquisition and b) 5 mm/s continuous acquisition.

The tungsten wire phantom appeared in the reconstructed images as a series of PSF's which were used to measure the resolution of the imaging system (Fig. 4.10). The FWHM of the PSFs in the OpUS images were used to provide values for the axial and lateral resolutions. Here, all PSF's were visible in the images acquired (Fig. 4.10).

The SNR and lateral resolution were slightly improved in the images obtained using a forward-viewing configuration, regardless of the acquisition method. As discussed in Section 3.5, both the SNR and lateral resolution worsened with depth, while the axial resolution remained constant at *ca.* 50 µm (Table 4.3). The SNR for the lower PSF was consistently poorer than that for the higher PSF, reaching a maximum of 38 dB in the forward-viewing configuration and 27 dB for the lateral-viewing configuration. This trend was also observed in the lateral resolution, which was consistently better for the higher wire than for the lower wire. Nevertheless, all parameters remained stable in the change of acquisition methodology, and the values were comparable across different transmitter configurations (Table 4.3).

			Raster	1	3	5
Forward	SNR [dB]	Top	38 ± 2	35 ± 2	32 ± 2	38 ± 1
		Bottom	25 ± 3	21 ± 2	26 ± 3	26 ± 2
	Ax. [µm]	Top	50 ± 3	55 ± 4	50 ± 3	51 ± 3
		Bottom	48 ± 3	51 ± 3	55 ± 2	50 ± 3
	Lat. [µm]	Top	82 ± 17	90 ± 15	89 ± 13	93 ± 16
		Bottom	120 ± 16	110 ± 21	129 ± 13	125 ± 13
Lateral	SNR [dB]	Top	25 ± 3	26 ± 3	22 ± 3	27 ± 2
		Bottom	18 ± 2	20 ± 2	21 ± 3	19 ± 2
	Ax. [µm]	Top	55 ± 3	60 ± 4	57 ± 3	60 ± 3
		Bottom	53 ± 3	51 ± 3	60 ± 4	55 ± 3
	Lat. [µm]	Top	120 ± 22	115 ± 21	130 ± 11	127 ± 16
		Bottom	210 ± 27	189 ± 21	204 ± 26	215 ± 24

Table 4.3: Image quality metrics for PSF target depths imaged with forward- and lateral-viewing image configurations and both raster and continuous imaging (1 – 5 mm/s). Values presented as mean ± standard deviation, calculated from resolution assessment of five repeated images.

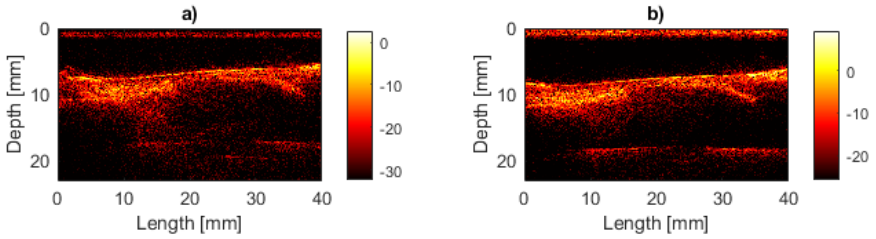

Figure 4.11: B-mode OpUS images of *ex vivo* swine aorta tissue acquired using a lateral-viewing probe and a) a raster acquisition and b) a 5 mm/s continuous acquisition.

4.3.2.2 *Ex vivo* Aorta Tissue

The aorta tissue surface was visible in the OpUS images through acquisition. For both raster and continuous acquisition, three layers were visible in the vessel wall in the reconstructed image. Both images showed a peak SNR of *ca.* 25 dB. The SNR of the tissue seemed to remain unaffected by the speed of acquisition and the configuration of the imaging probe.

4.3.3 Discussion

The axial resolutions demonstrated here, regardless of target depth, acquisition speed, or probe configuration, were consistent with previous OpUS devices such as [138] or [35] who both reported axial resolutions of 50 μm. Similarly, a good lateral resolution was achieved by all combinations here, with values as low as 110 μm. These values are comparable to previous OpUS probes [193, 177, 88], as well as typical commercial piezoelectric US devices which can achieve resolutions of 200 μm depending on the bandwidth and frequency of the device [63, 194, 195]. However, unlike the axial resolution, there is an inverse relationship demonstrated between the depth and the lateral resolution. This relationship has been demonstrated in Section 3.5, as well as previous OpUS studies [196, 177]. As outlined in Section 2.2.3, the lateral resolution could be enhanced by increasing beam divergence. However, the mechanical and US properties of such a modification must be considered. A smaller aperture could increase the beam divergence, albeit at the expense of penetration depth, but could increase the fragility of the transmitter tip, making fabrication more challenging.

It is also of note that the on-axis positional accuracy of this motor is $\pm$290 μm which could significantly degrade the quality of the reconstructed image. In particular, this error may lead to a lateral resolution loss due to inconsistently spaced A-lines, or introduce aliasing artefacts from spatial inconsistencies. To mitigate this, the stage undergoes a 'homing' procedure between scans, ensuring relative consistency in positional errors. Since the motor operates via a lead screw mechanism, positional drift can accumulate without calibration. However, once homed, the system is effectively recalibrated, achieving a movement accuracy of $\pm$4 μm.

Nonetheless, a smaller transmitter could offer other advantages. While the measured parameters appear to be independent of the acquisition speed in this context, errors and artefacts may be introduced during pullback motion. Considering Fig. 4.10, for example: increased noise in the uppermost 2 mm of the image appeared in the image acquired under continuous motion (Fig. 4.10b)) in comparison to the typical noise acquired under raster motion (Fig. 4.10a)). Noise in this re-

gion is usually removed during the application of a cross-talk removal algorithm [177]. The persistence of this noise through typical filters implies that the signal is originating elsewhere. The diameter of the capillary tip on the transmitter in this probe is similar to that of the housing sheath, suggesting that this artefact may result from unintended motion between the highly sensitive microresonator and either the transmitter or the sheath during acquisition. This noise is not present in images acquired using a raster scanning method, regardless of the probe configuration. Unlike continuous scanning, the raster method allows the receiver to remain stationary during each A-line acquisition, ensuring a more consistent distance from the transmission surface and reducing motion-induced artefacts such as interaction between the transmitter and receiver or a change in the acquired cross-talk. This artefact is likely exaggerated by the positioning of the detector relative to the emission surface; this noise is not noticeable in images acquired using continuous acquisition and a forward-viewing configuration. As such, a smaller diameter transmitter could also reduce the friction within the sheath.

The SNR demonstrates a similar set of relationships as the lateral resolution. Firstly, the impact of probe configuration appears minimal, with a difference of *ca.* 8 dB between the respective measurements for each configuration. Secondly, the speed of acquisition appears to have a negligible effect on the measured SNR. Finally, the SNR for all configurations and acquisition speeds shows a proportional relationship with the depth of the target. This could be improved by the application of Time Gain Compensation (TGC) such as that presented by [179]. The addition of TGC could additionally improve resolutions through the magnification of out-of-plane contributions to the delay-and-sum reconstruction. This could also be useful for tissue imaging: the peak SNR of the *ex vivo* swine aorta was comparable with previous studies (see Section 3.5), but the application of TGC could improve the delineation of the underside of the tissue.

This study demonstrates a proof-of-concept for a novel image acquisition process in tandem with a bespoke US transmitter. In general, it can be concluded that continuous acquisition is a comparable imaging process to the widely used raster

scanning method, while demonstrating a drastic reduction in acquisition time. Directions of development here include increasing the acquisition speed to satisfy the tool requirements (Section 1.2) and applying this to *ex vivo* oesophageal tissue.

4.4 Study III: Optimisation of Imaging Process

This study details two self-contained experiments carried out prior to rapid-acquisition lateral imaging of *ex vivo* oesophageal tissue.

4.4.1 Optimal Conditions for *ex vivo* Oesophageal Imaging

The conditions of *ex vivo* tissue for imaging is a crucial factor in determining the quality of the resulting image. One parameter to be considered is how intact the tissue remains over imaging periods. Oesophageal tissue is more susceptible to degradation *ex vivo* than tissue such as aorta [197]. Oesophageal tissue is lined with epithelial cells, such as squamous cells and ciliated columnar cells, which contain less connective tissue and fewer structural components than endothelial cells [198]. In contrast, aortic tissue is lined with endothelial cells, which has a higher density of structural proteins, enhancing their stability and slowing down the decomposition process [198]. Additionally, epithelial cells are inherently responsive to environmental factors like temperature changes and physical damage, leading to a high rate of cellular turnover. In contrast, endothelial cells have a lower turnover rate, resulting in slower decomposition [197].

Typically, tissue samples used for histopathology are placed in a fixative, like formalin, then dehydrated and embedded in a medium, such as paraffin wax [199]. While this method effectively prevents decay and preserves tissue structure, it is not conducive for US imaging of *ex vivo* tissue, where the primary aim is to replicate conditions as closely as possible to *in vivo* tissue imaging. For this purpose, hydrated tissue is needed without density alterations caused by additives such as paraffin. Therefore, a saline solution was explored for its use in imaging *ex vivo* oesophageal tissue. Whilst not a fixative, saline can temporarily preserve the tissue's physical appearance, and indeed is used for temporarily storing tissue during transport or short-term procedures [200]. However, too much salt in the solution

can affect the osmotic gradient of the tissue and cause further degradation.

4.4.1.1 Methods

Here, the effects of different saline concentrations were compared with the SNR of *ex vivo* oesophageal tissue over time. The water bath was filled with saline concentrations of 0% to 2%. For each concentration, a 4 cm long piece of *ex vivo* swine oesophagus was defrosted, cut lengthwise, and pinned to a cork mount. Images were acquired every 15 minutes for 4 hours using a 5 mm/s acquisition speed and an A-line spacing of 25 µm. The images were reconstructed (see Section 4.3.1.3) and the SNR was acquired for the upper surface of the tissue for each scan.

4.4.1.2 Results

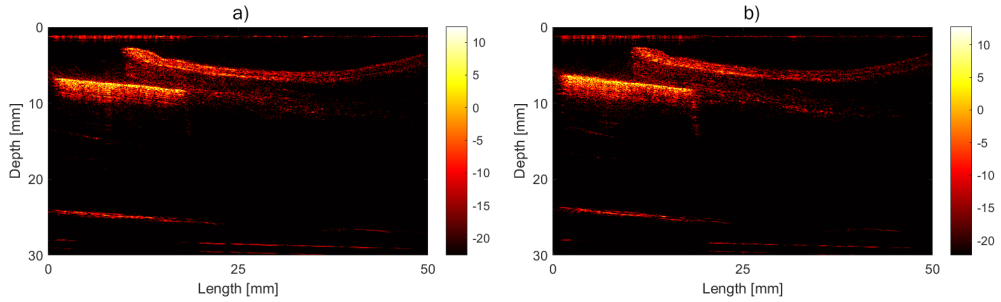

Figure 4.12: B-mode OpUS images of *ex vivo* swine oesophagus in deionised water a) immediately after submersion and b) after 30 minutes.

The full thickness of the oesophageal wall was visible in the image, with both the inner and outer surface as distinct boundaries (Fig. 4.12a)). The layer thought to correspond to the oesophageal mucosa showed the highest SNR, with a value of 28 dB. The layer beneath, thought to correspond to the muscularis propria, showed the lowest SNR of 8 dB.

The 0% concentration exhibited the greatest degradation over time, losing *ca.* 18 dB over 4 hours (Fig. 4.13). This trend was replicated in the 0.5% concentration. The concentrations of 1.5 and 2% showed a smaller loss of *ca.* 8 dB. However, the concentration of 1% showed negligible loss of SNR over the timeframe.

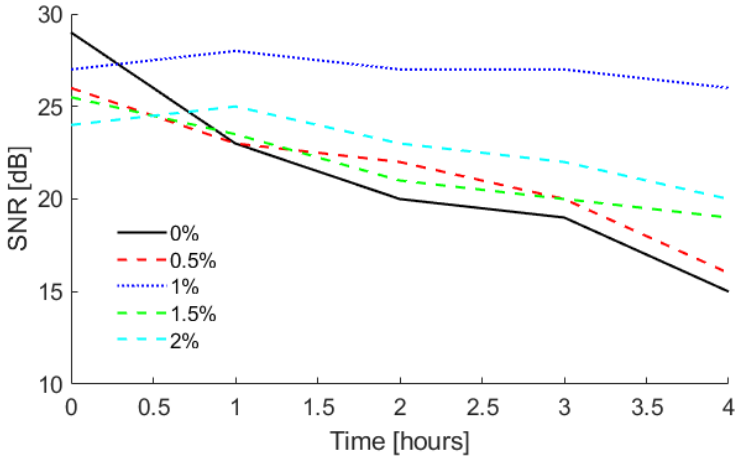

Figure 4.13: SNR of *ex vivo* oesophageal tissue acquired over 4 hours for saline concentrations of 0% (black solid line), 0.5% (red dashed line), 1% (blue dotted line), 1.5% (green dashed line) and 2% (blue dashed line).

4.4.1.3 Discussion

The results in Figure 4.13 clearly indicated that the ideal concentration was *ca.* 1%. This concentration aligns with the typical saline solution of 0.9% used for short-term tissue hydration [200, 201]. This correlation suggests that this concentration is effective in preserving the physiological balance of excised tissues by mimicking the osmotic conditions they experience *in vivo*. Excised tissue is highly susceptible to osmotic imbalances due to the loss of their natural regulatory mechanisms when removed from the body. If the surrounding solution is too hypo- or hypertonic, it can lead to cellular swelling or shrinkage, respectively, therefore compromising tissue structure [202]. The 0.9% saline solution is isotonic, meaning it has an osmolarity similar to that of extracellular fluid, which helps maintain the osmotic equilibrium of the tissue. Therefore, using a solution near this concentration helps to minimize osmotic stress, preventing the cells from undergoing lysis or dehydration. As such, it preserves cellular integrity and functionality, reducing the risk of early degradation and providing a more stable environment for *ex vivo* tissues during imaging.

In this study, the focus was specifically on assessing the SNR of the signal originating from the upper layer of the tissue. This emphasis was chosen due to the cellular composition of this area. As discussed earlier, the upper layer primarily consists of epithelial cells, which are generally more susceptible to rapid degrada-

tion. This vulnerability to degradation was apparent in the OpUS imaging results, where a noticeable decline in the signal strength of the upper tissue layer was observed over time.

In comparison, the signal from the deeper layer of tissue, presumed to correspond to the muscularis propria, demonstrated a low, but constant, signal strength of *ca.* 8 dB. The density of the muscularis propria, depending on the position within the GI tract, is around $1.05 - 1.10$ g/cm^3 [203]; the density of water, by comparison, is 1.0 g/cm^3, so a small SNR was expected. This tissue signal exhibited a minimal decline and remained relatively constant throughout the observation period. This difference in signal stability between the two layers is consistent with the inherent characteristics of their respective tissue types. The muscularis propria, being a muscle-based tissue, contains a higher concentration of structural components such as collagen and elastin fibers, which provide greater durability and resistance to degradation compared to the epithelial cells found in the upper layer [198]. As a result, the muscularis propria maintains its integrity and density, and therefore signal strength, for a longer period.

4.4.2 Hydrophone Positioning

While the FP hydrophones are omnidirectional receivers,the placement of the receivers must be considered for the quality of the reconstructed image. Here, the image reconstruction is carried out by considering a delay and sum of all received signals. In the case of a single point reflector, such as the tungsten wires used in the resolution studies, the received reflection will have a delay corresponding to the distance between the source and the transducer. For each transducer position, all the received signals from other positions can be delayed temporally to correspond with the position; the sum of these signals creates the representation of the reflector. Signals originating in line with the transmitter will give a strong signal, while signals outside of this line will sum to give a low value. However, this image reconstruction theory relies on the assumption that the transmitter and receiver are a single point and are omnidirectional. This would dictate an optimal position of a transmitter and receiver in the same physical space. However, this configuration has been noted

during the previous imaging study (Section 4.3) as a source of noise and artefact during pullback within the catheter. Here, noise is introduced as the motion creates interaction between the receiver and either the transmitter or the sheath. As such, it may be more efficient for the reliability of image acquisition, and the robustness of the probe, to introduce a separation between the elements and address any resulting signal losses in post-processing. This study focuses on the image reconstruction qualities with a transmitter-receiver separation.

4.4.2.1 Methods

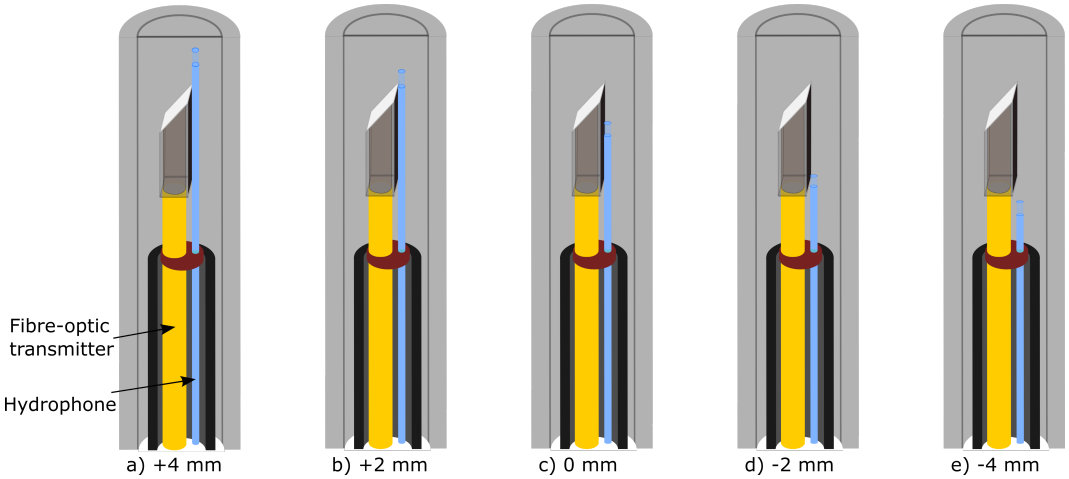

Figure 4.14: Transmitter-receiver separations of a) -4 mm, b) -2 mm, c) 0 mm, d) 2 mm and e) 4 mm.

The transmitter and receiver in the designed probe sit on the same axis, so the difference in positioning here is the separation between the transmitting surface and the tip of the hydrophone (Fig. 4.14). The effect of the hydrophone placement was measured using the tungsten wire phantom as described in Section 3.2.3.5. PSF's at two depths were chosen: one at 3.5 mm and one at 7 mm. The SNR was measured for these PSF's, along with the axial and lateral resolutions, at imaging speeds of $1-5$ mm/s at a set acquisition spacing of 50 µm for each hydrophone placement. The A-line spacing was constant at 50 µm. Each scan was repeated 10 times to assess the deviation in image quality.

Position	3.5 mm Ax. [µm]	3.5 mm Lat. [µm]	3.5 mm SNR	7 mm Ax. [µm]	7 mm Lat. [µm]	7 mm SNR
+4 mm	53 ± 5	115 ± 33	20.4 ± 1.4	54 ± 6	161 ± 40	17.8 ± 3.1
+2 mm	55 ± 7	140 ± 38	25.1 ± 4.0	55 ± 7	180 ± 43	19.0 ± 5.2
0 mm	51 ± 4	110 ± 25	23.6 ± 1.3	53 ± 5	150 ± 32	19.6 ± 2.5
−2 mm	49 ± 3	82 ± 15	22.1 ± 1.9	51 ± 6	120 ± 18	17.6 ± 2.5
−4 mm	50 ± 4	95 ± 20	22.4 ± 0.6	50 ± 5	126 ± 20	18.9 ± 1.2

Table 4.4: Image quality metrics for PSF target depths imaged with transmitter-receiver separations of −4 to +4 mm.

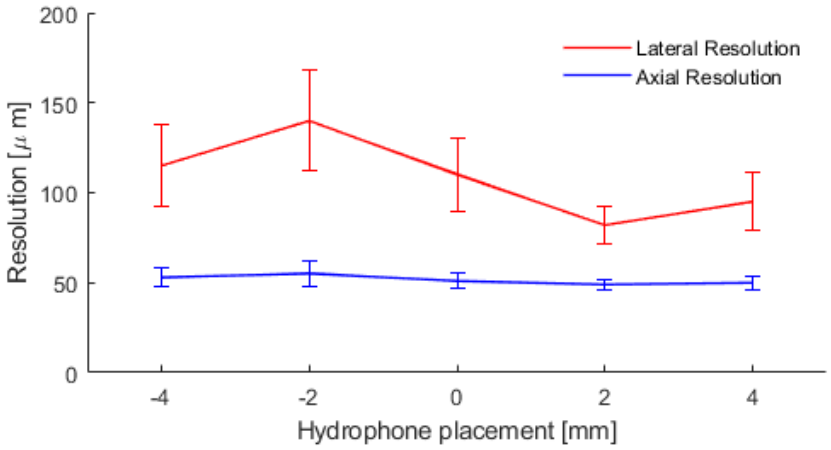

Figure 4.15: Axial and lateral resolutions measured by hydrophone placements for a target PSF at 3.5 mm depth. Data here shown as the average and standard deviation of the resolutions at speeds from $1 - 5$ mm/s.

4.4.2.2 Results

The results of the PSF quality at 3.5 mm can be seen in Fig. 4.15. The comparative results for the 7 mm depth can be seen in Table 4.4.

The axial resolution remains relatively consistent across the various hydrophone positioning, although is clearly the largest at the −2 mm position. For both the target PSF depths, the largest lateral resolution was shown by the −2 mm hydrophone position. The smallest lateral resolution was shown by the +2 and +4 mm hydrophone positioning. However, it is of note that the prone positions detect a higher SNR than those in the supine positions.

4.4.2.3 Discussion

The largest lateral resolution was exhibited by the -2 mm position. This position also showed the largest standard deviation in the resolution measurements, which implies that the poor resolution here is due to the accidental movement of the hydrophone during motion. The FP hydrophones can be considered omnidirectional receivers [136], so the angle of the US reflections should theoretically not limit the lateral resolution. However, the catheter is, by nature, small in diameter, and the current design of transmitter includes a glass capillary that is only slightly smaller than the catheter sheath. Irregular movement of the receiver could cause either the US reflections to be 'blocked', or the microresonator to be deformed through contact with either the sheath or the transmitter. Indeed, while acquiring the sample of 10 images using this configuration, the microresonator was often deformed to the point of requiring recalibration with the interrogation laser. This distortion may be caused by heating of the FP sensor, leading to a refractive index shift or cavity expansion, either due to self-heating or its proximity to the transmission surface. However, this is unlikely, as the water bath serves as an effective heat sink, and the interrogation power used is relatively low. By moving the hydrophone tip further along the lateral plane, it limits the possibility that the receiver will be distorted during acquisition.

However, placing the receiver in a prone position, such as the 2 or 4 mm, could pose a risk of damage to the fragile FP receiver. This is especially true during the 'push' to the start position of the image acquisition process. Given that the final tool must be flexible and cannot guarantee a perfectly straight sheath, pushing the unprotected receiver through it could deform the microresonator or even cause permanent damage. As such, despite the prone positions indicating the best quality of image reconstruction, these configurations cannot be used.

An alternative approach might involve modifying the dimensions of the probe. For instance, using a larger catheter sheath could reduce contact during motion, though this would make the probe incompatible with existing clinical workflow. Another option is to use a smaller optical fibre and capillary tip in the transmit-

ter, which would decrease unintended contact and increase beam divergence [175]. However, this could complicate modifications due to the angled surface and increase the transmitter's fragility. Additionally, manufacturing a miniature fiber guide to fit inside the catheter and keep the transmitter and probe aligned in parallel could address the issue, but it might introduce friction during motion and add strain on the motor. Lastly, an alternative transmitter design could emit US from an angled face, eliminating the need for a capillary and reducing the sheath diameter. While this would change the imaging perspective away from the direct vessel wall view, delay and sum reconstruction techniques would still produce a similar image orientation.

4.5 Study IV: Rapid Acquisition

The results outlined in Section 4.3 indicate that continuous acquisition in a lateral-viewing configuration acquires comparable image quality to those achieved by the raster scanning process in a forward-configuration demonstrated in Section 3.5. However, in order to satisfy the subsecond acquisition requirement (Section 1.2), this technique requires further optimisation.

In this study, the OpUS imaging probe with lateral dimensions compatible with standard-of-care clinical endoscope working channels that was demonstrated in Section 4.3 was used in conjunction with a modified operating system. The probe was housed within an US-transparent sheath. This system was capable of pullback speeds of ≤ 500 mm/s. A resolution phantom was used to assess the probe at acquisition speeds of $10-100$ mm/s. To demonstrate the potential of the device for clinical imaging, an *ex vivo* swine oesophagus was imaged using the working channel of a mock endoscope for device delivery.

4.5.1 Methods

The proximal end of the OpUS probe was mounted on a motorised translation stage (DDSM100, Thorlabs, UK, maximum speed: 500 mm/s, travel range: 100 mm) to provide pullback motion. The probe was clamped such that the Y-joint and US-transparent sheath were held stationary whilst the torque coil with the optical fibres fixed inside was mounted on the translation stage (Fig. 4.9c)). To acquire US im-

ages, the probe was translated laterally at a constant velocity within the sheath with respect to the sample surface. A-lines were acquired at a lateral spacing of 25 microns. The acquisition rate was varied to maintain the A-line spacing depending on the translation velocity, i.e. for a velocity of 100 mm/s a repetition rate of 4 kHz was used. Each A-line comprised 4000 data points which corresponded to a total imaging depth of *ca.* 30 mm. The impact of larger A-line spacing was investigated by removing A-lines in post-processing.

4.5.1.1 Image Processing

Acquired A-lines were concatenated, followed by the application of a bandpass filter (Butterworth, 4^{th} order, $1.5-40$ MHz). Subsequently, a cross-talk algorithm was applied to remove the US signals transmitted directly from the generation fibre to the reception fibre, as described previously [177].

This was followed by the application of digital TGC [179]. This was achieved by multiplying the signal by the following gain factor:

$$g(i) = \frac{min(i, i_{max})^{\gamma}}{i_{max}} \tag{4.1}$$

where i is the sample index of the signal. Parameters i_{max} and γ were empirically designated as 650 and 2 respectively. The US image was reconstructed using the k-Wave toolbox [77], using a k-space method based on the fast-fourier transform. Finally, the signal envelope was found using the absolute value of the Hilbert transform followed by a log transformation.

4.5.1.2 Imaging Targets

Two imaging targets were used for this study; a resolution phantom and *ex vivo* porcine oesophagus. The resolution phantom was used to assess the probe capabilities in terms of axial and lateral resolution and SNR. It comprised a plastic frame strung with regularly spaced tungsten wires (OD: 27 μm). The phantom was mounted in a water bath and angled with respect to the OpUS catheter such that the wires were positioned at increasing depths (Fig. 4.9c)).

Imaging of *ex vivo* porcine oesophageal tissue (Medmeat, UK) was carried out

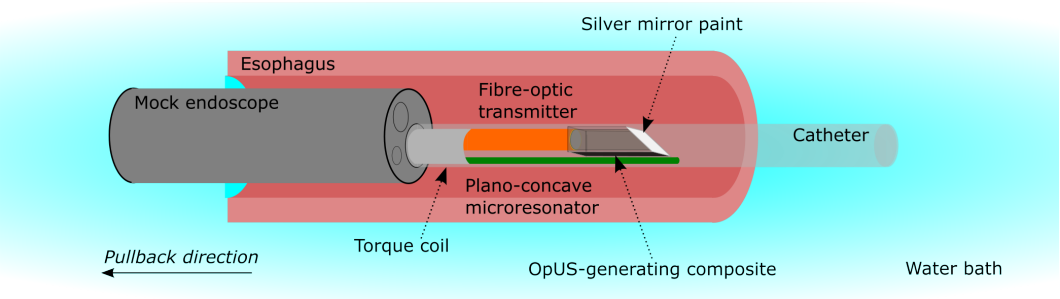

Figure 4.16: Schematic of lateral probe encased in an ultrasonically-transparent sheath inside the working channel of a mock endoscope inserted into an oesophagus.

to investigate the clinical potential of the OpUS probe. The tissue was acquired frozen, and subsequently defrosted and submerged in a 1% saline solution for experiments. The tissue was imaged immediately after defrosting. A 10 cm section of the oesophagus was mounted in a water bath and the mock endoscope was inserted into the lumen (Fig. 4.16). The OpUS probe was inserted through the instrument channel of the mock endoscope such that it extended out of the distal end into the oesophageal lumen. The pullback protocol outlined in Section 4.3.1.1 was used to acquire tissue images, with the US transparent sheath held stationary.

4.5.2 Results

4.5.2.1 Resolution Phantom Imaging

The tungsten wire phantom appeared in the reconstructed images as a series of PSF's which were used to measure the resolution of the imaging system (Fig. 4.17a)). The FWHM value of the resulting PSFs in the OpUS images were used to provide values for the axial and lateral resolutions. Here, all PSF's were visible in the images acquired (Fig. 4.17a)). The SNR at an A-line spacing of 25 µm decreased with increasing depth by *ca.* 1 dB/mm, from 43 dB for the closest wire (1.5 mm) to 32 dB for the furthest (12.5 mm) (Fig. 4.17d)). The A-line spacing had negligible impact on the SNR values (Fig. 4.17d)). Additionally, increasing imaging speed from 10 mm/s to 100 mm/s had negligible impact on the SNR (Fig. 4.18c)).

For an A-line spacing of 25 µm, the lateral resolution worsened with increasing depth from 152 µm for the closest wire to 214 µm for the furthest (Fig. 4.17c)).

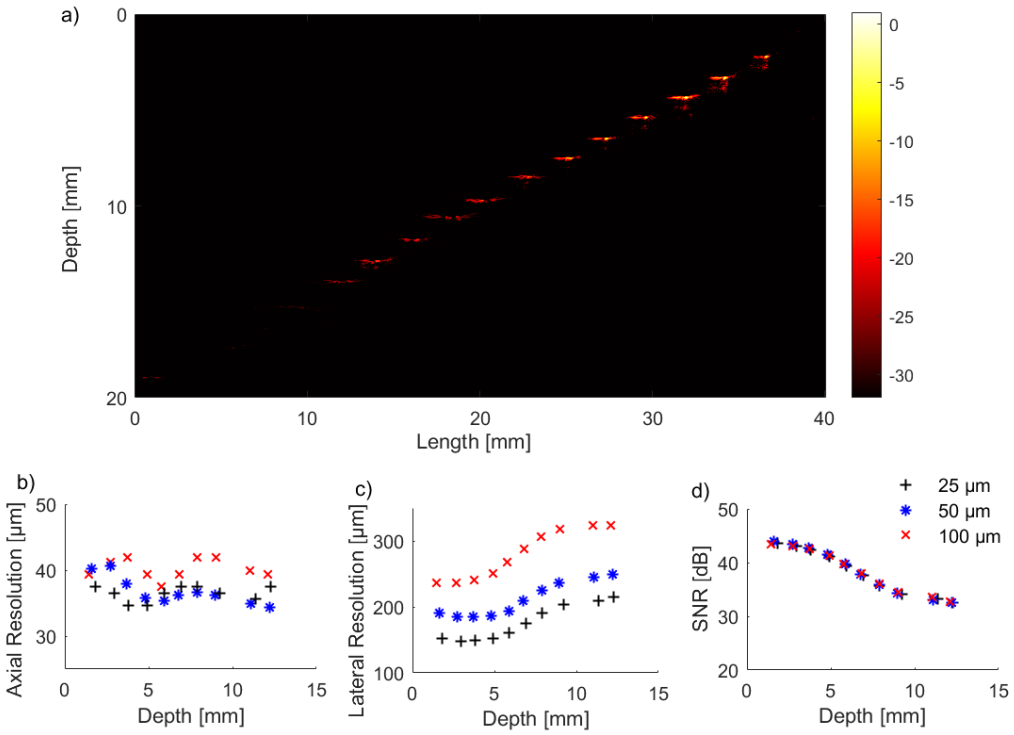

Figure 4.17: a) Reconstructed OpUS image of the tungsten wire resolution phantom acquired using a 100 mm/s fast-pullback acquisition with an A-line spacing of 25 µm. b) - d) OpUS probe performance with imaging depth for an A-line spacing of 25 µm (black cross), 50 µm (blue star) and 100 µm (red cross). b) Axial resolution. c) Lateral resolution. d) Signal to noise ratio (SNR).

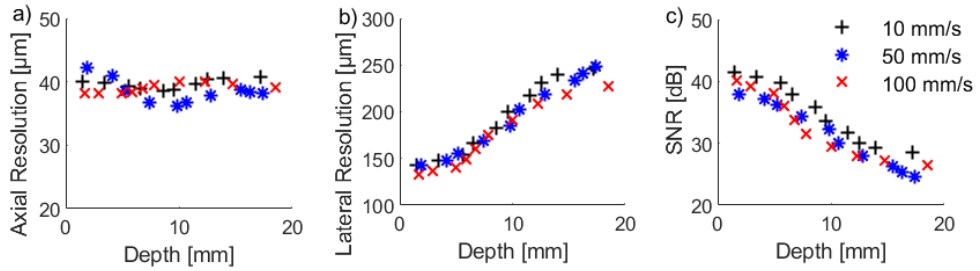

Figure 4.18: OpUS probe performance with imaging depth for an A-line spacing of 25 µm acquired using a pullback speed of 10 mm/s (black cross), 50 mm/s (blue star), and 100 mm/s (red cross). a) Axial resolution. b) Lateral resolution. c) Signal-to-noise ratio (SNR).

This relationship was replicated in the reconstruction at larger A-line spacing, albeit with worse overall resolution (Fig. 4.17c)). The best lateral resolution for a 50 µm spacing was 190 µm, whilst for a spacing of 100 µm it increased further to 236 µm.

This was also seen in the worst lateral resolutions for each spacing; at a depth of 13 mm the 50 and 100 µm spacing showed resolutions of 249 µm and 323 µm, respectively. Further, similar to the SNR, it was found that the pullback speed had a negligible impact on the lateral resolution (Fig. 4.18b)).

The axial resolution was consistently better than the lateral resolution. Unlike the lateral resolution, the axial resolution was largely independent of the system parameters and remained relatively constant at 37-43 µm, independent of the A-line spacing, pullback speed, or target depth (Fig. 4.17b), Fig. 4.18a)). For example, the best axial resolution at 10 mm/s was measured to be 37 µm, while the best axial resolution at 100 mm/s was measured to be 38 µm.

4.5.2.2 Oesophagheal Tissue Imaging

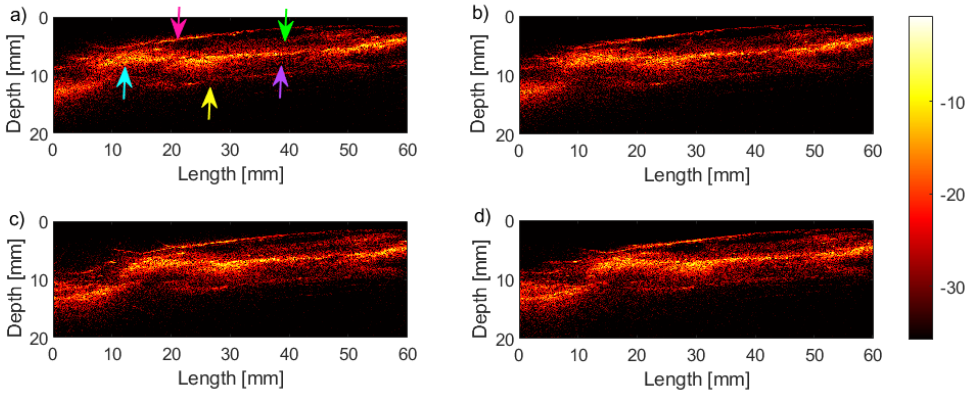

Figure 4.19: Reconstructed OpUS image of oesophageal tissue acquired using a) - b) 10 mm/s fast pullback reconstructed at an A-line spacing of a) 25 µm and b) 100 µm. c) - d) corresponding images taken using 100 mm/s fast-pullback at an A-line spacing of c) 25 µm and d) 100 µm. Right: dB scale bar. Part a) labels showing: inner edge of tissue (pink), outer edge of tissue (yellow), oesophageal mucosa (green), submucosa with oesophageal glands (blue) and muscularis propria (purple).

Ex vivo porcine oesophagus was imaged to investigate the clinical potential of the OpUS probe and demonstrate its capability for gastrointestinal imaging. The full thickness of the oesophageal wall was visible in the image, with both the inner (pink arrow) and outer surface (yellow arrow) appearing as distinct boundaries against the background (Fig. 4.9). Several distinct regions were apparent, which, on comparison with previous US images of the oesophagus, were thought to corre-

spond to the oesopheal mucusa (green arrow), submucosa with oesophageal glands (blue arrow), and muscularis propria (purple arrow) [204]. The SNR was highest in the layer thought to correspond to the submucosa, with a value of 32 dB.

The acquisition speed was found to have minimal impact on the quality of the OpUS images from a qualitative perspective (Fig. 4.19a),c)). Further, the SNR was found to decrease marginally with the increase in pullback speed, as demonstrated with the resolution phantom results. Additionally, despite the known reduction in lateral resolution associated with the increased A-line spacing, this had minimal impact on the qualitative outcome of the oesophageal imaging (Fig. 4.19a),b)). The general oesophageal shape was preserved and subsurface details could be well visualised for all A-line spacings.

4.5.3 Discussion

Images acquired of a resolution phantom demonstrated axial resolutions < 40 µm. This is consistent with previous OpUS devices such as [138] or [35] who both reported axial resolutions of 50 µm, or [205] who reported an axial resolution of 35 µm. With commercial miniaturised piezoelectric probes, axial resolutions of *ca.*100 µm have been reported with a corresponding tissue penetration of 4 - 8 mm [194, 195]. As with conventional US imaging, axial resolution is typically limited by the bandwidth of both the generated US and the US receiver [63]. Whilst the axial resolution provided here exceeds the clinical requirements, it could be improved further. This can be achieved by increasing the US reception bandwidth, or the bandwidth of the generated US pulse. The received bandwidth could be improved by decreasing the thickness of the FP cavity; however, this would create a decreased sensitivity [177]. The generated bandwidth is dictated by both the brevity of the excitation pulse and the thickness of the composite coating [119]. The transmitted US bandwidth, and therefore the axial resolution, could likely be improved by minimising the thickness of the optical absorber or adjusting the excitation pulse duration [206]. Since the brevity of the excitation pulse or the composite coating is not altered during either the change in acquisition step-size or the lateral pullback speed, it would be expected that the axial resolution remains independent of the

imaging parameters such as A-line spacing or pullback speed. This was reflected in the results. The independence of the axial resolution from the A-line spacing means that less computationally intensive datasets can be acquired without sacrificing image quality. Additionally, it was found that the axial resolution was independent of the pullback speed, as expected, which suggests that the pullback speed could be increased to allow for larger imaging apertures or shorter acquisition times.

Similar to the axial resolution, a good lateral resolution was achieved in this study, with values as low as 150 µm. These values were comparable to a typical commercial US device which can achieve lateral resolutions of 200 µm depending on the bandwidth and frequency of the device [63, 194, 195], as well as being comparable to previously reported OpUS transducers [193, 177, 88]. Unlike the axial resolution, the lateral resolution was dependent on various imaging parameters. Firstly, there was an inverse relationships demonstrated between the depth and the acquired lateral resolution. This relationship is similar to that demonstrated in previous OpUS studies [196, 177] as well as demonstrated in Section 3.5. As outlined in Section 2.2.3, lateral resolution is dictated by the width of the US beam and the bandwidth of the US [63]. Since the image reconstruction here relies on the premise of whole-field insonification, a wider beam divergence will lead to a higher lateral resolution. The resolution could likely be improved by increasing the US beam divergence, for example by changing the aperture size. However, changing the aperture size could increase the probe size thereby making it incompatible with a typical endoscope. Even a marginal increase in size could introduce more friction during pullback within the sheath which would be detrimental to the image quality. Secondly, there is an additional inverse relationship between the lateral resolution and the A-line spacing. Typically it is the aim to achieve the smallest possible resolution. Here, however, it would be beneficial to be able to provide real-time image reconstruction and analysis, so the compromise must be between the computational intensity of the acquired data and the resulting image quality, as mentioned previously. Using this as a baseline, the A-line spacings of 25 and 50 µm are both more than adequate for the purpose here. Finally, the last imaging parameter of

consideration here is the pullback speed. This work used a rapid linear pullback for image acquisition. The use of the pullback technique resulted in drastically reduced acquisition times than those previously reported using a raster scanning approach, or indeed the slower pullback speeds described in Section 4.3. It appears from the results that the pullback speed has minimal impact on the resulting image quality (Fig. 4.18). This supports the conclusions drawn from Section 4.3.

The maximum pullback velocity used in this study was 100 mm/s which enabled imaging over an 5 cm aperture in 0.5 s. The translation stage used here can reach speeds of 500 mm/s. This could be beneficial for larger imaging apertures, capable of imaging 50 cm in 1 s. The average adult human oesophagus is approximately 40 cm in length. To this end, this faster acquisition rate could acquire more pullback scans within the timespan of a regular endoscopy, thereby minimising the sampling error that is present in the acquisition and pathologic interpretation of biopsies which is currently the primary detection method of BE [207, 208]. In this study, pullback speeds were limited to 100 mm/s. An increased pullback speed could still create an A-line spacing of 25 µm by utilising a higher repetition rate. However, this increased rate would come at the expense of a higher energy deposition rate in the coating, which may lead to heating or damage to the coating (see Section 2.2.1). This requires exploration in further studies if the repetition rate is to be increased further. The results here showed that even at the highest speeds with an A-line spacing of 50 µm, the resolution is still comparable to previously reported devices [177, 209, 63], even up to depths of 20 mm, which exceeds the largest thickness of the oesophagus. The results here show that an increased A-line spacing of 50 µm can be used without significant detraction of image quality. Therefore, using a 50 µm spacing combined with a 4000 Hz acquisition rate, the maximum applicable pullback speed is 200 mm/s, meaning the acquisition of a single pullback scan of a 100 mm aperture could be achieved in 0.5 s. This satisfies the sub-second acquisition times outlined in the requirements given in Table 1.1.

The *ex vivo* swine oesophageal image demonstrated clinically relevant details with the tissue layers providing differing contrast. The full thickness of the tis-

sue was visualised and an SNR of 32 dB was achieved without the use of averaging. Further, tissue boundaries were observed and demonstrated similarities to US imaging acquired in previous studies [210, 211]. In future work, the origin of these boundaries could be verified with tissue histology or another method of ground truth imaging. This study was limited to healthy tissue, but could be extended to include imaging of diseased tissue to assess the ability to differentiate BE. This might be carried out on *ex vivo* human tissue or in an animal model. The primary clinical aim of oesphageal imaging would be to ascertain the presence of HGD commonly found with the commencement of BE, which is widely considered to be a significant precursor to oesophageal adenocarcinoma [212, 213, 214]. This is found in the mucosal tissue [215], which was believed to be visualised beneath the tissue surface (Fig. 4.19, green and blue arrows). The clear delineation of these layers, in conjunction with the high resolutions and sub-second acquisition speeds achieved, indicates the clinical potential of this device.

However, a key issue encountered at high speeds is movement in the components comprising the device. For high speeds, the transmitter and receiver stability was reduced, leading to a reduction in image quality. Whilst the motor used can exceed the current maximum pullback speeds, the pullback motion creates friction within the device between the two elements, which causes a reduction in the image quality. Indeed, friction and related artefacts were noted in the images acquired using slower pullback speeds outlined in Section 4.3. To overcome this in future studies the device fabrication method could be modified. This could include the introduction of a custom micromachined housing to hold the transmitter and receiver relative to one another. Alternatively, the device fabrication method could be modified to remove the bulky capillary, such as further modification of the tip of the optical fibre to create a flat emission surface on the lateral face, or to increase the angle of the polished face and emit US from this angled face.

4.6 Study V: Lateral Probe Optimisation

One of the conclusions from previous studies suggests that modifying the transmitter would enhance the robustness and mechanical flexibility of the probe. The current probe design occupies a significant amount of space within the sheath, which can lead to image artefacts, increased friction resulting in additional load on the motor, or even permanent damage to the transmitter or receiver. Furthermore, the use of a capillary creates challenges for integrating the transmitter into the probe and its housing. The proposed modifications include:

- Reducing the diameter of the optical fibre used for the transmitter. As previously mentioned, this would increase beam divergence but at the cost of reduced penetration depth. Additionally, it would make the transmitter more fragile, especially during fabrication, and complicate the accuracy of the polished angle. This issue could be mitigated by tipping the fibre with the capillary before polishing, which would increase the surface area exposed to the polisher. However, this design does not resolve the challenge of integrating the transmitter into the probe.

- Compression of a polymeric fibre to create an eccentric source such as [216]. By compressing the tip of a fibre from a circular shape to an oval, a 'flattened' surface could be created on the side of the tip of the fibre. Polishing the distal face to a 45° angle, coating this face with mirror paint, and coating the flattened side of the fibre would theoretically allow for lateral US emission without the need for a capillary. However, this configuration could significantly influence the US profile. The 'flattened' side is more likely to be convex than planar, meaning both a larger beam divergence and a smaller temporal profile [89]. Furthermore, the altered geometry of the reflective face will reduce the area of incident light on the composite coating, thus generating a wide insonification in the direction of the length of the fibre as well.

- Applying the composite coating to the polished face. This would create a transmitter that would generate US at a 45° angle to the direction of the fi-

bre. While not directly imaging the vessel wall, the premise of whole-field insonification would result in a lateral-viewing reconstructed image. Additionally, this design would minimise the required space within the sheath and simplify probe integration by removing the capillary. It would also preserve the existing image acquisition and processing methods while enhancing the mechanical flexibility of the probe. In a clinical context, a 45° view may provide better visualisation of tortuous or folded sections of the GI tract than a perpendicular view of the vessel wall.

4.6.1 Fabrication of a Modified Transmitter

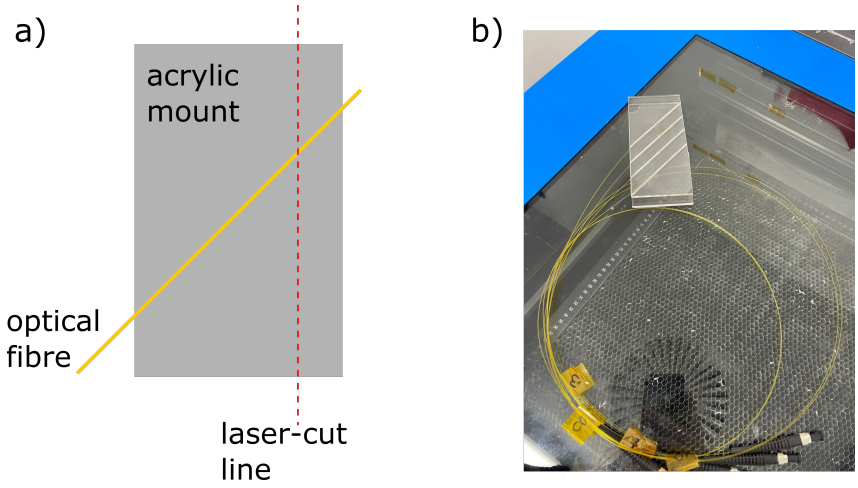

Figure 4.20: a) Schematic of fibre and acrylic mount configuration for cutting fibres to a 45° angled surface. b) Photograph of cut fibres in the acrylic mount.

The fibres used here were SMA connectorised silica core/cladding optical fibres with a 400 µm diameter and a polyimide buffer coating (FG400LEP, Thorlabs, UK), as is used in Section 4.2. The polyimide layer was carbonised and stripped from the fibre, followed by perpendicular cleaving as normal.

Subsequently, the fibre was clamped in an acrylic mount at a 45° angle (Fig. 4.20). This mount was placed in a laser cutter (VLS4.60, One Touch Laser, UK) and cut lengthwise (Fig. 4.20a)). This created a uniform, planar 45° face at the tip of the fibre.

This face was subsequently coated with a bilayer rGO-PDMS composite coating (Fig. 4.21), as outlined in Section 3.2.1.5. Briefly, 500 mg of rGO functionalised

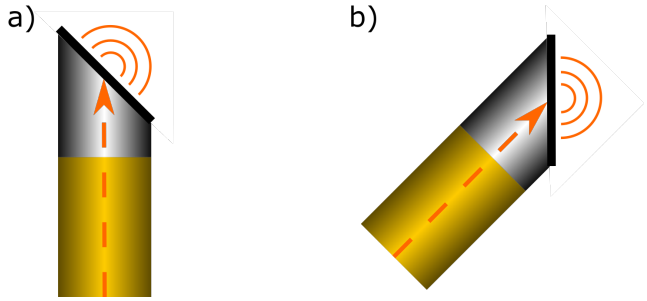

Figure 4.21: Schematic of modified transmitter.

with octadecylamine (805084, Sigma Aldrich, UK) was sonicated for 20 s in 2.5 ml of xylene. This was deposited on the angled surface and left to dry for *ca.* 12 hours. Subsequently, an overcoat of PDMS thinned with xylene was applied to the rGO coating to create a bilayer composite.

4.6.2 Characterisation of a Modified Transmitter

4.6.2.1 Acoustic Characterisation

The acoustic spectra of the transmitter was acquired using the protocol outlined in Section 3.2.2.2. Briefly, the study fibre was mounted on a stationary clamp stand directly opposite a 200 µm needle hydrophone, which was centred on the US beam and set to a transmitter-receiver distance of 1.5 mm. The study fibre was rotated such that the emission surface faced towards to hydrophone (Fig. 4.21b)). The received US pressure was measured, and the bandwidth obtained by applying a Fourier transform and the hydrophone calibration to the acquired time-series.

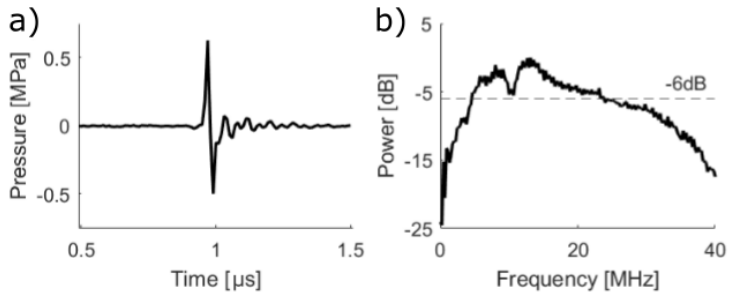

Figure 4.22: a) Transmitted ultrasound time-series measured at 1.5 mm. b) Corresponding ultrasound power spectrum.

The generated US peak-to-peak pressure level was measured as 1.12 MPa (Fig. 4.22a)) at 1.5 mm from the coated face with a corresponding −6 dB bandwidth

of 22 MHz (Fig. 4.22b)). This is comparable with the profile of the US generated by both the forward- and lateral-viewing transmitters demonstrated in Section 4.3.

4.6.2.2 Beam Divergence

This modified transmitter emits US in a different direction to those outlined in the previous sections of this chapter. As such, the beam profile must be assessed to evaluate the potential for lateral imaging in this configuration.

The beam divergence was acquired using the protocol outlined in Section 4.2.1.2. Briefly, the hydrophone was moved to a fixed distance from the emitting face of the transmitter (1.5 mm) and centred on the maximum US pressure, as with acoustic characterisation. Vertical and horizontal raster scans consisting of 61 measurements were then acquired intersecting this point using the motorised stages at an acquisition step size of 50 µm. This equated to a 9.3 mm^2 grid. The peak pressure p was extrapolated backwards for each position, resulting in an array of cross-sections of the US beam. The size of the FWHM cross section was extrapolated backwards to give the area of the beam over distance.

A beam spreading assessment was carried out both with the hydrophone perpendicular to the length of the fibre (Fig. 4.21a)) and directly facing the emission surface of the transmitter (Fig. 4.21b)).

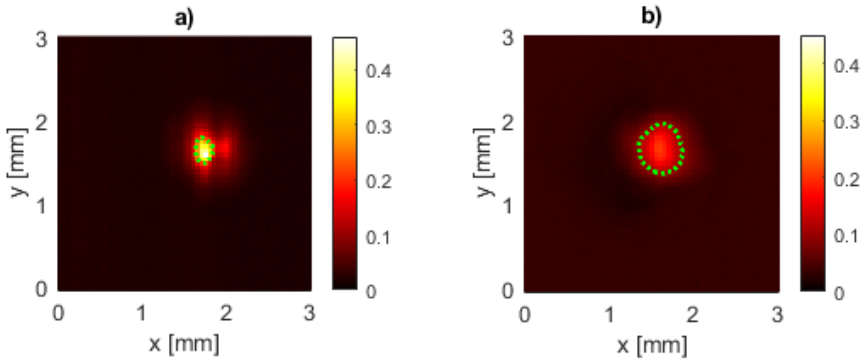

Figure 4.23: Beam divergence profiles for the modified lateral transmitter acquired at a distance of 1.5 mm in a view a) perpendicular to the fibre direction (see Figure 4.21a)) and b) perpendicular to the emitting face (see Figure 4.21b)).

The beam divergence of the modified transmitter was shown to spread at ap-

proximately the same rate as both the forward-viewing and original design of lateral transmitters. Here, a maximum FWHM of 9.3 mm^2 was measured, as well as an initial spot area of *ca.* 0.4 mm^2, corresponding the size of the emission surface. This correlates with the theoretical beam spreading given by [175]; despite the change in angle of emission, the size and shape of the emission surface remained consistent.

Of particular interest is the comparison of the initial profiles of the transmitter based on orientation. Although both profiles exhibit a similar total area of maximum pressure, the initial profile shown in Figure 4.23a) exhibits a slightly compressed shape, with pressure decaying only towards the right side and no lower pressures visible on the left. In particular, a small 'shadow' of pressure appears at *ca.* 2 mm in the x direction. This is likely due to the orientation of the fibre; the 'shadow' likely corresponds to the lower edge of the polished face. In contrast, the profile in Figure 4.23b) closely resembles those of the forward-viewing transmitters shown previously. This similarity indicates a suitable beam profile for application to imaging in the context required here.

4.6.3 Rapid Acquisition B-Mode Imaging with a Modified Probe

This transmitter was subsequently integrated into the OpUS probe and housing as outlined in Section 4.2.2. Briefly, both the transmitting and receiving elements were encased in a protective torque coil and fixed in place. This probe was subsequently housed in a US-transparent sheath and placed inside a mock endoscope. The key difference here was that the smaller diameter of the transmitter tip enabled it to be threaded forward through the torque coil, eliminating the need to remove the SMA connector and reconnecting the proximal end of the fibre after back-threading.

4.6.3.1 Methods

This probe was mounted on the motorised translation stage for imaging as described in Section 4.5. Briefly, the probe was clamped such that the Y-joint and sheath were held stationary while the probe was translated laterally at a constant velocity within the sheath with respect to the imaging target. A-lines were obtained at a lateral spacing of 25 μm, with each A-line comprising 4000 data points corresponding to a

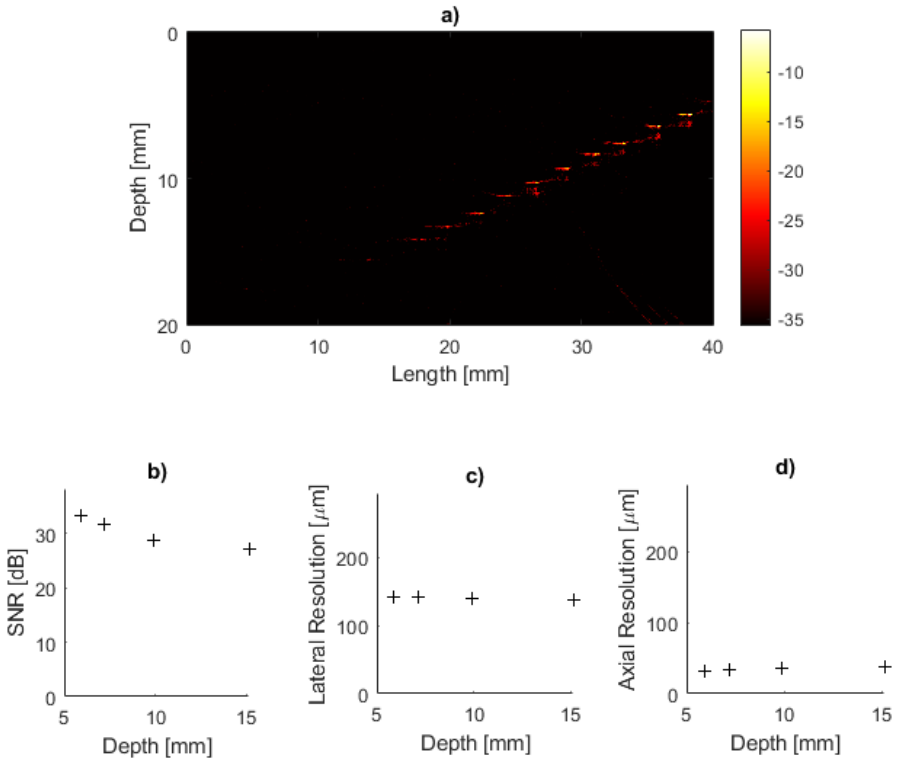

Figure 4.24: a) Reconstructed OpUS image of the tungsten wire resolution phantom acquired using the modified probe with a 100 mm/s acquisition speed with an A-line spacing of 25 µm. b)-d) OpUS probe performance with imaging depth. b) Signal to noise ratio (SNR). c) Lateral resolution. d) Axial resolution.

total imaging depth of *ca.* 30 mm.

Images were acquired of a tungsten wire resolution phantom at a speed of 100 mm/s. The acquired A-lines were concatenated, followed by a the application of a bandpass filter and a cross-talk removal algorithm [177]. TGC was applied [179], followed by image reconstruction using the k-Wave toolbox [77]. Finally, the signal envelope was found using the absolute value of the Hilbert transform followed by a log transformation. The acquired images were assessed in terms of the SNR, lateral resolution, and axial resolution of the PSF's.

4.6.3.2 Results

The tungsten wire phantom appeared in the reconstructed images as a series of PSF's (Fig. 4.24a)). The FWHM of the PSF's were used to provide values for the axial and lateral resolutions. The SNR decreased by *ca.* 0.5 dB per mm, from 33 dB for the closest wire (6 mm) to 28 dB for the furthest (15 mm) (Fig. 4.24b)). Increasing the imaging speed between $10-100$ mm/s was found to have negligible impact on the SNR.

The lateral resolution appeared consistent with increasing depth from 125 µm for the closest wire to 130 mm for the furthest (Fig. 4.24c)). Similar to the SNR the impact of acquisition speed was found to have a negligible impact on the lateral resolution.

The axial resolution was consistently better than the lateral resolution. Unlike the lateral resolution, the axial resolution was largely independent of the system parameters and remained relatively consistent at *ca.* 40 µm (Fig. 4.24d)).

4.6.3.3 Discussion

Images acquired of the resolution phantom demonstrated axial resolution *ca.* 40 µm. This is consistent with previous OpUS devices [138, 35, 205], but importantly, is consistent with the axial resolution acquired by the original design of transmitter shown in Section 4.5. As seen in the previous studies, the axial resolution appears unaffected by parameters like acquisition speed or PSF depth.

Similarly, a good lateral resolution was achieved in this study, with values as low as 125 µm. These values are comparable with previous OpUS devices [193, 177, 88] and typical commercial US devices [63, 194, 195]. Importantly, these results are consistent, and indeed marginally improved, with the lateral resolution acquired by the original design of transmitter shown in Section 4.5. As outlined previously, the lateral resolution is dictated by the width of the US beam; since the image reconstruction here relies on the premise of whole-field insonication, it is likely that the lateral resolution is improved by the out-of-plane contributions of the new field-of-view.

It is important to note that the lateral resolution here appears less influenced by

the depth of the PSF. This could be attributed in part to the application of TGC, but can also be explained by the out-of-plane contributions given by the US emission angle. This is supported by the relationship between the depth and the SNR of the PSF's; while signal loss is present, it is significantly smaller than noted in the previous study. However, it is important to note that the depths assessed here are ≤ 15 mm, while the previous studies reach depths of 20 mm. As concluded from the previous studies, the lateral resolution appears unaffected by the increase in acquisition speed.

The new configuration also enhanced the robustness and reliability of the probe, although this improvement is not quantified in the results. There was reduced interaction between the receiver, sheath, and transmitter during the image acquisition process, resulting in fewer noise and artefacts in the reconstructed images. This is likely due to the probe occupying less space within the sheath. Furthermore, there were fewer breakages, and the sheath's angle became more easily adjustable.

4.7 Chapter Conclusions

In this chapter, a novel method for sub-second acquisition of OpUS images while maintaining image resolutions and depths suitable for minimally invasive surgical applications was demonstrated. This was paired with a bespoke device comprising miniaturised components which are compatible with current clinical endoscopes. The lateral ultrasound transmitter developed for the study exhibited peak-to-peak pressure in excess of 1 MPa with a corresponding -6 dB bandwidth of > 20 MHz. These are consistent with both previous high-bandwidth rGO-PDMS OpUS devices [35] and previous side-viewing transmitters [139]. This enabled imaging resolutions as low as 45 µm and 120 µm in the axial and lateral extent respectively, with a corresponding SNR of 42 dB.

Crucially, the resolution appears to stay constant during changes in acquisition speed, both using the slower ($1-5$ mm/s) and faster speeds ($10-100$ mm/s). This is a key result for the development of the probe and optimisation of the required scan time for future medical translation. The minimal variation in resolution is

likely due to errors in the probe such as the introduction of air bubbles in the EBUS sheath or the inadvertent twisting of the fibres during pullback creating issues with acquisition of reflected signal.

The positioning of the hydrophone in reference to the probe twisting was investigated, using a variety of positions ranging from -4 to $+4$ mm. The optimal positioning was determined to be the positive positions where the hydrophone sits prone to the transmitter capillary, thus minimising the blocking of received signal or the excessive cross-talk from being positioned directly in front of the emitting face. This study has highlighted two avenues for probe improvement: smaller capillaries or miniaturised fibre guides to fix the transmitter and receiver tips in position. A modified transmitter was developed and tested within the presented system. This transmitter demonstrated comparable image quality alongside a reduced interaction between the probe elements during motion.

To demonstrate the potential of the device for clinical imaging, an *ex vivo* swine oesophagus was imaged using the working channel of a mock endoscope for device delivery. The full thickness of the oesophagus was resolved and several tissue layers were present in the resulting US images.

This work represents a significant step in the surgical translation of minimally invasive OpUS imaging. The subsecond acquisition times while maintaining competitive imaging resolutions and high imaging depths would be beneficial for many clinical applications. Additionally, the packaging of the probe in a clinically compatible catheter is a key step towards bringing OpUS through medical translation. It is expected that this device will be further developed for *in vivo* studies, with rigorous robustness testing and optimisation of handling for a preclinical environment. A further area of development is the addition of complementary imaging and therapeutic modalities. OpUS has shown promise for multi-modal devices, with previous studies including a combination with photoacoustic imaging [142] and optical ablation [140]. The presented probe could be modified to incorporate a secondary modality by using a wavelength-selective coating such as those previously presented from PDMS-AuNP [3] or PDMS-Epolight [5]. The comparable imaging

parameters demonstrated by this imaging method with both other OpUS modalities such as B-mode imaging [35] or rotational imaging [139], and conventional piezoelectric US [194] is indicative of the potential of rapid acquisition imaging in clinical application.

Chapter 5

Dual Modality OpUS Fluorescence Imaging

This chapter is based on work currently submitted for publication, and describes the preliminary development of a multi-modal optical imaging system, utilising both OpUS imaging and FlS sensing. This chapter is supported by the work carried out by Deniz Terzioglu for his undergraduate research project, supervised by both Dr Richard Colchester and the author.

5.1 Introduction

Fluorescence spectroscopy has been used both *in vitro* and *in vivo* to distinguish between normal and malignant tissue in several organs, including breast, lung, colon and oesophagus [11, 217, 218]. However, in most cases, the lesions are visible and can be readily diagnosed by the clinician. While these studies validate the tool's accuracy, it also holds potential to aid clinicians in diagnosing impalpable conditions. In BE, for example, the dysplasia within the mucosal level is not visually distinguishable from nondysplastic areas [11]. Extensive pinch biopsy specimens are required to detect dysplasia in patients [219]. As such, an alternative technique is required to improve the detection of HGD in patients with BE.

This chapter focuses on the addition of FlS as a complementary modality for OpUS imaging. Using an excitation light source of a specific wavelength, the imaging targets emit fluorescence at a range of wavelengths. FlS detects the intensity

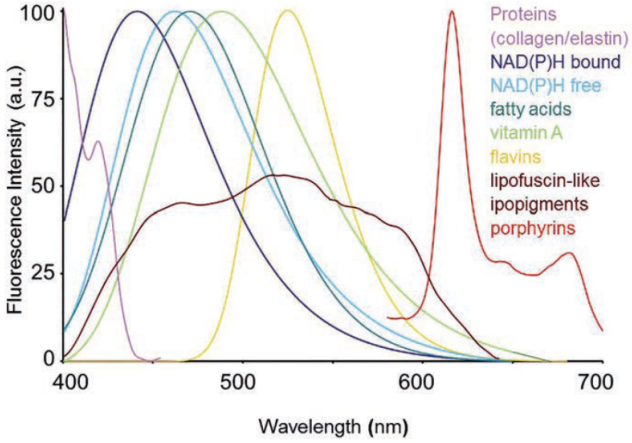

Figure 5.1: Typical spectral profiles of autofluorescence emission from endogenous fluorophores. Taken from [10].

of the fluorescence at particular wavelengths from the surface of the imaged tissue, which can be utilised to identify differing cell types. Typically, different cell types will fluoresce at different wavelengths, which can be utilised to identify tissue types (Fig. 5.1). Additionally, healthy tissue will display different fluorescing properties to diseased tissue. For example, the degree of dysplasia in oesophageal tissue with BE will be demonstrated in the measured fluorescing spectra, as shown in Fig. 5.2.

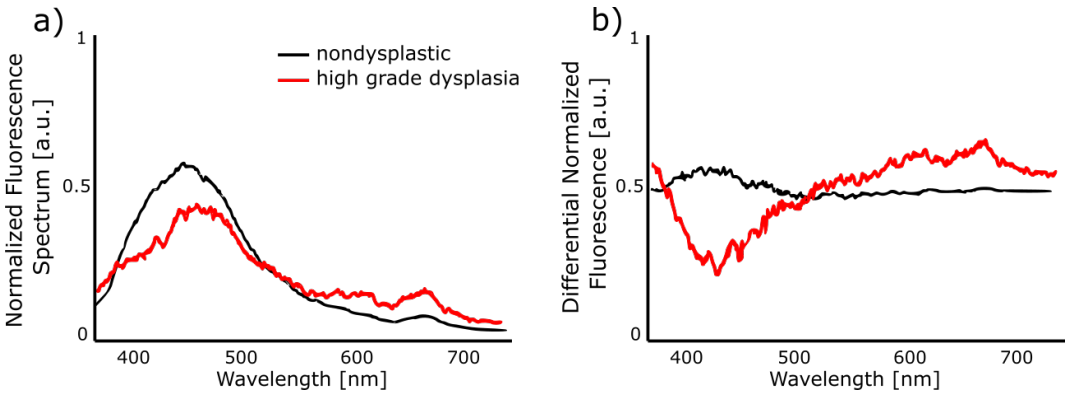

Figure 5.2: a) Normalised fluorescence spectrum from nondysplastic (black) and HGD (red) BE mucosa. b) Corresponding differential normalised fluorescence spectrum for nondysplastic (black) and HGD (red) BE mucosa. Adapted from [11].

A tool comprising of FlS in conjunction with OpUS imaging would yield valuable information about both biomarkers on the tissue surface and tissue density under the surface. The two data sets can be combined and co-registered to complement each other and provide a uniquely invaluable tool. For example, as light

dissipates over distance, FlS yields less intensity for surfaces further from the excitation source. By utilising the detailed depth data provided by the simultaneous OpUS image, the FlS can be normalised for distance. While fluorescence imaging is not depth resolved, the correction of intensity loss over depth allows the FlS data to display changes in cell type independent of distance. Inversely, normalised FlS data can be overlaid on the OpUS image to provide supporting information on the biological makeup of the imaged tissue.

The work in this chapter details a preliminary investigation into the development of a dual-modal FlS-OpUS probe with a lateral field-of-view. Here, a proof-of-concept device was developed alongside an image acquisition and processing methodology. This was applied to a series of bespoke phantoms and the correspondence between the modalities was assessed.

5.2 Study I: Proof of Concept of Optical Fluorescence Sensing

While fluorescence imaging has been demonstrated for identifying malignant tissue previously, many methods require complex equipment and computationally-intensive results [220]. FlS, by comparison, provides a more straightforward and simplistic approach to detecting specific fluorophores. This method typically used miniaturised sensors that can be easily integrated into catheters, endoscopes, or other invasive tools, allowing for real-time, point-of-care diagnostics within confined areas of the body [221]. Furthermore, FlS generally requires less power and space, making it particularly suitable for miniaturised devices.

Here, a simple proof-of-concept of an all-optical FlS system was demonstrated using uncoated optical fibres connected to a US excitation source and a standard spectrometer, prior to combined US-FlS imaging. This was to be used as a ‘gold standard’ to compare with the FlS data acquired in subsequent studies.

5.2.1 Methods

Here, two 400 µm uncoated fibres were used (FG400LEP, Thorlabs, UK); one for excitation light delivery and one for transmission of the resulting FlS. Continuous wave excitation light was provided by a Ultraviolet (UV) Light Emitting Diode (LED) (MP365FP1, Thorlabs, USA). The emitted light excited a fluorescent response when incident on the target. This fluorescent response was received through the adjacent fibre and interrogated by a spectrometer (Maya2000 Pro, Ocean Optics, USA), using an integration time of 6 ms, which was the minimum time the spectrometer was capable of achieving.

The imaging target used here was a laser alignment disk (ADF9, Thorlabs, USA) with a known fluorescence emission of *ca.* $560-600$ nm. Contrast was added using a cable tidy in an X-shape (Fig. 5.3). The FlS probe was attached to a dual-axis translation stage and data was acquired in a grid formation through a step-by-step raster scan.

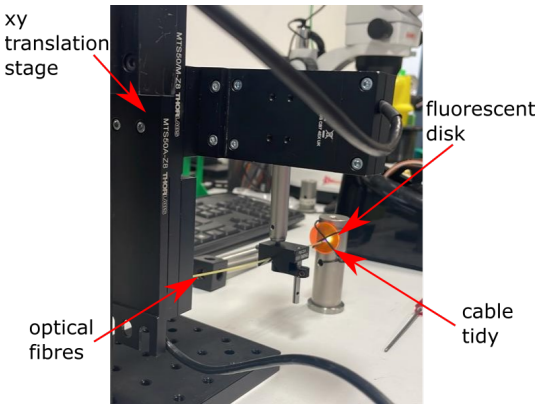

Figure 5.3: Photograph of fluorescence imaging process and imaging target.

For each fluorescence measurement, the optical spectrum was acquired across a range of $200-1200$ nm with a 0.5 nm bin size; this was the standard acquisition range for the spectrometer used. Here, the mean of the intensity I in the fluorescence response window ($\lambda_{min}-\lambda_{max}$) was calculated, given here to be $560-600$ nm. This was normalised using the maximum absorption value, which is typically given at the wavelength of the input excitation UV light:

$$I = \frac{\frac{I(\lambda_{min})+...+I(\lambda_{max})}{(\lambda_{max}-\lambda_{min})}}{I_{max}} \tag{5.1}$$

This results in the data being translated into matrix of intensity values for each acquisition point.

5.2.2 Results

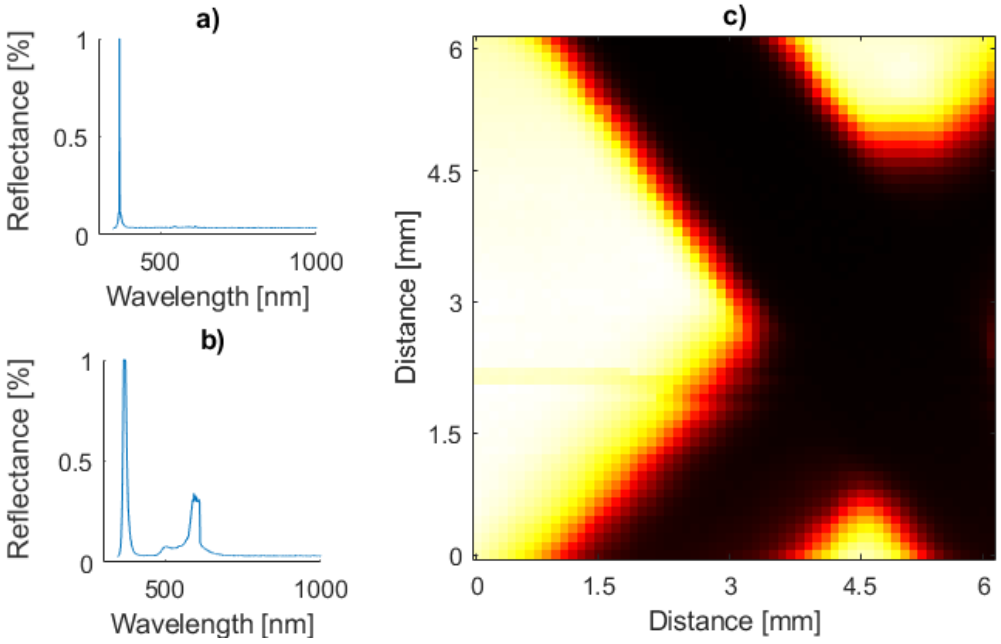

Figure 5.4: a) Light spectra at position [1,1]. b) Light spectra at position [61,61]. c) Reconstructed image of alignment disk fluorescence with contrast provided by cable tidy. Image corresponds to photograph in Fig. 5.3.

The resulting image is a 2D view of the imaging target. Here, the contrast was clearly visualised (Fig. 5.4c)), with a maximum SNR of 17 : 1. The excitation wavelength of 385 nm saturated the spectrometer, measuring 100% intensity (Fig. 5.4b)). No fluorescence signal was detected within the contrast region.

5.2.3 Discussion

The spectrometer used here is also used for characterising the optical profile of composite coatings in Chapter 3. In that context, additional measurements are taken for each study fibre to eliminate background light from the spectra. In particular, a 'dark' measurement is acquired to characterise any extraneous light, which is sub-

sequently detracted from the spectra. Here, it is not possible to incorporate these measurements during an imaging process. However, the saturation of the spectrometer caused by the excitation light creates a natural normalisation point. In this respect, the intensity of the received light is measured as relative to the intensity of the excitation light source, rather than as a photon count per second. This is not atypical; the intensity measured by a spectrometer is typically expressed in arbitrary units because the measurement depends on factors such as the sensitivity, the calibration, and the use of a known light source [222].

However, using a saturated signal for normalising fluorescence data has several limitations. Saturation prevents accurate measurement of true excitation intensity, leading to potential inaccuracies in normalisation. Many spectrometers exhibit non-linear responses near saturation, introducing errors, while variations in experimental conditions can cause inconsistencies. Additionally, normalisation based on a saturated signal may overcompensate fluorescence intensities, distorting the reconstructed image. Weaker fluorescence signals may be disproportionately affected, reducing the signal-to-noise ratio. A more reliable approach may involve using calibrated reference standards for improved accuracy, but this could introduce complexity when translating this approach to tissue imaging, particularly for clinical applications.

This normalisation dictated a SNR of $17:1$ in the region of $560-600$ nm. The SNR of commercial fluorescence sensing systems is typically $\geq 20:1$ [223, 28]. This indicates that, whilst demonstrating room for improvement, this method represents a good proof-of-concept for a simple FlS sensing system.

However, this probe requires modification to be compatible with the diameters required for a clinical endoscope in conjunction with the OpUS probe. The proposed modification is to use a single fibre for both transmission and receiving of light. This would minimise the diameter of the device, as well as ensure a consistent incidence of the excitation light to normalise the intensity of the received spectra.

5.3 Study II: Integration of Modalities

This study describes a proof-of-concept device, which demonstrates that fluorescence can be combined with OpUS in a miniature form factor. Here, the FlS device used in the previous study was modified to use a single fibre. This was used in conjunction with an OpUS probe to acquire images of a simple planar surface. The results acquired were used to develop an image coregistration process, including a FlS intensity depth-correction process based on an analytical model. Here, depth correction is applied to compensate for signal loss over depth, rather than to make the fluorescence depth-resolved.

5.3.1 Methods

5.3.1.1 Combined Imaging System

For this study, as imaging system was developed which comprised an OpUS imaging system and a fluorescence sensing system. Each comprised several components, as detailed in the following sections.

OpUS Imaging System

The OpUS imaging system used here is described previously in Chapters 3 and 4. Briefly, an OpUS transmitter was fabricated on a 400 μm optical fibre using a rGO-PDMS bilayer composite coating. This was used in conjunction with a planoconcave microresonator for US reception to create the OpUS probe (Fig. 5.5). The probe was used in a forward-viewing configuration as described in Chapter 3.

For US generation, pulsed excitation light (wavelength: 1064 nm, pulsewidth: 2 ns, pulse energy: 30 μJ) was delivered into the US transmitter from a Q-switched Nd:YAG laser (SPOT-10-500-1064, Elforlight, UK). The US receiving fibre was interrogated with a continuous wave light delivered by a tuneable laser (Tunics T100S-HP CL, Yenista Optics, France, tuning range: $1500 - 1630$ nm, power: 4.5 mW). As described previously, the low-frequency component of the received signal was digitised and used to record the FP transfer function and track the optimum bias point of the interferometer transfer function [224]. The high-frequency component was the US component originating from variations in the reflectivity of

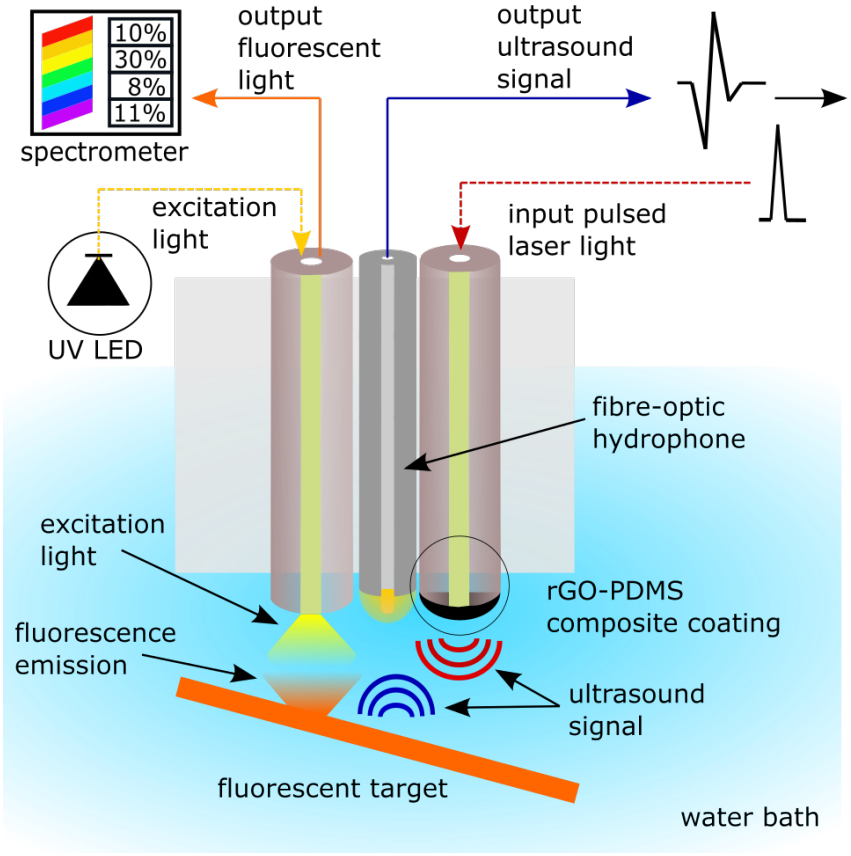

Figure 5.5: Schematic of fibre arrangement for a forward-viewing combined FlS-OpUS probe consisting of a fluorescence excitation/reception fibre, with UV input light (yellow) and spectrometer interrogation of the fluorescence emission (orange), and an OpUS probe, with input pulsed 1064 nm laser light generating US (red) through a composite rGO-PDMS coating and the reflected US (blue) being received by a fibre-optic hydrophone.

the FP cavity produced by the impinging US waves.

Fluorescence Sensing System

The FlS system comprised of a single uncoated 400 µm fibre (Fig. 5.5). A fibre splitter (TM200R5S1B, Thorlabs, USA) was used to facilitate both light emission and reception through a single fibre.

Continuous wave excitation light was provided by a UV LED (MP365FP1, Thorlabs, USA). The emitted light excited a fluorescent response when incident on the target. This fluorescent response was received through the same fibre emitting the excitation light and interrogated by a spectrometer (Maya2000 Pro, Ocean Optics, USA), using an integration time of 6 ms.

5.3.1.2 Data Acquisition

OpUS and FlS data were acquired concurrently during a single scan. Here, a step-by-step raster acquisition process was used, as described in Section 3.5. The proximal end of the probe was mounted on a translation stage (MTS50-Z8, Thorlabs, USA), which moved the probe a specified distance, paused during data acquisition, and then moved again. Data was acquired for both modalities at each point, which were concatenated for each modality to form a full dataset. Each US A-line consisted of 4000 data points which corresponded to a total imaging depth of *ca.* 30 mm. Each FlS measurement consisted of the intensity spectra across a range of $200-1200$ nm with a 0.5 nm bin size. The imaging target used here was a simple fluorescent slide angled at a 30° decline (FSK4, Thorlabs, USA) (Fig. 5.5). This provided a known target for use in verifying both the surface detection method and the modelling of fluorescence loss over depth. All experiments were carried out in a water bath and the imaging target was submerged and angled such that the imaging probe could acquire a top-down image (Fig. 5.5).

5.3.1.3 Image Processing

Ultrasound Post Processing

The US processing was carried out as described previously (Section 4.3.1.3) (Fig. 5.6a)). Briefly, the acquired A-lines were concatenated, followed by the application of a bandpass filter (Butterworth, 4th order, $1.5-40$ MHz) and a cross-talk removal algorithm as described in [177]. This was followed by the application of digital time-gain compensation [179]. The image was then reconstructed using the k-Wave toolbox [77, 225], using a k-space method based on the fast-Fourier transform. Finally, the signal envelope was found using the absolute value of the Hilbert transform followed by a log transformation.

Surface Detection

A surface detection method was implemented to identify the target surface and determine the position of the fluorescence signal within the image. In this approach, each A-line was analysed individually to detect the fluorescence signal. The process began by iterating through the A-line to identify the first pixel with an intensity

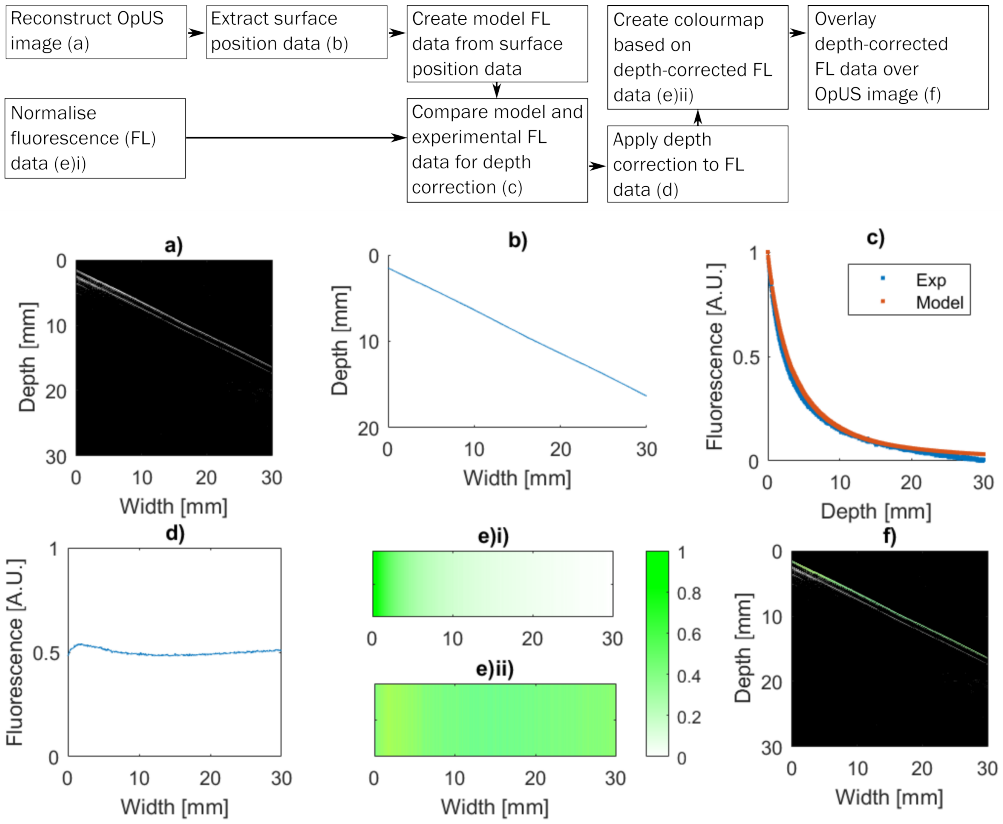

Figure 5.6: Image processing steps: a) Reconstructed OpUS image of target consisting of a slanted surface. b) Corresponding detected surface. c) Experimental data using the corresponding fluorescence measurements from the angled surface (blue) and modelled data using Equation 5.6 (orange) to show fluorescence intensity loss over depth. d) Fluorescence intensity corrected for depth over the width of the image. e) Fluorescence results i) before and ii) after depth correction is applied. f) OpUS image with fluorescence overlay.

value exceeding a predefined threshold. Once identified, the algorithm continued scanning to determine whether subsequent pixels also remained above the threshold. To mitigate the influence of noise, a minimum grouping of five consecutive pixels was required for detection. If a group contained fewer than five pixels above the threshold, it was disregarded, and the iteration proceeded to the next potential grouping. When a valid grouping of five or more pixels was detected, the index of the first pixel in this group was recorded for depth correction.

The fluorescence mask was then defined by continuing the iteration from this grouping until a pixel with a value below the threshold was encountered. This identified grouping was subsequently used to assign the fluorescence mask. If no

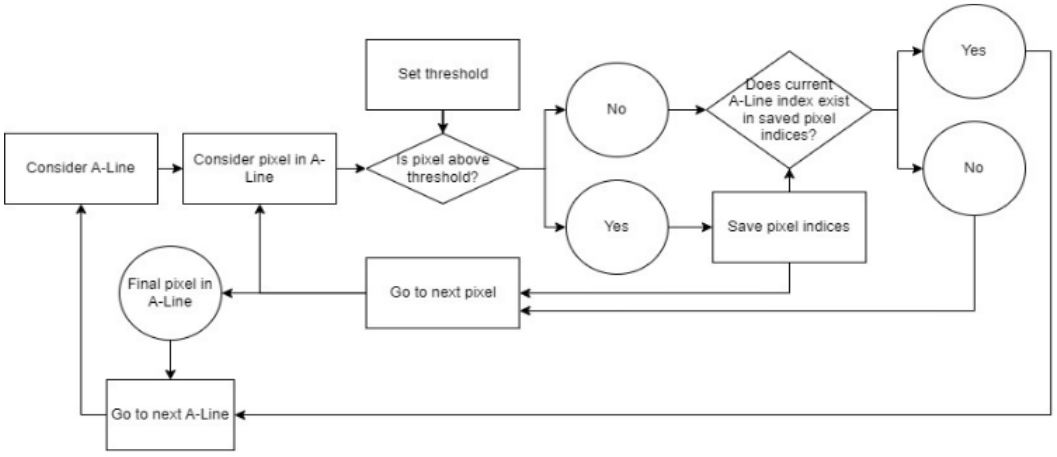

Figure 5.7: Schematic of steps taken for surface detection method.

grouping of at least five consecutive pixels above the threshold was found, the A-line was assigned a null fluorescence value.

Fluorescence Post Processing

The fluorescence signal obtained consists of a matrix of 2000 data points at each sensor location corresponding to the light intensity of the wavelength range. This was translated into a one dimensional series with a signal intensity value for each sensor location (Fig. 5.6e)i)). A fibre splitter was used to facilitate signal reception and provide a zero value for the fluorescence measurements. Received fluorescence intensity measurements were normalised against the saturation point provided by the excitation wavelength. The fluorescence emission window of the imaging target was found by comparing the entire dataset and locating the wavelengths where the light intensity fluctuates significantly. The fluorescence window of the imaging target here was found to be in the region of 470 - 520 nm. The average of this window was calculated for each sensor location resulting in the one dimensional data array.

Depth Correction

The depth correction process used an analytical fluorescence model as a function of depth. Assuming the light emission from the distal end of the fibre can be considered a point source, the radiated energy produces a spherical wave. Using the inverse-square law, the light intensity I as a function of distance x can be expressed as:

$$I \propto \frac{1}{x^2} \tag{5.2}$$

Applying the law of conservation of energy, the light intensity I from a power source P over an irradiated area A is given as:

$$I = \frac{P}{A} \tag{5.3}$$

Given the spherical wave, the irradiated area A is expressed as:

$$A = \pi r^2 \tag{5.4}$$

The point source consists of a 400 µm diameter fibre. Assuming that the absorption and scattering of the signal are negligible compared with the signal loss due to the acceptance angle of the optical fibre, the signal loss can be modelled. Given the Numerical Aperture (NA) of 0.22, the maximum acceptance angle θ_{acc} can be calculated as 12.71 °. The radius of the irradiated area can therefore be given as:

$$r = d_f + x\tan\theta_{acc} \tag{5.5}$$

This can be substituted into Equation 5.2 to give a modelled fluorescence loss as a function of depth as:

$$f(x) = \frac{1}{\pi(d_f + x\tan\theta_{acc})^2} \tag{5.6}$$

where d_f is the optical fibre diameter, θ_{acc} is the maximum acceptance angle of the optical fibre, and x is the depth given by the surface detection. The acquired fluorescent signal showing the loss of signal over depth can be seen in Fig.5.6c) alongside the modelled loss. This model was applied to the one dimensional array of fluorescence data in order to correct for signal loss over depth (Fig. 5.6d)).

Coregistration

The depth-corrected fluorescence was used to create a colourmap indicating the

magnitude of processed fluorescence (Fig.5.6e)ii)). This colourmap was applied as a mask using the surface location data and overlaid on the OpUS image (Fig.5.6f)).

5.3.2 Results

The analytical model was assessed using the slanted surface phantom. The experimental and modelled fluorescence loss for this target can be seen in Figure 5.6c). The difference is reported at 0.5% at both 0 and 15 mm. In contrast, at the maximum measured depth of 30 mm, the difference is 2.75%. On average, the difference across the depths is 1.5%.

The angled slide appeared as a slanted surface in the image (Fig. 5.6a)), which was used to assess the accuracy of the modelled loss. Here, the measured fluorescence signal decreased with depth following an inverse square pattern, with approximately 50% of the signal lost within the first 4 mm and 90% lost over 15 mm. The peak SNR was measured to be 15 : 1.

5.3.3 Discussion

Here, a hybrid device was demonstrated by imaging a simple planar surface with a known fluorescence emission window. This target was used to assess the bespoke surface detection and depth-correction methods developed.

The depth-correction was applied using a simple analytical model, which was based on the assumption that signal loss from the acceptance angle outweighs absorption and scattering. However, the model's accuracy diminished with increasing depth. Images were limited to a depth of 30 mm; between 20 and 30 mm, the signal drops to less than 10% of its original strength, and discrepancies between experimental and model values grow, likely leading to inaccurate correction factors. However, in the context of clinical imaging, the fluorescence emitted by targets like GI tissue typically originates near the surface, close to the imaging probe, where sensitivity is higher.

The required sensitivity for clinical conditions must be considered. Fluorescence intensity alone is not a reliable indicator; while it may be proportional to fluorophore concentration in low volumes, high concentrations can lead to concen-

tration quenching and fluorescence reabsorption [226]. For intensity to be proportional, factors such as specific excitation/emission wavelength pairs must be considered [227], along with corrections for the fraction of states and the fluorescence quantum yield of each state[228]. As such, creating a binary map of fluorescence presence may be more critical than achieving high sensitivity, though depth correction remains important.

The depth correction factor is determined based on the depth obtained through surface detection, using a simplified thresholding method to identify the single upper edge. However, this method has difficulty handling image noise, which increases the likelihood of detecting weak edges or misidentifying noise as an edge. This method could be replaced by edge detection algorithms like Canny or Sobel operators, but they tend to favour horizontal and vertical edges, making them unsuitable for tissue imaging, where edges are often irregular and curved [229]. These biases limit their effectiveness in accurately detecting the complex contours typical of biological tissues.

Due to the preliminary nature of this study, several limitations prevent this methodology from being directly applicable in a clinical setting. For instance, the analytical model assumes negligible scattering and absorption of fluorescence (FL) excitation light, whereas tissue imaging would experience significant optical losses. Additionally, a more sensitive and wavelength-selective fluorescence sensor would be required for endogenous imaging, where signal levels are typically lower. Other limitations include motion artefacts, which could impact image stability in a dynamic biological environment, and depth-dependent signal attenuation, which may require advanced correction techniques for accurate quantification. Furthermore, there is currently no method to account for interference from autofluorescence of surrounding tissues, which could interfere with signal specificity in a clinical scenario.

It is also of note that the acquisition time is not sufficient for clinical translation. This study used a step-by-step raster acquisition process acquired with a XY plane translation stage (MTS50-Z8, Thorlabs, USA). In development, the need

was realised for a continuous acquisition for seamless integration with the probe developed in Chapter 4. Here, the acquisition speed is limited by the integration time required by the spectrometer. This could be addressed by using an alternative detector such as APDs or PMTs, which demonstrate almost instantaneous acquisition. However, as discussed in Section 2.6.1.3, PMTs are difficult to integrate into compact systems due to their size, and APDs demonstrate a poor SNR.

5.4 Study III: Co-registered OpUS Imaging and FlS

The study outlined in Section 5.3 concluded that continuous acquisition was required in the development of this device for the required context. As such, a solution had to be found for acquiring spectra at known locations based on time intervals as opposed to distance intervals. For the OpUS probe, the pulse repetition rate can be dictated to acquire A-lines at set time intervals. Due to the constant movement speed of the motor, the location of these A-lines can be determined. However, this process is only possible due to the virtually instantaneous A-line acquisition; the error in position is negligible ($\pm$1.5 µm), and any possible errors are counteracted by the delay-and-sum image reconstruction process. As such, images can be reliably acquired at pullback speeds of 100 mm/s [36].

In comparison, the spectral acquisition is dictated by, and indeed qualitatively proportional to, the exposure time; a longer exposure time will result in a more precise measurement, especially when dealing with weak signals, as the increased light acquisition will enhance the SNR. The recommended exposure time for the MayaPro is 6 ms - 5 s. As such, applying the same approach as the OpUS modality of acquiring data at set time intervals is not as simple for FlS. Firstly, the movement speed is significantly limited. This is primarily due to the exposure time needing to be shorter than or equal to the step acquisition time. For example, using the minimum exposure time t of 6 ms and a step size d of 50 µm, the maximum speed is given as:

$$s = \frac{d}{t} = \frac{0.05}{0.006} = 8.33 mm/s \tag{5.7}$$

Secondly, the quality of the results will tend to decrease as the speed tends to the

maximum. Each measurement takes 6 ms to acquire, during which time the probe will have moved 50 μm if moving at the maximum velocity. As this speed requires the minimum possible exposure time, this is likely to correlate to a poorer result. Additionally, some time must be allowed for the computational process of acquiring the data at that point. As such, the continuous imaging speed for an A-line spacing of 50 μm was restricted to 7 mm/s. Dedicating the entire integration time to movement gives a step size of 42 μm per FlS acquisition. A scan length of 50 mm would be acquired here in 7.1 seconds.

This study demonstrates continuous multi-modal imaging in conjunction with a lateral-viewing probe. A range of bespoke phantoms were fabricated and imaged, with the modalities exhibited in coregistered images.

5.4.1 Methods

5.4.1.1 Imaging System

OpUS Probe

A modified transmitter was fabricated on a 400 μm optical fibre (FG400LEP, Thorlabs, USA) (Fig. 5.8a)i)). Firstly, the distal face of an optical fibre was polished to a 45°surface (Fig. 5.8a)ii)). Subsequently, a bilayer rGO-PDMS composite coating was manually applied to the polished surface (Fig. 5.8a)iii)), as described previously (Section 4.2). For US reception, a planoconcave microresonator was used in conjunction with the US transmitter (Fig. 5.8c)); this has been described previously [136] (Section 3.5).

OpUS Console

The console used was described in previous studies (Section 3.5, 4.3). Briefly, this comprised optoelectronic components to deliver pulsed excitation light to the OpUS transmitter and interrogate the OpUS receiver (Fig. 5.8d)). For US generation, pulsed excitation light (wavelength: 1064 nm, pulsewidth: 2 ns, pulse energy: 30 μJ) was delivered into the US transmitter from a Q-switched Nd:YAG laser (SPOT-10-500-1064, Elforlight, UK). The US receiving fibre was interrogated with a continuous wave light delivered by a tuneable laser (Tunics T100S-HP CL, Yenista Optics, France, tuning range: $1500 - 1630$ nm, power: 4.5 mW).

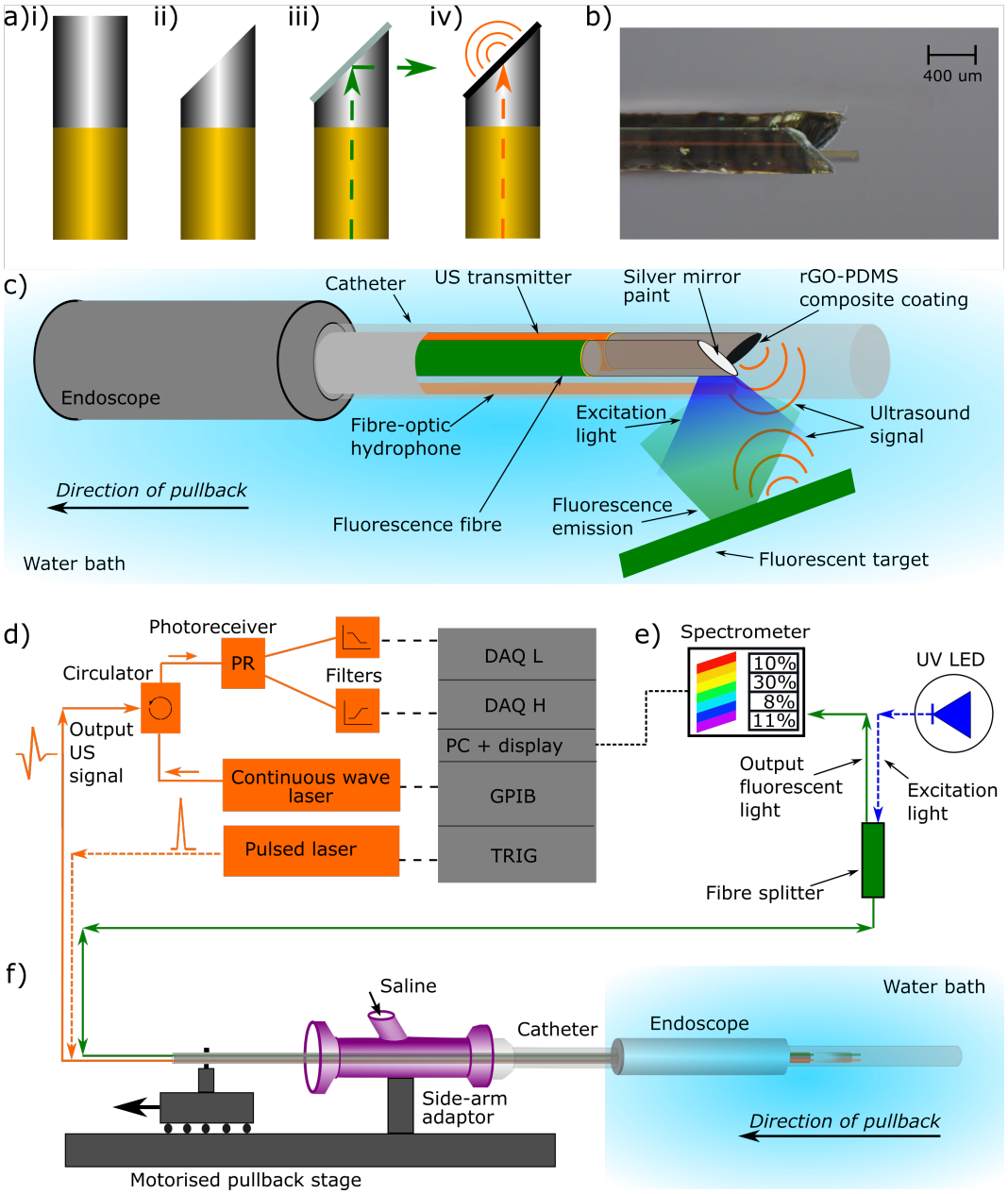

Figure 5.8: Schematic of combined OpUS-fluorescence probe. a)i) - iv) Transmitter fabrication process; i) stripped and cleaved optical fibre, ii) a fibre tip polished to 45° angle, iii) silver mirror applied to angled surface to create the fluorescence fibre, iv) OpUS-generating composite coating applied to angled surface to create the OpUS transmitter. b) Stereo-microscope image of probe tip showing 45° surfaces from the side view with scale bar. c) Schematic of the side-viewing optical transducer. US transmitting fibre and omnidirectional receiver (orange), combined with fluorescence transmission/reception fibre (green). Probe submerged in saline water bath and directed at the imaging target. d) Imaging console comprising pulsed excitation light delivered to the transmission fibre and CW light delivered from a wavelength-tuneable laser to the receiving fibre. e) Console comprising CW excitation light delivered by a UV LED and spectrometer for received fluorescence. f) Schematic of data acquisition process showing the transducer being pulled back within a stationary endoscope and catheter by the motorised stage.

Fluorescence Probe

The fluorescence sensing system comprised of a single uncoated 400 μm fibre. This was polished to create a 45°surface which was subsequently coated with silver mirror paint to create a side view (Fig. 5.8a)iv)). A fibre splitter (TM200R5S1B, Thorlabs, USA) was used to facilitate both light emission and reception through a single fibre (Fig. 5.8e)).

Fluorescence Console

Continuous wave excitation light was provided by an UV LED (MP365FP1, Thorlabs, USA) (Fig.5.8e)). The emitted light excited a fluorescent response when incident on the target. This fluorescent response was received through the same fibre emitting the excitation light and interrogated by a spectrometer (Maya2000 Pro, Ocean Optics, USA), using an integration time of 6 ms.

Imaging Probe

To facilitate medical application, the probe was incorporated within a medical grade catheter. An ultrasonically transparent sheath was adapted from an endobronchial guide sheath (K201 EBUS Sheath, Olympus, US). The three optical fibres were aligned longitudinally, with the US receiving fibre extended *ca.* 1 mm beyond the other two to facilitate the reception of US reflections (Fig. 5.8b),c)). The fibres were fixed in place within the tubing using sealing wax and heat shrink tubing, and the probe was then inserted into an US-transparent sheath (ID: 1.4 mm, OD: 1.6 mm) via a Y-piece connector which allowed flushing with water during experiments. For device delivery during experiments, a mock endoscope with an outer diameter of 5 mm and a 2 mm working channel was fabricated out of steel hypotubing to correspond with standard clinical gastrointestinal endoscopes; this has been described previously (Section 4.2.2.2). The catheter was inserted through the working channel of the mock endoscope for imaging.

5.4.1.2 Image Processing

Data Acquisition

OpUS imaging and fluorescence sensing was acquired concurrently during a single motorised pullback, which has been described previously (Section 4.5).

Briefly, the proximal end of the probe was mounted on a motorised translation stage (Fig. 5.8f)) (DDSM100, Thorlabs, UK, maximum speed: 500 mm/s, travel range: 100 mm) to provide pullback motion. The probe was clamped such that the Y-joint and sheath were held stationary while the probe was pulled back within the sheath (Fig. 5.8f)).

Data was acquired for both modalities at set intervals, equating to an acquisition step size of $50-240$ µm using speeds of $7-40$ mm/s to assess the attainable image quality during a clinically relevant imaging time-span. Each US A-line consisted of 4000 data points which corresponded to a total imaging depth of *ca.* 30 mm. For fluorescence measurement, the optical spectrum was acquired across a range of $200-1200$ nm with a 0.5 nm bin size. Each acquisition point was then concatenated and processed to form a full image.

Data Processing

The post-processing of the data has been outlined in Section 5.3.1.3. Briefly, the US image was reconstructed through the application of bandpass filters, cross-talk removal and TGC, before being reconstructed using the k-Wave toolbox. A surface detection method based on thresholding was applied to identify the target surface. This creates both a matrix of positional data and a mask for the fluorescence overlay. The fluorescence signal was translated to a 1D series with a signal intensity value for each sensor location. This was corrected for loss over depth by applying an analytical model in conjunction with the positional data acquired through surface detection. This corrected data was used to populate the mask acquired by the surface detection.

5.4.1.3 Imaging Targets

All experiments were carried out in a water bath and imaging targets were submersed and angled such that the imaging catheter could acquire a top-down image through rapid pullback acquisition (Fig. 5.8f)). Initial studies used a simple fluorescent slide angled at a 30° decline (FSK4, Thorlabs, USA) (Fig. 5.9a)i)). This provided a known target for use in verifying both the surface detection method and the modelling of fluorescence loss over depth in comparison with the configuration

demonstrated in the previous study.

To assess the correlation between the two modalities, a variety of phantoms were fabricated using a fluorescent filament (Polylite PLA, 3D Filaprint, UK) with a known excitation (385 nm) and fluorescent emission wavelength (470-520 nm). Firstly, a phantom was fabricated to assess the capabilities of the imaging probe. The phantom consisted of standalone posts (width: 1 mm) at decreasing heights with respect to the imaging path (Fig. 5.9a)iii)). An additional phantom was fabricated using the florescent filament comprising posts of decreasing widths (5 mm - 0.2 mm) to assess the positional accuracy of the fluorescent overlay (Fig. 5.9a)ii).

To produce clinically relevant images, a phantom was fabricated consisting of a segment of *ex vivo* porcine oesophagus (Medmeat, UK) with fluorescent inserts to simulate tissue contrasts. The tissue was acquired frozen, and subsequently defrosted and imaged immediately in a bath of saline solution. A 10 cm section of the oesophagus was mounted in a water bath with a mesh formed of fluorescent filament inserted inside (Fig. 5.10a)). Each section of mesh was 0.2 mm in diameter, and was aligned such that the mesh was in-line with the surface of the oesphageal tissue. The mock endoscope was inserted into the lumen, and the imaging probe was inserted through the instrument channel such that it extended out of the distal end into the oesophageal lumen.

5.4.2 Results

The lateral correlation of the two datasets was assessed using the known positions of the post phantoms. For instance, the horizontal distance from the starting position of the probe to the second post in Figure 5.9d) is given to be 7.2 mm, corresponding to a probe-target distance of 6 mm. At this point, the initial fluorescence signal was expected to appear in the 144^{th} measurement. In practise, the signal appeared in the 143^{rd} measurement and peaked at the 145^{th} measurement. This lateral correlation was repeated at faster imaging speeds of 40 mm/s, albeit with slightly less accuracy. Taking the same post, for example, the fluorescence signal was expected to appear at the 30^{th} measurement, but was not significantly apparent until the 31^{st} measurement in practise. However, this lateral correlation remained consistent across the entire

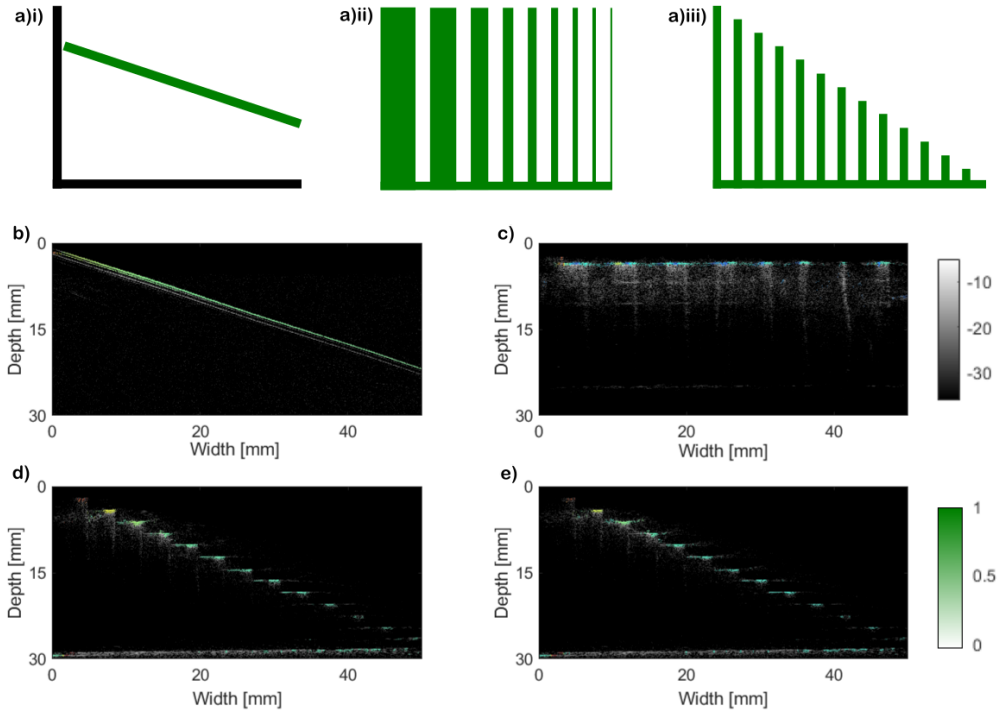

Figure 5.9: Co-registered fluorescent sensing-OpUS images of besoke phantoms. a)i) - iii) schematics of fabricated phantoms: i) slanted surface phantom, ii) stepped posts of decreasing widths, iii) stepped posts of decreasing height. b) - e) coregistered fluorescence-OpUS images displayed with a dynamic range of $-35:0$ dB of the phantoms shown in: b) part a)i), c) part a)ii), d) part a)iii) taken at 7 mm/s with a corresponding step of 50 µm. e) image d) repeated with an imaging speed of 40 mm/s and a corresponding step of 240 µm. Right: dB scale bar (top) and fluorescent contrast scale (bottom).

30 mm depth for both acquisition speeds.

Ex vivo swine oesophagus was imaged to investigate the clinical potential of the multi-modal probe and demonstrate its capability for gastrointestinal imaging (Fig. 5.10b)-c)). The full thickness of the oesophageal wall was visible in the US image; both the inner (green arrow) and outer (red arrow) surfaces appeared as distinct boundaries. The cork mount appeared in both images at a depth of approximately 10 mm (yellow arrow). The fluorescence overlay appeared in the surface layer of the tissue. The fluorescent inserts appeared as intermittent areas of variable sizes. This is to represent areas where the biomarkers of a particular fluorescence window are present. The opacity of the colour indicates the intensity of the fluorescence signal. The peak SNR here was measured at $14:1$

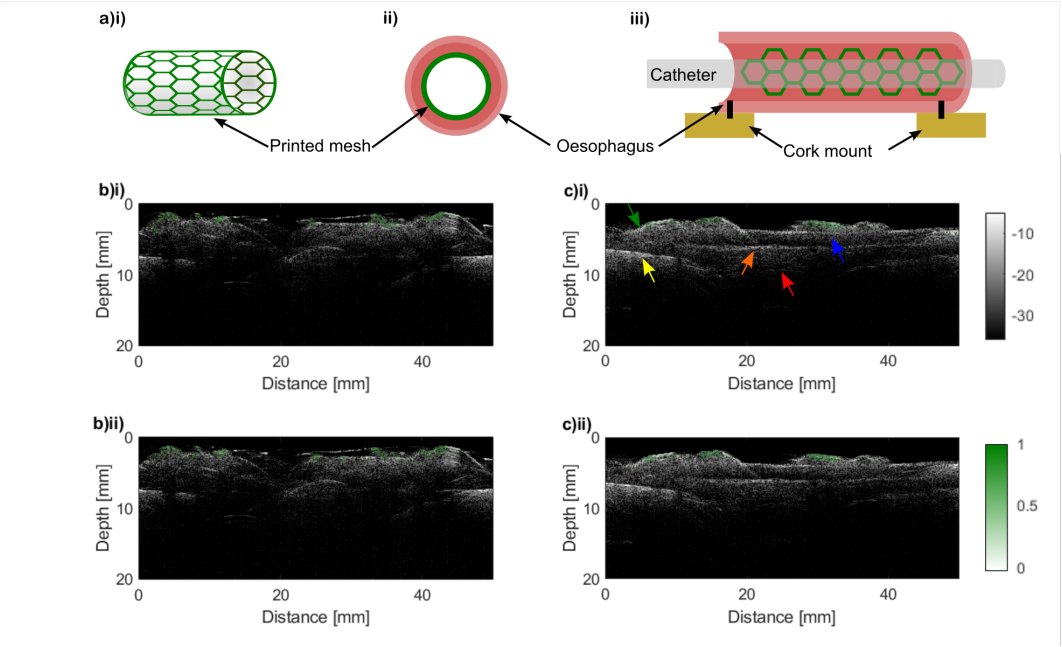

Figure 5.10: Overlaid fluorescence-OpUS images of *ex vivo* swine oesophageal tissue with fluorescent insert (a)i) - iii)) taken of two pieces of tissue (b)-c)) taken at speeds of 7 mm/s (b)i) and c)i)) and 40 mm/s (b)ii) and c)ii)). Right: dB scale bar (top) and fluorescent contrast scale (bottom). Part c)i) labels showing: cork mount (yellow), inner edge of tissue (green), outer edge of tissue (red), mucosa (orange) and submucosa with oesophageal glands (blue).

5.4.3 Discussion

As with the previous study, depth-correction was applied here using a simple analytical model, which was based on the assumption that signal loss from the acceptance angle outweighs absorption and scattering. This model was not altered for application to a lateral field-of-view. As noted in Section 5.3, the model's accuracy diminished with increasing depth. However, the accuracy of the model applied here was consistent with that of the previous study. In a clinical context, it may be more critical to obtain a binary map of fluorescence presence as opposed to a high accuracy of the received intensity.

To this end, this model was then applied to a series of phantoms with raised steps made from a material with a known fluorescing window. The results showed that the fluorescence signal aligned with the OpUS image within a single acquisition step, indicating strong linear alignment of the signals. However, at faster image

acquisition speeds, the quality of the US image declines due to the increased A-line spacing [36]. The lateral accuracy of the corresponding fluorescence data also declined. This could be due to either the reduced number of measurements leading to sampling errors, or the lower quality of the US image causing inaccuracies in the surface detection and therefore the fluorescence depth correction. In this case, the depth correction factor is determined based on the depth obtained through surface detection, using a simplified thresholding method to identify the single upper edge. However, this method has difficulty handling image noise, which increases the likelihood of detecting weak edges or misidentifying noise as an edge. This method could be replaced by edge detection algorithms like Canny or Sobel operators, but they tend to favor horizontal and vertical edges, making them unsuitable for tissue imaging, where edges are often irregular and curved [229]. These biases limit their effectiveness in accurately detecting the complex contours typical of biological tissues.

The full thickness of the *ex vivo* swine oesophageal tissue was resolved with clear tissue layers visible. The coregistered image demonstrated clinically relevant details, with the US data providing structural contrast and the FlS data providing complementary molecular specificity. In future work, the origin of the tissue boundaries indicated here could be verified through tissue histology or another reliable ground truth imaging technique. It is important to highlight that *in vivo* applications would depend on the tissue response, whether endogenous or exogenous, to indicate biomarkers such as dysplasia [10]. However, in this study, a fabricated insert was used to simulate abnormal tissue in a controlled manner to allow for validation. An additional development could involve using fluorescing dyes, such as Indocyanine Green (ICG), with *ex vivo* tissue to evaluate imaging quality. Alternatively, incorporating both inserts and dyes could showcase the probe's capability for multispectral FlS.

Previous studies have shown hybrid all-optical imaging using a wavelength-selective composite coating on a single optical fibre. However, this design likely compromises at least one imaging modality; [142] found that the developed

wavelength-selective composite had lower pressure and bandwidth compared to other available options. Here, using two fibres allows for optimal performance of both imaging modalities independently while still maintaining a clinically-compatible small diameter. Specifically, keeping fluorescence sensing as a separate component allows for greater adaptability. Previous studies have employed various excitation wavelengths to target different biomarkers [10, 230, 231]. By isolating the fluorescence element, the probe can potentially accommodate a broader range of tissue imaging needs with only a minimal increase in diameter.

It is important to note that the dual modality imaging technique here provides a slower imaging speed than that demonstrated previously (Section 4.5). This is in order to accommodate for both the processing time and the integration time required for each fluorescence acquisition. However, the maximum speed here of 40 mm/s is still capable of achieving > 5 s time-spans for image acquisition while maintaining competitive imaging resolutions. As stated previously, this faster acquisition speed correlates with a poorer imaging resolution and therefore accuracy of the fluorescence overlay; this is dictated by the minimum integration time of the spectrometer used for sensing. This issue could be addressed by using alternative detectors like PMTs, which offer high sensitivity and fast response times, making them well-suited for real-time applications [143]. However, PMTs are bulky and fragile, posing challenges for integration into compact systems, and they are also sensitive to magnetic fields, necessitating additional shielding [143]. Alternatively, APDs could serve as a durable, low-cost detector. While their lower sensitivity might limit use in applications requiring high precision, they would be adequate for generating a binary fluorescence map [143].

5.5 Chapter Conclusions

In this chapter, a novel hybrid all-optical imaging probe combing ultrasound imaging with complementary fluorescence sensing was demonstrated. Here, OpUS imaging provides structural contrast with imaging depths of up to 40 mm, whilst FlS can be used to differentiate tissue types thus providing complementary infor-

mation. The device comprised miniaturised components which are compatible with current clinical endoscopes and provided a view of the imaging target perpendicular to the fibre direction. The US transmitter generated a peak-to-peak pressure sufficient to enable US imaging with no averaging. Further, the bandwidth was suitable to generate a high imaging resolution [63]. Fluorescence sensing was performed using a single optical fibre, with US excitation light generating the fluorescence, which was then detected by a spectrometer.

A range of fluorescent phantoms were fabricated and imaged at speeds of $7-40$ mm/s to evaluate the capabilities of the probe. OpUS images and fluorescence data were co-registered and displayed as a single image. The quality of the co-registration was assessed at a variety of pullback speeds. To demonstrate the potential of the device for clinical imaging, an *ex vivo* swine oesophagus with fluorescent inserts was imaged with device delivery through the working channel of a mock endoscope.

Fundamentally, this work demonstrates that low-cost materials can be used to fabricate a hybrid, dual-modality imaging device, with modalities providing complementary information for one another. Additionally, the packaging of the probe in a clinically compatible catheter is a key step towards bringing fibre-optic hybrid probes through medical translation. It is expected that this device will be further developed for *in vivo* studies, with optimisation of both the available acquisition time and the handling for a preclinical environment. A further area of development for pre-clinical translation is to establish and test the appropriate light sources for targeting the endogenous fluorescence of various biomarkers. Additionally, this device demonstrates significant potential for multi-spectral FlS; this could be further developed.

Chapter 6

Conclusions

6.1 Initial Requirements

This thesis explores the development of a hybrid imaging tool for use in imaging the GI tract. During Chapter 1 a set of requirements was laid out for this device (Section 1.2). As stated, these requirements provided a guiding framework; as a proof-of-concept investigation, these were not expected to be fully met. However, several of these requirements have been met during the work.

- **Device diameter**. This was specified to be a suitably small diameter to fit within current surgical workflow. This requirement was not only met but exceeded; the device was successfully incorporated into a clinically compatible sheath, allowing it to pass through the working channel of a mock endoscope. This integration demonstrates the device's practical applicability in real-world clinical settings, highlighting its potential for use in minimally invasive procedures where space constraints and compatibility with existing surgical tools are critical. The successful adaptation within the mock endoscope setup underscores its readiness for translation into clinical environments.

- **Acquisition time**. Here, a target of less than one minute was set. Again, this target was exceeded. Subsecond acquisition times were achieved for OpUS imaging, without compromising image quality. When FlS was incorporated, the acquisition time was larger, but still $\leq$ 1 minute for a 50 mm scan.

- **Low cost**. This device is inherently designed to be single-use. While the

cost of the permanent elements such as the imaging consoles are significantly larger than this cost target, the cost of fabricating each probe meets this target.

- **Peak pressure**. Transmitters fabricated here generated pressures in excess of 1 MPa which is sufficient for the penetration depth required by the intended context of this device. This was demonstrated by the optimised Epolight-PDMS coatings in both of the transmitter configurations.

- **Bandwidth**. In particular, the broad bandwidths exhibited by the DD Epolight-PDMS coatings exceeded this requirement significantly. Bandwidths in excess of 30 MHz were recorded. This indicates the potential for a high-resolution OpUS imaging device.

- **Resolution**. In conjunction with the broad bandwidths, the resolutions here were significant. While the axial resolution was not specified as a target, values as low as 45 µm were recorded. The corresponding lateral resolution did not quite reach the intended target, recording an average of 120 µm. However, this is still a significant value, as this was acquired using a novel transmitter and novel acquisition method. Further optimisation could include modification of the transmitter to achieve a broader bandwidth and broader beam divergence in order to meet this resolution target.

- **Penetration depth**. This is directly related to the peak pressure generated by the transmitters. In this case, the high pressure caused the imaging penetration depth to surpass the intended target. Images were acquired of depths ≤ 40 mm. This successfully imaged through the *ex vivo* swine aorta and oesophageal tissue.

- **Fluorescence SNR**. This target was not quite met. The FlS sensing demonstrated a SNR of $17:1$. However, this is a significant value for a proof-of-concept device with no amplification or averaging and a minimal integration time. This could be improved by using alternative detectors such as APDs, or incorporating components such as lenses, mirrors or filters. However, dur-

ing the process of this investigation, it was theorised that a binary map of fluorescence presence may be a more clinically relevant approach.

- **Excitation/emission wavelengths**. This target was not met. Firstly, during the development of this probe, a known fluorescent target was deemed more suitable for validating the system and the image processing model. Secondly, addressing tissue autofluorescence would likely require *in vivo* imaging, which was not performed.

6.2 Discussion and Outlook

Over the course of this research there has been significant progress in the field of optical methods for biomedical imaging. Advancements in technologies such as OpUS, fluorescence spectroscopy, OCT, and photoacoustic imaging have enhanced the ability to visualise biological tissues with unprecedented resolution and specificity. Innovations in miniaturisation have allowed these techniques to be incorporated into compact, clinically compatible devices, broadening their applicability in minimally invasive procedures. Additionally, the integration of machine learning and advanced data processing algorithms has improved image reconstruction and analysis, providing clinicians with more accurate diagnostic information in real time. These developments have not only expanded the range of detectable biomarkers but also improved the speed, sensitivity, and overall performance of optical imaging methods, paving the way for new diagnostic and therapeutic possibilities in clinical practice.

The field of OpUS has advanced from bench-top and lab-based systems to imaging using a variety of probe configurations. In this work, B-mode pulse-echo imaging was successfully demonstrated in both forward- and lateral-viewing configurations, highlighting the potential of OpUS for medical imaging. Additionally, OpUS imaging was achieved with subsecond acquisition times without compromising image quality. This marks a significant advancement in translating this technology from the laboratory to clinical settings. The lateral-viewing configuration demonstrated here could provide clinicians with a clear view of the vessel wall,

which could act as a 'virtual biopsy'. This probe could be adapted to include rotational imaging similar to that demonstrated by [139], thus rapidly providing a complete view of the vessel. Further developments like this could create an invaluable clinical tool.

There has been significant work creating composite coatings which can generate high US pressures and bandwidths from several groups. For device development there are still many developments to be considered. Currently only a few studies have used materials which can both absorb and transmit light as a hybrid OpUS transmitter with complementary modalities [142, 3]. These materials are not as efficient as the best pure OpUS-generating materials such as carbon-based PDMS composites. Several new absorbers could be considered, such as Epolight 7665 (Epolin, UK) or quantum dots. The addition of a variety complementary modalities could be invaluable for clinicians, such as ablation, photoacoustic, or OCT. Overall, the future of all-optical imaging in medical contexts is likely to be very exciting with clinical translation in the near future.

Appendix A

Publications and Presentations

A.1 Publications

A.1.1 Journals

1. India Lewis-Thompson, Edward Z. Zhang, Paul C. Beard, Adrien E. Desjardins, and Richard J. Colchester. "All-optical ultrasound catheter for rapid B-mode oesophageal imaging." *Biomedical Optics Express* 14(8) (2023): 4052-4064.

2. Bodian, Semyon, Esra Aytac-Kipergil, Shaoyan Zhang, India Lewis-Thompson, Sanjayan Sathasivam, Sunish J. Mathews, Erwin J. Alles et al. "Comparison of Fabrication Methods for Fiber-Optic Ultrasound Transmitters Using Candle-Soot Nanoparticles." *Advanced Materials Interfaces* 10(9) (2023): 2201792.

A.1.2 Conference Proceedings

1. India Lewis-Thompson, Shaoyan Zhang, Sacha Noimark, Adrien E Desjardins, and Richard J Colchester. PDMS composites with photostable NIR dyes for multi-modal ultrasound imaging. MRS Advances, 7(23-24):499–503, 2022

2. India Lewis-Thompson, Sunish Mathews, Edward Zhang, Paul Beard, Adrien Desjardins, and Richard Colchester. PDMS composites with photostable NIR

dyes for B-mode ultrasound imaging. In 2022 IEEE International Ultrasonics Symposium (IUS), pages 1–5. IEEE, 2022

A.2 Conference Presentations

1. PDMS composites with photostable NIR dyes for B-mode ultrasound imaging. 2022 IEEE International Ultrasonics Symposium (IUS), Venice.

2. PDMS composites with photostable NIR dyes for B-mode ultrasound imaging. 2022 Biomedical Engineering, London.

Appendix B

Bespoke MATLAB Functions for Image Co-Registration

B.1 Surface Detection

Listing B.1: Surface detection algorithm for use on a two-dimensional OpUS image to find create a mask of the surface detected (peakPos) and a one dimensional array of the distance of the surface from the imaging probe (depth).

```
function [peakPos, depth] = findsurface(dataset,
   threshold,visibility)

[data_rows, data_cols] = size(dataset);
peakPos = zeros(data_rows, data_cols);

for col = 1:data_cols
    peakFound = false;
    for row = threshold + 1:data_rows
        if dataset(row, col) > threshold
            peakPos(row:row + visibility, col) = 1;
            peakFound = true;
        elseif peakFound
            break;
```

```
        end
    end
end

depth = zeros(1, size(peakPos, 2));
for col = 1:size(peakPos, 2)
    row_index = find(peakPos(:, col), 1, 'first');
    if ~isempty(row_index)
        depth(col) = row_index;
    end
end
```

B.2 Fluorescence Correction

Listing B.2: Fluorescence intensity correction outputting the correction factor based on the depth data given by the surface detection algorithm.

```
function model_values = FL_depth_correction(depth)
alpha = 12.71;  %in degrees
fdiameter = 0.4;    %fibre core diameter in mm
model_values = 1./(pi*(fdiameter+(depth*tan(deg2rad(
   alpha)))).^2);
```

B.3 Creating a Fluorescence Colormap

Listing B.3: Fluorescence image creation based on the corrected fluorescence data.

```
function FL_image = createFLcmap(FL, cmap)
norm = imagesc(FL, [0 1]); % Create scaled colourmap
colormap(cmap);
cdata = norm.CData; % Colourmap data
cmap = colormap(norm.Parent);
num = size(cmap, 1); % Number of colours in colourmap
```

```
7  c = linspace(norm.Parent.CLim(1), norm.Parent.CLim(2),
       num); % Intensity range
8  idx = reshape(interp1(c, 1:num, cdata(:), 'nearest'),
       size(cdata)); % Indexed image
9  FL_image = ind2rgb(idx, cmap);
10 close(norm)
```

Bibliography

[1] S Zeki and RC Fitzgerald. Targeting care in Barrett's Oesophagus. *Clinical Medicine*, 14(Suppl 6):s78–s83, 2014.

[2] A Fritscher-Ravens, D Schuppan, M Ellrichmann, S Schoch, C Röcken, J Brasch, J Bethge, M Böttner, J Klose, and PJ Milla. Confocal endomicroscopy shows food-associated changes in the intestinal mucosa of patients with irritable bowel syndrome. *Gastroenterology*, 147(5):1012–1020, 2014.

[3] S Noimark, RJ Colchester, RK Poduval, E Maneas, EJ Alles, T Zhao, EZ Zhang, M Ashworth, E Tsolaki, AH Chester, et al. Polydimethylsiloxane composites for optical ultrasound generation and multimodality imaging. *Advanced Functional Materials*, 28(9):1704919, 2018.

[4] L Shi, LA Sordillo, A Rodríguez-Contreras, and R Alfano. Transmission in near-infrared optical windows for deep brain imaging. *Journal of Biophotonics*, 9(1-2):38–43, 2016.

[5] I Lewis-Thompson, S Zhang, S Noimark, AE Desjardins, and RJ Colchester. PDMS composites with photostable NIR dyes for multi-modal ultrasound imaging. *MRS Advances*, 7(23-24):499–503, 2022.

[6] M Monici. Cell and tissue autofluorescence research and diagnostic applications. *Biotechnology annual review*, 11:227–256, 2005.

[7] M Gandolfi, F Banfi, and C Glorieux. Optical wavelength dependence of photoacoustic signal of gold nanofluid. *Photoacoustics*, 20:100199, 2020.

[8] MZ Lin, MR McKeown, HL Ng, TA Aguilera, NC Shaner, RE Campbell, SR Adams, LA Gross, W Ma, T Alber, et al. Autofluorescent proteins with excitation in the optical window for intravital imaging in mammals. *Chemistry & biology*, 16(11):1169–1179, 2009.

[9] SS Zakariyah, PP Conway, DA Hutt, DR Selviah, K Wang, J Rygate, J Calver, and W Kandulski. Fabrication of polymer waveguides by laser ablation using a 355 nm wavelength Nd: YAG laser. *Journal of Lightwave Technology*, 29(23):3566–3576, 2011.

[10] AC Croce and G Bottiroli. Autofluorescence spectroscopy and imaging: a tool for biomedical research and diagnosis. *European journal of histochemistry: EJH*, 58(4), 2014.

[11] M Panjehpour, BF Overholt, T Vo-Dinh, RC Haggitt, DH Edwards, and FP Buckley. Endoscopic fluorescence detection of high-grade dysplasia in Barrett's Oesophagus. *Gastroenterology*, 111(1):93–101, 1996.

[12] S Basu, S Singhal, and D Singh. A systematic literature review on multimodal medical image fusion. *Multimedia tools and applications*, 83(6):15845–15913, 2024.

[13] GJ Cook et al. PET/CT in oncology. *Clinical medicine*, 12(4):368, 2012.

[14] JH Kempen, EA Sugar, GJ Jaffe, NR Acharya, JP Dunn, SG Elner, SL Lightman, JE Thorne, AT Vitale, MM Altaweel, et al. Fluorescein angiography versus optical coherence tomography for diagnosis of uveitic macular edema. *Ophthalmology*, 120(9):1852–1859, 2013.

[15] NHS UK. Case-mix Adjusted Percentage of Cancers Diagnosed at Stages 1 and 2 in England, 2020. *https://digital.nhs.uk/data-and-information/publications/statistical/case-mix-adjusted-percentage-of-cancers-diagnosed-at-stages-1-and-2-in-england* [Accessed 07-12-2023].

[16] CQ Liu, YL Ma, Q Qin, PH Wang, Y Luo, PF Xu, and Y Cui. Epidemiology of esophageal cancer in 2020 and projections to 2030 and 2040. *Thoracic Cancer*, 14(1):3–11, 2023.

[17] TM Runge, JA Abrams, and NJ Shaheen. Epidemiology of Barrett's Oesophagus and esophageal adenocarcinoma. *Gastroenterology Clinics*, 44(2):203–231, 2015.

[18] C Richardson, P Colavita, C Dunst, J Bagnato, P Billing, K Birkenhagen, F Buckley, W Buitrago, J Burnette, P Leggett, et al. Real-time diagnosis of Barrett's Oesophagus: a prospective, multicenter study comparing confocal laser endomicroscopy with conventional histology for the identification of intestinal metaplasia in new users. *Surgical endoscopy*, 33:1585–1591, 2019.

[19] RJ Schlemper, RH Riddell, Y e al Kato, F Borchard, HS Cooper, SM Dawsey, MF Dixon, CM Fenoglio-Preiser, JF Fléjou, Karel Geboes, et al. The Vienna classification of gastrointestinal epithelial neoplasia. *Gut*, 47(2):251–255, 2000.

[20] RD Odze. Diagnosis and grading of dysplasia in Barrett's Oesophagus. *Journal of clinical pathology*, 59(10):1029–1038, 2006.

[21] ME Singer and RD Odze. High rate of missed Barrett's Oesophagus when screening with forceps biopsies. *Esophagus*, 20(1):143–149, 2023.

[22] National Institute for Health and Care Excellence. Cytosponge for detecting abnormal cells in the oesophagus [medtech innovation briefing], 2020. *https://www.nice.org.uk/guidance/mib240*.

[23] W Januszewicz, WK Tan, K Lehovsky, I Debiram-Beecham, T Nuckcheddy, S Moist, S Kadri, M di Pietro, A Boussioutas, NJ Shaheen, et al. Safety and acceptability of a non-endoscopic esophageal sampling device–Cytosponge®: a systematic review of multi-center data. *Clinical gastroenterology and hepatology: the official clinical practice journal of the American Gastroenterological Association*, 17(4):647, 2019.

[24] SS Sami, V Subramanian, WM Butt, G Bejkar, J Coleman, J Mannath, and K Ragunath. High definition versus standard definition white light endoscopy for detecting dysplasia in patients with Barrett's Oesophagus. *Diseases of the Esophagus*, 28(8):742–749, 2015.

[25] WL Hofstetter, RE Davila, and ML Davila. Chapter 37: Endoscopic management of high-grade dysplasia and superficial esophageal carcinoma. In *Shackelford's Surgery of the Alimentary Tract, 2 Volume Set*, pages 382–390. Elsevier, 2019.

[26] SB Andersen, I Taghavi, SB Søgaard, CAV Hoyos, MB Nielsen, JA Jensen, and CM Sørensen. Super-resolution ultrasound imaging can quantify alterations in microbubble velocities in the renal vasculature of rats. *Diagnostics*, 12(5):1111, 2022.

[27] SR Puli, JBK Reddy, ML Bechtold, D Antillon, JA Ibdah, and MR Antillon. Staging accuracy of esophageal cancer by endoscopic ultrasound: a meta-analysis and systematic review. *World journal of gastroenterology: WJG*, 14(10):1479, 2008.

[28] S Yoon, SY Cheon, S Park, D Lee, Y Lee, S Han, M Kim, and H Koo. Recent advances in optical imaging through deep tissue: imaging probes and techniques. *Biomaterials Research*, 26(1):57, 2022.

[29] P Hinnen, FWM de Rooij, EM Terlouw, A Edixhoven, H Van Dekken, R Van Hillegersberg, HW Tilanus, JHP Wilson, and PD Siersema. Porphyrin biosynthesis in human Barrett's Oesophagus and adenocarcinoma after ingestion of 5-aminolaevulinic acid. *British journal of cancer*, 83(4):539–543, 2000.

[30] B Aasling, J Jirholt, P Hammond, M Knutsson, A Walentinsson, G Davidson, L Agreus, A Lehmann, and M Lagerstrom-Fermer. Collagen type III alpha I is a gastro-oesophageal reflux disease susceptibility gene and a male risk factor for hiatus hernia. *Gut*, 58(8):1063–1069, 2009.

[31] National Institute of Diabetes, Digestive, and Kidney Diseases. Upper gi endoscopy. *https://www.niddk.nih.gov/health-information/diagnostic-tests/upper-gi-endoscopy?* [Online; accessed 15 December 2023].

[32] DF Swinehart. The Beer-Lambert law. *Journal of chemical education*, 39(7):333, 1962.

[33] Michael F Byrne and Paul S Jowell. Gastrointestinal imaging: endoscopic ultrasound. *Gastroenterology*, 122(6):1631–1648, 2002.

[34] KN Phoa, FG Van Vilsteren, BL Weusten, R Bisschops, EJ Schoon, K Ragunath, G Fullarton, M Di Pietro, N Ravi, M Visser, et al. Radiofrequency ablation vs endoscopic surveillance for patients with Barretts Esophagus and low-grade dysplasia: a randomized clinical trial. *Jama*, 311(12):1209–1217, 2014.

[35] I Lewis-Thompson, S Mathews, E Zhang, P Beard, A Desjardins, and R Colchester. PDMS composites with photostable NIR dyes for b-mode ultrasound imaging. In *2022 IEEE International Ultrasonics Symposium (IUS)*, pages 1–5. IEEE, 2022.

[36] I Lewis-Thompson, EZ Zhang, PC Beard, AE Desjardins, and RJ Colchester. All-optical ultrasound catheter for rapid B-mode oesophageal imaging. *Biomedical Optics Express*, 14(8):4052–4064, 2023.

[37] S Thakkar and V Kaul. Endoscopic ultrasound staging of esophageal cancer. *Gastroenterology & Hepatology*, 16(1):14, 2020.

[38] W Curvers, L Baak, R Kiesslich, A Van Oijen, T Rabenstein, K Ragunath, JF Rey, P Scholten, U Seitz, F Ten Kate, et al. Chromoendoscopy and narrow-band imaging compared with high-resolution magnification endoscopy in Barrett's Oesophagus. *Gastroenterology*, 134(3):670–679, 2008.

[39] JM Poneros and NS Nishioka. Diagnosis of Barrett's Oesophagus using optical coherence tomography. *Gastrointestinal Endoscopy Clinics*, 13(2):309–323, 2003.

[40] JM Poneros. Diagnosis of Barrett's Oesophagus using optical coherence tomography. *Gastrointestinal Endoscopy Clinics*, 14(3):573–588, 2004.

[41] K Uno, T Koike, and T Shimosegawa. Recent development of optical coherence tomography for preoperative diagnosis of esophageal malignancies. *World journal of gastrointestinal endoscopy*, 7(9):872, 2015.

[42] N Gupta, R Yelamanchi, H Agrawal, and N Agarwal. Role of optical coherence tomography in Barrett's Oesophagus. *Artificial Intelligence in Gastrointestinal Endoscopy*, 2(4):149–156, 2021.

[43] DR Kohli, ML Schubert, AM Zfass, and TU Shah. Performance characteristics of optical coherence tomography in assessment of Barrett's Oesophagus and esophageal cancer: systematic review. *Diseases of the Esophagus*, 30(11), 2017.

[44] TH Tsai, CL Leggett, AJ Trindade, A Sethi, AF Swager, V Joshi, JJ Bergman, H Mashimo, NS Nishioka, and E Namati. Optical coherence tomography in gastroenterology: a review and future outlook. *Journal of biomedical optics*, 22(12):121716–121716, 2017.

[45] JF Bruzzi, RF Munden, MT Truong, EM Marom, BS Sabloff, GW Gladish, RB Iyer, TS Pan, HA Macapinlac, and JJ Erasmus. PET/CT of esophageal cancer: its role in clinical management. *Radiographics*, 27(6):1635–1652, 2007.

[46] HY Fang, NS Munch, M Schottelius, J Ingermann, H Liu, M Schauer, S Stangl, G Multhoff, K Steiger, C Gerngroß, et al. CXCR4 is a potential target for diagnostic PET/CT imaging in Barrett's dysplasia and esophageal adenocarcinoma. *Clinical Cancer Research*, 24(5):1048–1061, 2018.

[47] J Lu, X Sun, X Yang, X Tang, Q Qin, H Zhu, H Cheng, and X Sun. Impact of PET/CT on radiation treatment in patients with esophageal cancer: a systematic review. *Critical reviews in oncology/hematology*, 107:128–137, 2016.

[48] HH Chuang and HA Macapinlac. The evolving role of PET-CT in the management of esophageal cancer. *The Quarterly Journal of Nuclear Medicine and Molecular Imaging*, 53(2):201, 2009.

[49] S Bhushan, R Richards-Kortum, and S Anandasabapathy. Progress and challenges of global high-resolution endoscopy. *Int. Arch. Intern. Med*, 4(024):10–23937, 2020.

[50] JS Louie, R Richards-Kortum, and S Anandasabapathy. Applications and advancements in the use of high-resolution microendoscopy for detection of gastrointestinal neoplasia. *Clinical Gastroenterology and Hepatology*, 12(11):1789–1792, 2014.

[51] RS Gill and R Singh. Endoscopic imaging in Barrett's Oesophagus: current practice and future applications. *Annals of Gastroenterology*, 25(2):89, 2012.

[52] WL Curvers, FJC van den Broek, JB Reitsma, E Dekker, and JJGHM Bergman. Systematic review of narrow-band imaging for the detection and differentiation of abnormalities in the esophagus and stomach (with video). *Gastrointestinal endoscopy*, 69(2):307–317, 2009.

[53] Y Hamamoto, T Endo, K Nosho, Y Arimura, M Sato, and K Imai. Usefulness of narrow-band imaging endoscopy for diagnosis of Barrett's Oesophagus. *Journal of gastroenterology*, 39:14–20, 2004.

[54] R Singh, SC Mei, and S Sethi. Advanced endoscopic imaging in Barrett's Oesophagus: a review on current practice. *World journal of gastroenterology: WJG*, 17(38):4271, 2011.

[55] RS DaCosta, BC Wilson, and NE Marcon. Spectroscopy and fluorescence in esophageal diseases. *Best Practice & Research Clinical Gastroenterology*, 20(1):41–57, 2006.

[56] H Isomoto, A Nanashima, T Senoo, K Ogiwara, M Hashisako, K Ohnita, N Yamaguchi, M Kunizaki, S Hidaka, H Fukuda, et al. In vivo fluorescence navigation of gastric and upper gastrointestinal tumors by 5-aminolevulinic acid mediated photodynamic diagnosis with a laser-equipped video image endoscope. *Photodiagnosis and Photodynamic Therapy*, 12(2):201–208, 2015.

[57] MB Sturm and TD Wang. Emerging optical methods for surveillance of Barrett's Oesophagus. *Gut*, 64(11):1816–1823, 2015.

[58] J Mannath and K Ragunath. Role of endoscopy in early oesophageal cancer. *Nature reviews Gastroenterology & hepatology*, 13(12):720–730, 2016.

[59] SR Friedberg and J Lachter. Endoscopic ultrasound: Current roles and future directions. *World Journal of Gastrointestinal Endoscopy*, 9(10):499, 2017.

[60] MM Owens and MB Kimmey. The role of endoscopic ultrasound in the diagnosis and management of Barrett's Oesophagus. *Gastrointestinal Endoscopy Clinics*, 13(2):325–334, 2003.

[61] H Lu, H Cui, G Lu, L Jiang, R Hensleigh, Y Zeng, A Rayes, MK Panduranga, M Acharya, Z Wang, et al. 3d printing and processing of miniaturized transducers with near-pristine piezoelectric ceramics for localized cavitation. *Nature communications*, 14(1):2418, 2023.

[62] SK Kirk et al. Recent advancements in ultrasound transducer: from material strategies to biomedical applications. *BME frontiers*, 2022.

[63] A Ng and J Swanevelder. Resolution in ultrasound imaging. *Continuing Education in Anaesthesia Critical Care & Pain*, 11(5):186–192, 2011.

[64] A Rosencwaig and A Gersho. Theory of the photoacoustic effect with solids. *Journal of Applied Physics*, 47(1):64–69, 1976.

[65] H Hu, X Wang, and X Xu. Generalized theory of the photoacoustic effect in a multilayer material. *Journal of Applied Physics*, 86(7):3953–3958, 1999.

[66] Lihong V Wang and Hsin-i Wu. *Biomedical optics: principles and imaging*. John Wiley & Sons, 2007.

[67] P Beard. Biomedical photoacoustic imaging. *Interface Focus*, 1(4):602–631, 2011.

[68] AL McKenzie. Physics of thermal processes in laser-tissue interaction. *Physics in Medicine & Biology*, 35(9):1175, 1990.

[69] M Xu and LV Wang. Photoacoustic imaging in biomedicine. *Review of Scientific Instruments*, 77(4):041101, 2006.

[70] LV Wang and H Wu. *Biomedical optics: principles and imaging*. John Wiley & Sons, 2012.

[71] FJ Millero, RW Curry, and W Drost-Hansen. Isothermal compressibility of water at various temperatures. *Journal of Chemical and Engineering Data*, 14(4):422–425, 1969.

[72] LI Rugani. Relationship of temperature rise to incident laser power in optical traps. *Photonics Spectra*, 41(4):104, 2007.

[73] T Stahl, T Allen, and P Beard. Characterization of the thermalisation efficiency and photostability of photoacoustic contrast agents. In *Photons Plus Ultrasound: Imaging and Sensing 2014*, volume 8943, page 89435H. International Society for Optics and Photonics, 2014.

[74] E Grüneisen. Theorie des festen zustandes einatomiger elemente. *Annalen der Physik*, 344(12):257–306, 1912.

[75] SA Goss, RL Johnston, and F Dunn. Comprehensive compilation of empirical ultrasonic properties of mammalian tissues. *The Journal of the Acoustical Society of America*, 64(2):423–457, 1978.

[76] D Carugo, J Owen, C Crake, JY Lee, and E Stride. Biologically and acoustically compatible chamber for studying ultrasound-mediated delivery of therapeutic compounds. *Ultrasound in Medicine & Biology*, 41(7):1927–1937, 2015.

[77] BE Treeby and BT Cox. k-Wave: MATLAB toolbox for the simulation and reconstruction of photoacoustic wave fields. *Journal of Biomedical Optics*, 15(2):021314, 2010.

[78] G Barton. *Elements of Green's functions and propagation: potentials, diffusion, and waves*. Oxford University Press, 1989.

[79] WY Chang, W Huang, J Kim, S Li, and X Jiang. Candle soot nanoparticles-polydimethylsiloxane composites for laser ultrasound transducers. *Applied Physics Letters*, 107(16):161903, 2015.

[80] S Umchid. Directivity pattern measurement of ultrasound transducers. *The International Journal on Applied Biomedical Engineering (IJABME)*, 2:39–43, 2009.

[81] LE Kinsler, AR Frey, AB Coppens, and JV Sanders. *Fundamentals of acoustics*. John wiley & sons, 2000.

[82] FC Laing and AB Kurtz. The importance of ultrasonic side-lobe artifacts. *Radiology*, 145(3):763–768, 1982.

[83] B Mandersson and G Salomonsson. Weighted least-squares pulse-shaping filters with application to ultrasonic signals. *IEEE transactions on ultrasonics, ferroelectrics, and frequency control*, 36(1):109–113, 1989.

[84] W Yaping, S Dufang, and H Yulong. Study of the directivity of laser generated ultrasound in solids. *Journal of applied physics*, 83(3):1207–1212, 1998.

[85] C Ni, L Dong, Z Shen, X Ni, and D Shi. Numerical simulation study of defect detections by using laser array generated giant acoustic waves. *International Journal of Thermophysics*, 36:1236–1243, 2015.

[86] E Biagi, M Brenci, S Fontani, L Masotti, and M Pieraccini. Photoacoustic generation: Optical fiber ultrasonic sources for non destructive evaluation and clinical diagnosis. *Optical review*, 4(4):481–483, 1997.

[87] E Biagi, F Margheri, and D Menichelli. Efficient laser-ultrasound generation by using heavily absorbing films as targets. *ieee transactions on ultrasonics, ferroelectrics, and frequency control*, 48(6):1669–1680, 2001.

[88] E Biagi, S Cerbai, L Masotti, L Belsito, A Roncaglia, G Masetti, and N Speciale. MOMS technology for fully fiber optic ultrasonic probes: a proposal for virtual biopsy. In *Sensors*, pages 1156–1160. IEEE, 2010.

[89] GJ Diebold, T Sun, and MI Khan. Photoacoustic monopole radiation in one, two, and three dimensions. *Physical Review Letters*, 67(24):3384, 1991.

[90] EJ Alles, J Heo, S Noimark, RJ Colchester, IP Parkin, HW Baac, and AE Desjardins. Acoustical characterisation of carbon nanotube-loaded polydimethylsiloxane used for optical ultrasound generation. In *2017 IEEE International Ultrasonics Symposium (IUS)*, pages 1–4. IEEE, 2017.

[91] BE Treeby, EZ Zhang, AS Thomas, and BT Cox. Measurement of the ultrasound attenuation and dispersion in whole human blood and its components from 0–70 MHz. *Ultrasound in Medicine & Biology*, 37(2):289–300, 2011.

[92] HW Baac, JG Ok, T Lee, and LJ Guo. Nano-structural characteristics of carbon nanotube–polymer composite films for high-amplitude optoacoustic generation. *Nanoscale*, 7(34):14460–14468, 2015.

[93] N Bowden, WTS Huck, KE Paul, and GM Whitesides. The controlled formation of ordered, sinusoidal structures by plasma oxidation of an elastomeric polymer. *Applied Physics Letters*, 75(17):2557–2559, 1999.

[94] M Born and E Wolf. *Principles of optics: electromagnetic theory of propagation, interference and diffraction of light*. Elsevier, 1999.

[95] Z Cai, W Qiu, G Shao, and W Wang. A new fabrication method for all-PDMS waveguides. *Sensors and Actuators A: Physical*, 204:44–47, 2013.

[96] SL Chen. Review of laser-generated ultrasound transmitters and their applications to all-optical ultrasound transducers and imaging. *Applied Sciences*, 7(1):25, 2017.

[97] X Deng, L Mammen, HJ Butt, and D Vollmer. Candle soot as a template for a transparent robust superamphiphobic coating. *Science*, 335(6064):67–70, 2012.

[98] Y Hou, S Ashkenazi, S Huang, and M O'Donnell. Improvements in optical generation of high-frequency ultrasound. *IEEE transactions on ultrasonics, ferroelectrics, and frequency control*, 54(3):682–686, 2007.

[99] Y Hou, JS Kim, S Ashkenazi, M O'Donnell, and LJ Guo. Optical generation of high frequency ultrasound using two-dimensional gold nanostructure. *Applied physics letters*, 89(9):093901, 2006.

[100] RJ Colchester, CA Mosse, DS Bhachu, JC Bear, CJ Carmalt, IP Parkin, BE Treeby, I Papakonstantinou, and AE Desjardins. Laser-generated ultrasound with optical fibres using functionalised carbon nanotube composite coatings. *Applied Physics Letters*, 104(17):173502, 2014.

[101] S Noimark, RJ Colchester, BJ Blackburn, EZ Zhang, EJ Alles, S Ourselin, PC Beard, I Papakonstantinou, IP Parkin, and AE Desjardins. Carbon-nanotube–PDMS composite coatings on optical fibers for all-optical ultrasound imaging. *Advanced Functional Materials*, 26(46):8390–8396, 2016.

[102] HW Baac, JG Ok, A Maxwell, KT Lee, YC Chen, AJ Hart, Z Xu, E Yoon, and LJ Guo. Carbon-nanotube optoacoustic lens for focused ultrasound generation and high-precision targeted therapy. *Scientific reports*, 2(1):1–8, 2012.

[103] B-Y Hsieh, J Kim, J Zhu, S Li, X Zhang, and X Jiang. A laser ultrasound transducer using carbon nanofibers–polydimethylsiloxane composite thin film. *Applied Physics Letters*, 106(2):021902, 2015.

[104] D Cui, Z Zhang, and Y Shi. Optically-excited simultaneous photoacoustic and ultrasound imaging based on a flexible gold-PDMS film. *Journal of Innovative Optical Health Sciences*, 13(04):2050012, 2020.

[105] S Rajagopal, T Sainsbury, BE Treeby, and BT Cox. Laser generated ultrasound sources using carbon-polymer nanocomposites for high frequency metrology. *The Journal of the Acoustical Society of America*, 144(2):584–597, 2018.

[106] W Gotschy, K Vonmetz, A Leitner, and FR Aussenegg. Optical dichroism of lithographically designed silver nanoparticle films. *Optics letters*, 21(15):1099–1101, 1996.

[107] YS Chen, W Frey, S Kim, K Homan, P Kruizinga, K Sokolov, and S Emelianov. Enhanced thermal stability of silica-coated gold nanorods for photoacoustic imaging and image-guided therapy. *Optics express*, 18(9):8867–8878, 2010.

[108] D Pan, B Kim, LV Wang, and GM Lanza. A brief account of nanoparticle contrast agents for photoacoustic imaging. *Wiley Interdisciplinary Reviews: Nanomedicine and Nanobiotechnology*, 5(6):517–543, 2013.

[109] X Zou, N Wu, Y Tian, and X Wang. Broadband miniature fiber optic ultrasound generator. *Optics express*, 22(15):18119–18127, 2014.

[110] AA Bogdanov Jr, AJ Dixon, S Gupta, L Zhang, S Zheng, MS Shazeeb, S Zhang, and AL Klibanov. Synthesis and testing of modular dual-modality nanoparticles for magnetic resonance and multispectral photoacoustic imaging. *Bioconjugate chemistry*, 27(2):383–390, 2016.

[111] Y Zhao, F Ye, TB Brismar, X Li, R He, R Heuchel, R El-Sayed, N Feliu, W Zheng, S Oerther, et al. Multimodal imaging of pancreatic ductal adenocarcinoma using multifunctional nanoparticles as contrast agents. *ACS applied materials & interfaces*, 12(48):53665–53681, 2020.

[112] M Bouche, M Puhringer, A Iturmendi, A Amirshaghaghi, A Tsourkas, I Teasdale, and DP Cormode. Activatable hybrid polyphosphazene-aunp nanoprobe for ros detection by bimodal pa/ct imaging. *ACS applied materials & interfaces*, 11(32):28648–28656, 2019.

[113] R Weissleder. A clearer vision for *in vivo* imaging. *Nature biotechnology*, 19(4):316–317, 2001.

[114] H SadAbadi, S Badilescu, M Packirisamy, and R Wüthrich. PDMS-gold nanocomposite platforms with enhanced sensing properties. *Journal of biomedical nanotechnology*, 8(4):539–549, 2012.

[115] LA Sordillo, Y Pu, S Pratavieira, Y Budansky, and RR Alfano. Deep optical imaging of tissue using the second and third near-infrared spectral windows. *Journal of biomedical optics*, 19(5):056004, 2014.

[116] AM Smith, MC Mancini, and S Nie. Second window for *in vivo* imaging. *Nature nanotechnology*, 4(11):710–711, 2009.

[117] AS Schulze, I Tavernaro, F Machka, O Dakischew, KS Lips, and MS Wickleder. Tuning optical properties of water-soluble CdTe quantum dots for biological applications. *Journal of Nanoparticle Research*, 19:1–16, 2017.

[118] JP Clifford, G Konstantatos, KW Johnston, S Hoogland, L Levina, and EH Sargent. Fast, sensitive and spectrally tuneable colloidal-quantum-dot photodetectors. *Nature nanotechnology*, 4(1):40–44, 2009.

[119] S Bodian, RJ Colchester, TJ Macdonald, F Ambroz, M Briceno de Gutierrez, SJ Mathews, YMM Fong, E Maneas, KA Welsby, RJ Gordon, et al. CuInS2 quantum dot and polydimethylsiloxane nanocomposites for all-optical ultrasound and photoacoustic imaging. *Advanced Materials Interfaces*, page 2100518, 2021.

[120] SI Reja, M Minoshima, Y Hori, and K Kikuchi. Near-infrared fluorescent probes: a next-generation tool for protein-labeling applications. *Chemical Science*, 12(10):3437–3447, 2021.

[121] CL Bliss, JN McMullin, and CJ Backhouse. Integrated wavelength-selective optical waveguides for microfluidic-based laser-induced fluorescence detection. *Lab on a Chip*, 8(1):143–151, 2008.

[122] S Perni, C Piccirillo, J Pratten, P Prokopovich, W Chrzanowski, IP Parkin, and M Wilson. The antimicrobial properties of light-activated polymers containing methylene blue and gold nanoparticles. *Biomaterials*, 30(1):89–93, 2009.

[123] G Wissmeyer, MA Pleitez, A Rosenthal, and V Ntziachristos. Looking at sound: optoacoustics with all-optical ultrasound detection. *Light: Science & Applications*, 7(1):53, 2018.

[124] P Morris, A Hurrell, and P Beard. Moving towards an ideal frequency response with fibre-optic hydrophones. In *2009 IEEE International Ultrasonics Symposium*, pages 944–947. IEEE, 2009.

[125] AM Winkler, K Maslov, and LV Wang. Noise-equivalent sensitivity of photoacoustics. *Journal of biomedical optics*, 18(9):097003–097003, 2013.

[126] J Rebling, O Warshavski, C Meynier, and D Razansky. Optoacoustic characterization of broadband directivity patterns of capacitive micromachined ultrasonic transducers. *Journal of biomedical optics*, 22(4):041005–041005, 2017.

[127] S Yang, W Qin, H Guo, T Jin, N Huang, M He, and L Xi. Design and evaluation of a compound acoustic lens for photoacoustic computed tomography. *Biomedical optics express*, 8(5):2756–2765, 2017.

[128] J Buchmann, J Guggenheim, E Zhang, C Scharfenorth, B Spannekrebs, C Villringer, and J Laufer. Characterization and modeling of Fabry–Perot ultrasound sensors with hard dielectric mirrors for photoacoustic imaging. *Applied optics*, 56(17):5039–5046, 2017.

[129] A Hurrell and P Beard. Piezoelectric and fibre-optic hydrophones. In *Ultrasonic transducers*, pages 619–676. Elsevier, 2012.

[130] MM Frocht. *Photoelasticity: Proceedings of the International Symposium Held at Illinois Institute of Technology, Chicago, Illinois, October 1961*. Elsevier, 2014.

[131] JA Guggenheim, J Li, TJ Allen, RJ Colchester, S Noimark, O Ogunlade, IP Parkin, I Papakonstantinou, AE Desjardins, EZ Zhang, et al. Ultrasensitive plano-concave optical microresonators for ultrasound sensing. *Nature Photonics*, 11(11):714–719, 2017.

[132] RC Preston. *Output measurements for medical ultrasound*. Springer Science & Business Media, 2012.

[133] A Pérot and C Fabry. On the application of interference phenomena to the solution of various problems of spectroscopy and metrology. *Astrophysical Journal*, 9:87 – 114, 1899.

[134] P Morris, A Hurrell, A Shaw, E Zhang, and P Beard. A Fabry–Pérot fiber-optic ultrasonic hydrophone for the simultaneous measurement of tempera-

ture and acoustic pressure. *The Journal of the Acoustical Society of America*, 125(6):3611–3622, 2009.

[135] EZ Zhang and PC Beard. A miniature all-optical photoacoustic imaging probe. In *Photons plus Ultrasound: Imaging and Sensing*, volume 7899, page 78991F. International Society for Optics and Photonics, 2011.

[136] EZ Zhang and PC Beard. Characteristics of optimized fibre-optic ultrasound receivers for minimally invasive photoacoustic detection. In *Photons Plus Ultrasound: Imaging and Sensing 2015*, volume 9323, page 932311. International Society for Optics and Photonics, 2015.

[137] C Sheaff and S Ashkenazi. Polyimide-etalon all-optical ultrasound transducer for high frequency applications. In *Photons Plus Ultrasound: Imaging and Sensing 2014*, volume 8943, pages 687–694. SPIE, 2014.

[138] RJ Colchester, EZ Zhang, PC Beard, and AE Desjardins. High-resolution sub-millimetre diameter side-viewing all-optical ultrasound transducer based on a single dual-clad optical fibre. *Biomedical Optics Express*, 13(7):4047–4057, 2022.

[139] RJ Colchester, C Little, G Dwyer, S Noimark, EJ Alles, EZ Zhang, CD Loder, IP Parkin, I Papakonstantinou, PC Beard, et al. All-optical rotational ultrasound imaging. *Scientific Reports*, 9(1):1–8, 2019.

[140] S Zhang, EZ Zhang, PC Beard, AE Desjardins, and RJ Colchester. Dual-modality fibre optic probe for simultaneous ablation and ultrasound imaging. *Communications Engineering*, 1(1):1–9, 2022.

[141] BY Hsieh, SL Chen, T Ling, LJ Guo, and PC Li. All-optical transducer for ultrasound and photoacoustic imaging by dichroic filtering. In *2012 IEEE International Ultrasonics Symposium*, pages 1410–1413. IEEE, 2012.

[142] RJ Colchester, S Noimark, EZ Zhang, PC Beard, and AE Desjardins. Dual-modality all-optical ultrasound and photoacoustic imaging using permanent

marker ink. In *2018 IEEE International Ultrasonics Symposium (IUS)*, pages 1–4. IEEE, 2018.

[143] JR Lakowicz. *Principles of fluorescence spectroscopy*. Springer, 2006.

[144] R Weissleder and V Ntziachristos. Shedding light onto live molecular targets. *Nature medicine*, 9(1):123–128, 2003.

[145] AC Sedgwick, L Wu, HH Han, SD Bull, XP He, TD James, JL Sessler, BZ Tang, H Tian, and J Yoon. Excited-state intramolecular proton-transfer (ESIPT) based fluorescence sensors and imaging agents. *Chemical Society Reviews*, 47(23):8842–8880, 2018.

[146] K Chevalier, A Grun, and A Stamm. ESIPT and photodissociation of 3-hydroxychromone in solution: Photoinduced processes studied by static and time-resolved UV/Vis, fluorescence, and IR spectroscopy. *The Journal of Physical Chemistry*, 117(44):11233–11245, 2013.

[147] J Wu, W Liu, J Ge, H Zhang, and P Wang. New sensing mechanisms for design of fluorescent chemosensors emerging in recent years. *Chemical Society Reviews*, 40(7):3483–3495, 2011.

[148] T Ueno, Y Urano, H Kojima, and T Nagano. Mechanism-based molecular design of highly selective fluorescence probes for nitrative stress. *Journal of the American Chemical Society*, 128(33):10640–10641, 2006.

[149] F Yu, P Li, B Wang, and K Han. Reversible near-infrared fluorescent probe introducing tellurium to mimetic glutathione peroxidase for monitoring the redox cycles between peroxynitrite and glutathione in vivo. *Journal of the American Chemical Society*, 135(20):7674–7680, 2013.

[150] J Shao, H Sun, H Guo, S Ji, J Zhao, W Wu, X Yuan, C Zhang, and TD James. A highly selective red-emitting FRET fluorescent molecular probe derived from BODIPY for the detection of cysteine and homocysteine: an experimental and theoretical study. *Chemical Science*, 3(4):1049–1061, 2012.

[151] EM Brustad, EA Lemke, PG Schultz, and AA Deniz. A general and efficient method for the site-specific dual-labeling of proteins for single molecule fluorescence resonance energy transfer. *Journal of the American Chemical Society*, 130(52):17664–17665, 2008.

[152] K Bracha-Drori, K Shichrur, A Katz, M Oliva, R Angelovici, S Yalovsky, and N Ohad. Detection of protein–protein interactions in plants using bimolecular fluorescence complementation. *The Plant Journal*, 40(3):419–427, 2004.

[153] Z Shen, Z Lu, PY Chhatbar, P O'herron, and P Kara. An artery-specific fluorescent dye for studying neurovascular coupling. *Nature methods*, 9(3):273–276, 2012.

[154] M Maroteaux and SJ Liu. Alteration of AMPA receptor-mediated synaptic transmission by Alexa Fluor 488 and 594 in cerebellar stellate cells. *Eneuro*, 3(3), 2016.

[155] OA Kucherak, S Oncul, Z Darwich, DA Yushchenko, Y Arntz, P Didier, Y Mely, and AS Klymchenko. Switchable nile red-based probe for cholesterol and lipid order at the outer leaflet of biomembranes. *Journal of the American Chemical Society*, 132(13):4907–4916, 2010.

[156] C Hättig, A Hellweg, and A Köhn. Intramolecular charge-transfer mechanism in quinolidines: The role of the amino twist angle. *Journal of the American Chemical Society*, 128(49):15672–15682, 2006.

[157] JS Chen, RZ Liu, Y Yang, and TS Chu. Intramolecular charge transfer and sensing mechanism for a colorimetric fluoride sensor based on 1, 8-naphthalimide derivatives. *Theoretical Chemistry Accounts*, 133:1–7, 2014.

[158] J Pawley. *Handbook of biological confocal microscopy*, volume 236. Springer Science & Business Media, 2006.

[159] MY Berezin and S Achilefu. Fluorescence lifetime measurements and biological imaging. *Chemical reviews*, 110(5):2641–2684, 2010.

[160] A Diaspro. *Confocal and two-photon microscopy: foundations, applications and advances*. John Wiley & Sons, 2001.

[161] Hamamatsu. Photomultiplier tubes: Basics and applications, 2017. *www.hamamatsu.com/content/dam/hamamatsu-photonics/sites/documents/PMThandbook.pdf* [Accessed 20-08-2024].

[162] GF Amelio, MF Tompsett, and GE Smith. Experimental verification of the charge coupled device concept. *Bell System Technical Journal*, 49(4):593–600, 1970.

[163] RK Henderson, BR Rae, and D-U Li. Complementary metal-oxide-semiconductor (CMOS) sensors for fluorescence lifetime imaging (FLIM). In *High performance silicon imaging*, pages 312–347. Elsevier, 2014.

[164] JC Campbell, S Demiguel, F Ma, A Beck, X Guo, S Wang, X Zheng, X Li, JD Beck, MA Kinch, et al. Recent advances in avalanche photodiodes. *IEEE Journal of selected topics in quantum electronics*, 10(4):777–787, 2004.

[165] JR Swedlow and M Platani. Live cell imaging using wide-field microscopy and deconvolution. *Cell structure and function*, 27(5):335–341, 2002.

[166] A Stemmer, M Beck, and R Fiolka. Widefield fluorescence microscopy with extended resolution. *Histochemistry and cell biology*, 130:807–817, 2008.

[167] JW Lichtman and JA Conchello. Fluorescence microscopy. *Nature methods*, 2(12):910–919, 2005.

[168] W Denk, JH Strickler, and WW Webb. Two-photon laser scanning fluorescence microscopy. *Science*, 248(4951):73–76, 1990.

[169] JB Ding, KT Takasaki, and BL Sabatini. Supraresolution imaging in brain slices using stimulated-emission depletion two-photon laser scanning microscopy. *Neuron*, 63(4):429–437, 2009.

[170] K Svoboda and R Yasuda. Principles of two-photon excitation microscopy and its applications to neuroscience. *Neuron*, 50(6):823–839, 2006.

[171] X Liu, P Wang, J Fu, D Lv, D Chen, Y Li, and W Ma. Two-photon fluorescence real-time imaging on the development of early mouse embryo by stages. *Journal of microscopy*, 241(2):212–218, 2011.

[172] W Becker. Fluorescence lifetime imaging–techniques and applications. *Journal of microscopy*, 247(2):119–136, 2012.

[173] MA Aegerter and M Mennig. *Sol-gel technologies for glass producers and users*. Springer Science & Business Media, 2013.

[174] N Hijón, MV Cabanas, J Pena, and M Vallet-Regí. Dip coated silicon-substituted hydroxyapatite films. *Acta biomaterialia*, 2(5):567–574, 2006.

[175] RJ Colchester, EJ Alles, and AE Desjardins. A directional fibre optic ultrasound transmitter based on a reduced graphene oxide and polydimethylsiloxane composite. *Applied Physics Letters*, 114(11):113505, 2019.

[176] E Zhang, J Laufer, and P Beard. Backward-mode multiwavelength photoacoustic scanner using a planar Fabry-Perot polymer film ultrasound sensor for high-resolution three-dimensional imaging of biological tissues. *Applied Optics*, 47(4):561–577, 2008.

[177] RJ Colchester, EZ Zhang, CA Mosse, PC Beard, I Papakonstantinou, and AE Desjardins. Broadband miniature optical ultrasound probe for high resolution vascular tissue imaging. *Biomedical Optics Express*, 6(4):1502–1511, 2015.

[178] Epolin. Epolight 9837 nir dye technical data sheet (2013). *www.epolin.com/wp-content/uploads/2021/02/9837-data-sheet.pdf*. [Online; accessed 1 November 2021].

[179] MC Finlay, CA Mosse, RJ Colchester, S Noimark, EZ Zhang, S Ourselin, PC Beard, RJ Schilling, IP Parkin, I Papakonstantinou, et al. Through-needle

all-optical ultrasound imaging *in vivo*: a preclinical swine study. *Light: Science & Applications*, 6(12):e17103–e17103, 2017.

[180] V Amendola, R Pilot, M Frasconi, OM Maragò, and MA Iatì. Surface plasmon resonance in gold nanoparticles: a review. *Journal of Physics: Condensed Matter*, 29(20):203002, 2017.

[181] S Barazzouk, L Bekalé, and S Hotchandani. Enhanced photostability of chlorophyll-a using gold nanoparticles as an efficient photoprotector. *Journal of Materials Chemistry*, 22(48):25316–25324, 2012.

[182] AP Demchenko. Photobleaching of organic fluorophores: quantitative characterization, mechanisms, protection. *Methods and applications in fluorescence*, 8(2):022001, 2020.

[183] J Widengren and R Rigler. Mechanisms of photobleaching investigated by fluorescence correlation spectroscopy. *Bioimaging*, 4(3):149–157, 1996.

[184] KS Suslick. Sonochemistry. *science*, 247(4949):1439–1445, 1990.

[185] KS Suslick. The chemical effects of ultrasound. *Scientific American*, 260(2):80–87, 1989.

[186] J Gonzalez-Garcia, V Saez, I Tudela, MI Diez-Garcia, M Deseada Esclapez, and O Louisnard. Sonochemical treatment of water polluted by chlorinated organocompounds. a review. *Water*, 2(1):28–74, 2010.

[187] D Menichelli and E Biagi. Optoacoustic sources: a practical Green function-based model for thin film laser-ultrasound generation. *Journal of Optics A: Pure and Applied Optics*, 3(4):S23, 2001.

[188] C Lee, K Fujino, Y Motooka, A Gregor, N Bernards, H Ujiie, T Kinoshita, K Chung, S Han, and K Yasufuku. Photoacoustic imaging to localize indeterminate pulmonary nodules: A preclinical study. *PloS one*, 15(4):e0231488, 2020.

[189] Z Nie, S-CA Yeh, M LePalud, F Badr, F Tse, D Armstrong, LWC Liu, MJ Deen, and Q Fang. Optical biopsy of the upper GI tract using fluorescence lifetime and spectra. *Frontiers in Physiology*, 11:339, 2020.

[190] RS PRO. Silver conductive lacquer technical data sheet (2015). *https://uk.rs-online.com/web/p/electronics-varnishes/1239911* [Online; accessed 27 July 2024].

[191] RJ Colchester. *Novel optical ultrasound probes for minimally invasive surgery*. PhD thesis, UCL (University College London), 2016.

[192] M Kay and R Wyllie. Esophagogastroduodenoscopy and related techniques. In *Pediatric Gastrointestinal and Liver Disease*, pages 626–649. Elsevier, 2011.

[193] X Li, W Wu, Y Chung, WY Shih, W-H Shih, Q Zhou, and KK Shung. 80-MHz intravascular ultrasound transducer using PMN-PT free-standing film. *IEEE Transactions on Ultrasonics, Ferroelectrics, and Frequency Control*, 58(11):2281–2288, 2011.

[194] C Peng, H Wu, S Kim, X Dai, and X Jiang. Recent advances in transducers for intravascular ultrasound (IVUS) imaging. *Sensors*, 21(10):3540, 2021.

[195] FS Foster, CJ Pavlin, KA Harasiewicz, DA Christopher, and DH Turnbull. Advances in ultrasound biomicroscopy. *Ultrasound in Medicine & Biology*, 26(1):1–27, 2000.

[196] S Bodian, E Aytac-Kipergil, S Zhang, I Lewis-Thompson, S Sathasivam, SJ Mathews, EJ Alles, EZ Zhang, PC Beard, RJ Gordon, et al. Comparison of fabrication methods for fiber-optic ultrasound transmitters using candle-soot nanoparticles. *Advanced Materials Interfaces*, page 2201792, 2023.

[197] MH Sorg and WD Haglund. *Forensic taphonomy: the postmortem fate of human remains*. crc press, 1996.

[198] RV Krstic. *Human microscopic anatomy: an atlas for students of medicine and biology*. Springer Science & Business Media, 2013.

[199] M Slaoui and L Fiette. Histopathology procedures: from tissue sampling to histopathological evaluation. *Drug Safety Evaluation: Methods and Protocols*, pages 69–82, 2011.

[200] A Knapik, K Kornmann, K Kerl, M Calcagni, C Contaldo, B Vollmar, P Giovanoli, and N Lindenblatt. Practice of split-thickness skin graft storage and histological assessment of tissue quality. *Journal of Plastic, Reconstructive & Aesthetic Surgery*, 66(6):827–834, 2013.

[201] B Winkler, D Reineke, PP Heinisch, F Schonhoff, C Huber, A Kadner, L Englberger, and T Carrel. Graft preservation solutions in cardiovascular surgery. *Interactive cardiovascular and thoracic surgery*, 23(2):300–309, 2016.

[202] G Cao and X Li. The decellularization of tissues. *Decellularized Materials: Preparations and Biomedical Applications*, pages 69–114, 2021.

[203] Platelet Third Edition. Robbins & cotran pathologic basis of disease, 2013.

[204] BA Standish, KKC Lee, A Mariampillai, NR Munce, MKK Leung, VXD Yang, and IA Vitkin. In vivo endoscopic multi-beam optical coherence tomography. *Physics in Medicine & Biology*, 55(3):615, 2010.

[205] C Sheaff and S Ashkenazi. Characterization of an improved polyimide-etalon all-optical transducer for high-resolution ultrasound imaging. *IEEE Transactions on Ultrasonics, Ferroelectrics, and Frequency Control*, 61(7):1223–1232, 2014.

[206] EJ Alles, RJ Colchester, and AE Desjardins. Adaptive light modulation for improved resolution and efficiency in all-optical pulse-echo ultrasound. *IEEE Transactions on Ultrasonics, Ferroelectrics, and Frequency Control*, 63(1):83–90, 2015.

[207] R Harrison, I Perry, W Haddadin, S McDonald, R Bryan, K Abrams, R Sampliner, NJ Talley, P Moayyedi, and JA Jankowski. Detection of intestinal metaplasia in Barrett's Oesophagus: an observational comparator study suggests the need for a minimum of eight biopsies. *Official Journal of the American College of Gastroenterology*, 102(6):1154–1161, 2007.

[208] PAC Gatenby, JR Ramus, CPJ Caygill, NA Shepherd, and A Watson. Relevance of the detection of intestinal metaplasia in non-dysplastic columnar-lined oesophagus. *Scandinavian Journal of Gastroenterology*, 43(5):524–530, 2008.

[209] G Li, Z Guo, and S-L Chen. Miniature all-optical probe for large synthetic aperture photoacoustic-ultrasound imaging. *Optics Express*, 25(21):25023–25035, 2017.

[210] S Yoshinaga, I Oda, S Nonaka, R Kushima, and Y Saito. Endoscopic ultrasound using ultrasound probes for the diagnosis of early esophageal and gastric cancers. *World Journal of Gastrointestinal Endoscopy*, 4(6):218, 2012.

[211] MB Kimmey, RW Martin, RC Haggitt, KY Wang, DW Franklin, and FE Silverstein. Histologic correlates of gastrointestinal ultrasound images. *Gastroenterology*, 96(2):433–441, 1989.

[212] L Lekakos, NP Karidis, D Dimitroulis, C Tsigris, G Kouraklis, and Nikolaos Nikiteas. Barrett's Oesophagus with high-grade dysplasia: focus on current treatment options. *World Journal of Gastroenterology: WJG*, 17(37):4174, 2011.

[213] BV Naini, RF Souza, and RD Odze. Barrett's Oesophagus: a comprehensive and contemporary review for pathologists. *The American Journal of Surgical Pathology*, 40(5):e45, 2016.

[214] DK Rex, OW Cummings, M Shaw, MD Cumings, RKH Wong, RS Vasudeva, D Dunne, EY Rahmani, and DJ Helper. Screening for Barrett's Oesopha-

gus in colonoscopy patients with and without heartburn. *Gastroenterology*, 125(6):1670–1677, 2003.

[215] A Joseph, S Raja, S Kamath, S Jang, D Allende, M McNamara, G Videtic, S Murthy, and A Bhatt. Esophageal adenocarcinoma: A dire need for early detection and treatment. *Cleveland Clinic Journal of Medicine*, 89(5):269–279, 2022.

[216] FT Watt, S Noimark, AE Desjardins, PC Beard, and EJ Alles. Fabrication of an array of eccentric sources for freehand optical ultrasound imaging. In *2022 IEEE International Ultrasonics Symposium (IUS)*, pages 1–4. IEEE, 2022.

[217] KT Schomacker, JK Frisoli, and CC Compton. Ultraviolet laser-induced fluorescence of colonic cancer: basic biology and diagnostic potential. *Lasers Surg Med*, 12:63–78, 1992.

[218] GC Tang, A Pradhan, and RR Alfano. Spectroscopic differences between human cancer and normal lung and breast tissues. *Lasers Surg Med*, 9:290–295, 1989.

[219] DS Levine, RC Haggitt, PL Blount, PS Rabinovitch, VW Rusch, and BJ Reid. An endoscopic biopsy protocol can differentiate high-grade dysplasia from early adenocarcinoma in Barrett's Oesophagus. *Gastroenterology*, 105:40–50, 1993.

[220] R Raj, M Firoz Khan, M Shariq, N Ahsan, R Singh, and P Kumar Basoya. Point-of-care optical devices in clinical imaging and screening: a review on the state of the art. *Journal of Biophotonics*, 16(6):e202200386, 2023.

[221] L Angelova, E Borisova, Al Zhelyazkova, M Keremedchiev, B Vladimirov, and L Avramov. Fluorescence spectroscopy of gastrointestinal tumors: in vitro studies and in vivo clinical applications. In *Biophotonics—Riga 2013*, volume 9032, pages 42–52. SPIE, 2013.

[222] JJ Workman. A review of calibration transfer practices and instrument differences in spectroscopy. *Applied spectroscopy*, 72(3):340–365, 2018.

[223] F Aghlmand, CY Hu, S Sharma, K Pochana, RM Murray, and A Emami. A 65-nm CMOS fluorescence sensor for dynamic monitoring of living cells. *IEEE Journal of Solid-State Circuits*, 2023.

[224] PC Beard, F Perennes, and TN Mills. Transduction mechanisms of the Fabry-Perot polymer film sensing concept for wideband ultrasound detection. *IEEE Transactions on Ultrasonics, Ferroelectrics, and Frequency Control*, 46(6):1575–1582, 1999.

[225] BT Cox and PC Beard. Fast calculation of pulsed photoacoustic fields in fluids using k-space methods. *The Journal of the Acoustical Society of America*, 117(6):3616–3627, 2005.

[226] YJ Choi and K Sawada. Physical sensors: Fluorescence sensors. *Encyclopedia of Sensors and Biosensors, ELSEVIER*, 1:1–19, 2023.

[227] CP Moon and KG Fleming. Using tryptophan fluorescence to measure the stability of membrane proteins folded in liposomes. In *Methods in enzymology*, volume 492, pages 189–211. Elsevier, 2011.

[228] MR Eftink. The use of fluorescence methods to monitor unfolding transitions in proteins. *Biophysical journal*, 66(2):482–501, 1994.

[229] RC Gonzalez. *Digital image processing*. Pearson education india, 2009.

[230] D Schweitzer, M Klemm, S Quick, L Deutsch, S Jentsch, M Hammer, J Dawczynski, CH Kloos, and UA Mueller. Detection of early metabolic alterations in the ocular fundus of diabetic patients by time-resolved autofluorescence of endogenous fluorophores. In *European Conference on Biomedical Optics*, page 80871G. Optica Publishing Group, 2011.

[231] M Panjehpour, CE Julius, MN Phan, T Vo-Dinh, and S Overholt. Laser-induced fluorescence spectroscopy for in vivo diagnosis of non-melanoma

skin cancers. *Lasers in Surgery and Medicine: The Official Journal of the American Society for Laser Medicine and Surgery*, 31(5):367–373, 2002.